

FINITE-QUARK-MASS EFFECTS ON THE HIGGS PRODUCTION CROSS SECTION IN THE GLUON-GLUON FUSION CHANNEL

Dissertation

zur Erlangung des Doktorgrades an der Fakultät für Mathematik, Informatik und
Naturwissenschaften

Fachbereich Physik der Rheinisch-Westfälischen Technischen Hochschule

vorgelegt von

TOM CLAUS RUDOLF SCHELLENBERGER

Aachen

1. Juli 2025

Finite-Quark-Mass Effects on the Higgs Production Cross Section in the Gluon-Gluon Fusion Channel

© Tom Claus Rudolf Schellenberger 2025

GUTACHTER DER DISSERTATION:

Prof. Dr. Michał Czakon
Prof. Dr. Robert Harlander

ZUSAMMENSETZUNG DER PRÜFUNGSKOMMISSION:

Prof. Dr. Michał Czakon
Prof. Dr. Robert Harlander
TBA
TBA

VORSITZENDER DER PRÜFUNGSKOMMISSION:

TBA

DATUM DER DISPUTATION:

TBA

DEKAN DER FAKULTÄT MIN:

Prof. Dr. Carsten Honerkamp

ABSTRACT

This is my Abstract

ZUSAMMENFASSUNG

Dies ist meine Zusammenfassung

ACKNOWLEDGMENTS

Here is where I thank god.

PUBLICATIONS

During my PhD studies, I co-authored the following publications:

- [1] Michał Czakon, Felix Schlenker, and Tom Schellenberger. “Revisiting the double-soft asymptotics of one-loop amplitudes in massless QCD.” In: *JHEP* 04 (2023), p. 065. DOI: [10.1007/JHEP04\(2023\)065](#). arXiv: [2211.06465 \[hep-ph\]](#)
- [2] Michał Czakon, Felix Schlenker, and Tom Schellenberger. “Subleading effects in soft-gluon emission at one-loop in massless QCD.” In: *JHEP* 12 (2023), p. 126. DOI: [10.1007/JHEP12\(2023\)126](#). arXiv: [2307.02286 \[hep-ph\]](#)
- [3] Michał Czakon et al. “Top-Bottom Interference Contribution to Fully Inclusive Higgs Production.” In: *Phys. Rev. Lett.* 132.21 (2024), p. 211902. DOI: [10.1103/PhysRevLett.132.211902](#). arXiv: [2312.09896 \[hep-ph\]](#)
- [4] Michał Czakon et al. “Quark mass effects in Higgs production.” In: *JHEP* 10 (2024), p. 210. DOI: [10.1007/JHEP10\(2024\)210](#). arXiv: [2407.12413 \[hep-ph\]](#)

Among these, only the last two are directly relevant to this dissertation.

CONTENTS

1	Introduction	1
2	The Standard Model of Particle Physics	3
2.1	Electroweak Symmetry breaking	3
2.2	Cross Sections	7
2.2.1	The Hard Scattering Amplitude	8
2.2.2	The Parton Distribution Functions	11
2.2.3	The Phase-Space Integration	13
3	The Higgs as a Window to New Physics	19
3.1	Higgs Portal	19
3.2	Stability of the Higgs Potential	22
3.3	The Hierarchy Problem	22
4	Hadronic Higgs Production	23
4.1	The Leading-Order Cross Section	24
4.2	The Heavy-Top Limit	28
4.2.1	Renormalization of Gauge Invariant Operators	29
4.2.2	Matching of Wilson Coefficients	33
4.2.3	Higher-Order Corrections	36
4.2.4	Phenomenological Application	41
4.3	Theory Status	43
4.3.1	Scale Uncertainties	44
4.3.2	PDF Uncertainties	47
4.3.3	Electroweak Corrections	50
4.3.4	Finite Top-Quark Mass Effects	52
4.3.5	Effect of Light Quarks	53
4.3.6	Differential Cross Sections	55
5	Computational Details	57
5.1	Computing the Amplitudes	57
5.1.1	The Real-Real Corrections	58
5.1.2	The Real-Virtual Corrections	59
5.1.3	The Virtual-Virtual Corrections	75
5.2	The 4-Flavour Scheme	76
5.3	$\overline{\text{MS}}$ -scheme	78
5.4	Performing the Phase-Space Integration	83
6	Results and Discussion	85
6.1	Total Cross Section	85
6.1.1	Effects of Finite Top-Quark Masses	85
6.1.2	Effects of Finite Bottom-Quark Masses	86
6.2	Differential Cross Section	92
6.3	Validation & Comparison With Other Works	94

6.4 Recommendations for Phenomenological Applications	96
7 Conclusions	99
A Feynman Rules of the Standard Model	101
B Feynman Integrals	105
C Energy Scan of the Top-Bottom Interference Contribution	107
D On-shell Results for the Differential Cross Section	109
Bibliography	111

ACRONYMS

SM	Standard model
VEV	Vacuum expectation value
SSB	Spontaneous symmetry breaking
PDF	Parton distribution function
QCD	Quantum chromodynamics
QED	Quantum electrodynamics
RGE	Renormalization group equation
LO	Leading order
DR	Dimensional regularization
UV	Ultraviolet
IR	Infrared
LO	Leading order
NLO	Next-to-leading order
NNLO	Next-to-next-to-leading order
OS	On-shell renormalization
RG	Renormalization group
RGE	Renormalization group equation
LHC	Large hadron collider
FS	Flavor scheme
MC	Monte-Carlo
LME	Large mass expansion
HEL	High-energy limit
HTL	Heavy-top limit
rHTL	Rescaled heavy-top limit
SCET	Soft-collinear effective theory
IBP	Integration-by-parts
MSSM	Minimal supersymmetric standard model
DM	Dark matter

NOTATION, CONSTANTS AND CONVENTIONS

- In this thesis, I will be using the *Einstein summation convention*, by which any index—be it a Lorentz, color or flavor index—which appears twice is implicitly summed over.

- I will be using natural units

$$\hbar = c = 1. \quad (0.1)$$

- The electron charge is

$$-e, \quad e > 0. \quad (0.2)$$

- The metric is

$$g_{\mu\nu} = \begin{pmatrix} 1 & & & \\ & -1 & & \\ & & -1 & \\ & & & -1 \end{pmatrix}. \quad (0.3)$$

- The normalization of the Levi-Civita anti-symmetric tensor $\epsilon_{\mu\nu\rho\sigma}$ is

$$\epsilon_{0123} = +1 \quad (0.4)$$

- The Pauli matrices are defined as

$$\sigma^1 \equiv \begin{pmatrix} 0 & 1 \\ 1 & 0 \end{pmatrix}, \quad \sigma^2 \equiv \begin{pmatrix} 0 & -i \\ i & 0 \end{pmatrix}, \quad \sigma^3 \equiv \begin{pmatrix} 1 & 0 \\ 0 & -1 \end{pmatrix}, \quad \tau^i \equiv \sigma^i. \quad (0.5)$$

- Unless specifically specified otherwise we will use the following values for appearing physical constants

- $G_F = 1.16637 \times 10^{-5} \text{ GeV}^{-2}$
- $m_H = 125.00 \text{ GeV}$
- $m_t = 173.06 \text{ GeV}$
- $\overline{m}_t(\overline{m}_t) = 162.7 \text{ GeV}$
- $m_b = 4.78 \text{ GeV}$
- $\overline{m}_b(\overline{m}_b) = 4.18 \text{ GeV}$
- $\overline{m}_c(\overline{m}_c) = 1.27 \text{ GeV}$
- $m_Z = 91.1876 \text{ GeV}$

- We use the **NNPDF31_nnlo_as_0118** and **NNPDF31_nnlo_as_0118_nf_4PDF** set in the 5FS and 4FS respectively.

- α_s is extracted from the PDF set at the Z^0 mass.

1 | INTRODUCTION

General introductions

2.1 ELECTROWEAK SYMMETRY BREAKING

The standard model (SM) of particle physics is a theory describing all known matter and their fundamental interactions except for gravity. It unifies the electromagnetic, weak, and strong forces under a single theoretical framework. The matter content of the SM is classified into two primary groups: *fermions* and *bosons*. The fermions have spin 1/2, they are further subcategorized into *quarks* and *leptons*. Quarks participate in strong interactions, while leptons interact only via the electromagnetic and weak forces. In contrast, bosons have integer spin. There exists a single particle with spin 0, the *Higgs* boson, and four vector bosons, namely the gluon, the photon, and the *W* and *Z* boson. The vector bosons act as force carrier for the strong, the electromagnetic and the weak force respectively. Fermions are organized into three generations, with each generation containing two types of quarks (up-type and down-type) and two leptons (a charged lepton and its corresponding neutrino). These generations are shown in Fig. 2.1, along with their masses, charges, and spins.

The interactions between SM particles are described by a non-abelian gauge theory of the $SU(3)_C \times SU(2)_L \times U(1)_Y$ group. Here $SU(3)_C$ governs the strong interactions. It applies to all *colored* particles, i.e. quarks and gluons. The quarks transform under the fundamental representation of the $SU(3)_C$ group. $SU(2)_L \times U(1)_Y$ governs electroweak interactions. The $SU(2)_L$ transformation acts non-trivially only on *left-handed* fermions which form doublets

$$L_{iL} \equiv \begin{pmatrix} \nu_{iL} \\ l_{iL} \end{pmatrix}, \quad Q_{iL} \equiv \begin{pmatrix} u_{iL} \\ d_{iL} \end{pmatrix}, \quad (2.1)$$

$$\nu_i = (\nu_e, \nu_\mu, \nu_\tau), \quad l_i = (e, \mu, \tau), \quad u_i = (u, c, t), \quad d_i = (d, s, b).$$

The phase transformation $U(1)_Y$ acts on all particles except neutrinos according to their quantum number, the *hypercharge* Y . The symmetry is spontaneously broken to $SU(3)_C \times U(1)_Q$, where the $U(1)_Q$ group corresponds to gauge transformation of the electromagnetic interaction, hence the subscript Q for the *electric charge*. To ensure that the particles have the correct charges, the hypercharge must satisfy the *Gell-Mann–Nishijima relation*:

$$\frac{Y}{2} = Q - I^3. \quad (2.2)$$

With the particle charges displayed in Fig. 2.1 we then get

	L_{iL}	Q_{iL}	ν_{iR}	l_{iR}	u_{iR}	d_{iR}
$\frac{Y}{2}$	$-\frac{1}{2}$	$\frac{1}{6}$	0	-1	$\frac{2}{3}$	$-\frac{1}{3}$



Figure 2.1: Elementary particles of the SM. The was image generated with the help of Ref. [5].

The transformation properties of the gauge bosons is dictated by the covariance of the covariant derivative

$$D_\mu \equiv \partial_\mu - igA_\mu^a T_R^a - ig_2 W_\mu^a I^a + ig_Y \frac{Y}{2} B_\mu$$

$$T_R^a = \begin{cases} T^a & \text{for quarks,} \\ 0 & \text{for leptons,} \end{cases} \quad I^a = \begin{cases} \frac{\tau}{2} & \text{for left-handed fermions,} \\ 0 & \text{for right-handed fermions,} \end{cases} \quad (2.3)$$

where T^a and τ^a are the *Gell-Mann* and *Pauli* matrices.

Before spontaneous symmetry breaking, the Lagrangian which governs the evolution of all matter fields must be invariant under the $SU(3)_C \times SU(2)_L \times U(1)_Y$ gauge group. Up to a \mathbb{CP} violating term¹ the SM Lagrangian is the most general mass-dimension four Lagrangian for the described particle content

$$\mathcal{L}_{\text{SM}} = \mathcal{L}_G + \mathcal{L}_F + \mathcal{L}_Y + \mathcal{L}_H. \quad (2.4)$$

¹ The absence of the \mathbb{CP} violating term $\theta \frac{g^2}{64\pi^2} \epsilon^{\mu\nu\alpha\beta} F_{\mu\nu}^a F_{\alpha\beta}^a$ is an unsolved problem of particle physics, known as the strong CP problem.

The gauge-field Lagrangian \mathcal{L}_G describes the free propagation and in the case of the non-abelian groups $SU(3)_C$ and $SU(2)_L$ also the self-interaction of the gauge bosons. It is given by

$$\begin{aligned}\mathcal{L}_G &= -\frac{1}{4}G_{\mu\nu}^a G^{a\mu\nu} - \frac{1}{4}W_{\mu\nu}^a W^{a\mu\nu} - \frac{1}{4}B_{\mu\nu}B^{\mu\nu}, \\ G_{\mu\nu}^a &\equiv \partial_\mu A_\nu^a - \partial_\nu A_\mu^a + gf^{abc}A_\mu^b A_\nu^c, \\ W_{\mu\nu}^a &\equiv \partial_\mu W_\nu^a - \partial_\nu W_\mu^a + g_2\epsilon^{abc}W_\mu^b W_\nu^c, \\ B_{\mu\nu} &\equiv \partial_\mu B_\nu - \partial_\nu B_\mu.\end{aligned}\tag{2.5}$$

The propagation of the fermions and their interaction with the gauge bosons is described by

$$\mathcal{L}_F = \bar{L}_{iL}i\not{D}L_{iL} + \bar{\nu}_{iR}i\not{D}\nu_{iR} + \bar{l}_{iR}i\not{D}l_{iR} + \bar{Q}_{iL}i\not{D}Q_{iL} + \bar{u}_{iR}i\not{D}u_{iR} + \bar{d}_{iR}i\not{D}d_{iR}.\tag{2.6}$$

The Higgs field is a doublet of the $SU(2)_L$ group. We want the field to have a non-vanishing vacuum expectation value (VEV) to dynamically generate the fermion and boson masses. Of course, the vacuum cannot carry an electric charge, which means that the Higgs field must be electrically neutral along the direction of *spontaneous symmetry breaking* (SSB). We choose this to be the second component of the doublet. With the Gell-Mann–Nishijima relation we can then deduce that hypercharge of the doublet must be $Y = +1$. The Higgs doublet field thus takes the form

$$\Phi = \begin{pmatrix} \phi^+ \\ \phi^0 \end{pmatrix},\tag{2.7}$$

where the superscript indicates the electric charge.

In order to generate a non-vanishing VEV, the Higgs field must be in a potential with a global minimum away from zero. Hence, the only gauge invariant mass-dimension four Lagrangian we can construct is

$$\begin{aligned}\mathcal{L}_H &= (D_\mu\Phi)^\dagger (D^\mu\Phi) - V(\Phi) \\ V(\Phi) &= \lambda(\Phi^\dagger\Phi)^2 - \mu^2\Phi^\dagger\Phi, \quad \mu^2, \lambda > 0.\end{aligned}\tag{2.8}$$

The minimum of the Higgs potential V is at

$$\Phi_0^\dagger\Phi_0 = \frac{\mu^2}{2\lambda} \equiv \frac{v^2}{2} \neq 0.\tag{2.9}$$

After (SSB) we can expand the Higgs field around its minimum

$$\Phi = \begin{pmatrix} \phi^+ \\ \frac{1}{\sqrt{2}}(v + H + i\xi) \end{pmatrix}\tag{2.10}$$

The real scalar field H is the famous Higgs boson, whereas the fields ϕ^\pm and ξ are unphysical since they can always be eliminated through a gauge transformation (*would-be Goldstone bosons*). After inserting the expansion in the Higgs Lagrangian, the mass of the Higgs can be read off from its square term

$$m_H = \sqrt{2}\mu.\tag{2.11}$$

SSB enables the generation of vector boson masses without breaking the gauge symmetry explicitly. If we insert the expanded Higgs field in the Higgs Lagrangian, we get quadratic terms of the gauge boson fields

$$\begin{aligned}\mathcal{L}_H &\supseteq \frac{v^2}{2} \left\{ g_2^2 \begin{pmatrix} 0 & 1 \end{pmatrix} I^a I^b \begin{pmatrix} 0 \\ 1 \end{pmatrix} W_\mu^a W^{b\mu} - g_2 g_Y \begin{pmatrix} 0 & 1 \end{pmatrix} I^a \begin{pmatrix} 0 \\ 1 \end{pmatrix} W_\mu^a B^\mu + \frac{g_Y^2}{4} B_\mu B^\mu \right\} \\ &= \frac{v^2}{2} \left\{ \frac{g_2^2}{4} [(W^1)^2 + (W^2)^2] + \frac{1}{4} \begin{pmatrix} B^\mu & W^{3\mu} \end{pmatrix} \begin{pmatrix} g_Y^2 & g_Y g_2 \\ g_Y g_2 & g_2^2 \end{pmatrix} \begin{pmatrix} B_\mu \\ W_\mu^3 \end{pmatrix} \right\}.\end{aligned}\quad (2.12)$$

By diagonalizing the mass matrix we obtain the physical states

$$\begin{pmatrix} A_\mu^\gamma \\ Z_\mu \end{pmatrix} = \begin{pmatrix} \cos \theta_W & -\sin \theta_W \\ \sin \theta_W & \cos \theta_W \end{pmatrix} \begin{pmatrix} B_\mu \\ W_\mu^3 \end{pmatrix}, \quad \cos \theta_W = \frac{g_2}{\sqrt{g_Y^2 + g_2^2}}, \quad \sin \theta_W = \frac{g_Y}{\sqrt{g_Y^2 + g_2^2}}. \quad (2.13)$$

In this new basis, we have one massless boson A_μ^γ , which we identify as the photon and a charge neutral boson of mass

$$m_Z = \frac{v}{2} \sqrt{g_Y^2 + g_2^2}. \quad (2.14)$$

The vector bosons W^1 and W^2 are not eigenstates of the charge operator. We therefore define the new states

$$W_\mu^\pm = \frac{1}{\sqrt{2}} (W_\mu^1 \mp i W_\mu^2), \quad Q W_\mu^\pm = \pm W_\mu^\pm, \quad (2.15)$$

which are eigenstates of Q and have mass

$$m_W = \frac{v}{2} g_2. \quad (2.16)$$

Last but not least, we discuss the Yukawa sector of the SM Lagrangian. Before SSB, fermions cannot generate masses because a mass term would mix the left- and right-handed components of the fields, thereby breaking the chiral gauge symmetry. Here, once again, the Higgs field comes to the rescue: by coupling the fermions with the Higgs field through a Yukawa interaction²

$$\mathcal{L}_Y = - \left(y_{ij}^\nu \bar{L}_{iL} \Phi^c \nu_{jR} + y_{ij}^l \bar{L}_{iL} \Phi l_{jR} + y_{ij}^d \bar{Q}_{iL} \Phi d_{jR} + y_{ij}^u \bar{Q}_{iL} \Phi^c u_{jR} \right) + \text{h.c.}, \quad (2.17)$$

where Φ^c is the charge-conjugated field to Φ , we do not explicitly break the symmetry. However, after SSB this Lagrangian will generate exactly the required mixing between left- and right-handed fields to generate the fermion masses. The Yukawa-interaction matrices $y_{ij}^{\nu, l, d, u}$ can be shifted from the Yukawa sector to the fermion sector through a field redefinition. Indeed, if we apply the *singular value decomposition* of the Yukawa matrix

$$y = U_L^\dagger y_{\text{diag}} U_R, \quad \text{with} \quad (y_{\text{diag}})_{ij} = \sqrt{2} Y_i \delta_{ij} \quad \text{and} \quad U_{L,R} \in \text{U}(3), \quad (2.18)$$

and redefine our fermion fields to be

$$f_{iR} \longrightarrow U_{Rij} f_{jR}, \quad f_{iL} \longrightarrow U_{Lij} f_{jL}, \quad f = \nu, l, u, d \quad (2.19)$$

the Yukawa Lagrangian becomes

$$\mathcal{L}_Y = - \sum_i \left(m_{\nu_i} \bar{\nu}_i \nu_i + m_{l_i} \bar{l}_i l_i + m_{u_i} \bar{u}_i u_i + m_{d_i} \bar{d}_i d_i \right) \left(1 + \frac{H}{v} \right). \quad (2.20)$$

² In the original formulation of the SM, there are no neutrino Yukawa interactions, since they were believed to be massless. Neutrino oscillation experiments have shown however, that neutrinos do in fact have finite masses.

Here we identified the Yukawa coupling as $Y_i = m_i/v$ in order to generate the required mass terms. Consequently, we observe that the Yukawa coupling of the Higgs to the fermions is proportional to the mass of that fermion. The field redefinition is a change from a flavor eigenbasis, which is diagonal in the couplings to the gauge bosons, to a mass eigenbasis. In the mass eigenbasis the part of fermion Lagrangian which contains the interaction to the electroweak gauge bosons after SSB is

$$\begin{aligned} \mathcal{L}_F \supset & \sum_f (-Q_f) e \bar{f}_i \not{A} f_i + \sum_f \frac{e}{\sin \theta_W \cos \theta_W} \bar{f}_i (I_f^3 \gamma^\mu P_L - \sin^2 \theta_W Q_f \gamma^\mu) f_i Z_\mu \\ & + \frac{e}{\sqrt{2} \sin \theta_W} \left(\bar{u}_i \gamma^\mu P_L (V_{\text{CKM}})_{ij} d_j W_\mu^+ + \bar{d}_i \gamma^\mu P_L (V_{\text{CKM}}^\dagger)_{ij} u_j W_\mu^- \right) \\ & + \frac{e}{\sqrt{2} \sin \theta_W} \left(\bar{\nu}_i \gamma^\mu P_L (V_{\text{PMNS}}^\dagger)_{ij} l_j W_\mu^+ + \bar{l}_i \gamma^\mu P_L (V_{\text{PMNS}})_{ij} \nu_j W_\mu^- \right). \end{aligned} \quad (2.21)$$

Here we identified the electromagnetic coupling constant

$$e = \frac{g_2 g_Y}{\sqrt{g_2^2 + g_Y^2}}, \quad (2.22)$$

as the factor in front of the photon interaction term. The operators $P_{L,R}$ are just the projectors onto the left- and right-handed components

$$P_{L,R} = \frac{1 \mp \gamma^5}{2}. \quad (2.23)$$

The *CKM* and *PMNS matrices*³ are the results of the field redefinitions

$$V_{\text{CKM}} \equiv U_L^{u\dagger} U_L^d, \quad V_{\text{PMNS}} \equiv U_L^{l\dagger} U_L^\nu. \quad (2.24)$$

Typically, one prefers to work in the mass eigenbasis of the quarks, while the neutrinos are kept in the flavor eigenbasis, in which case one encounters flavor changes (*neutrino oscillations*) through propagation. This is why the PMNS matrix is defined in terms of the complex conjugate of the CKM matrix equivalent in the lepton sector.

2.2 CROSS SECTIONS

Cross sections offer the possibility to directly test the SM and many of the great successes of the SM are its *cross section* predictions. The cross section is simply defined as the probability to create some final state from some initial state per unit of time per target particle normalized by the incoming particle flux. This definition allows for straightforward measurement through counting experiments. For instance, experiments like **CMS** and **ATLAS** collide particles and count how often a particular final state is produced within a given time interval.

From a theoretical perspective, cross sections can be calculated using

$$d\sigma_{ij \rightarrow n} = \frac{1}{F} d\Phi_n |M_{ij \rightarrow n}|^2, \quad (2.25)$$

where F denotes the *flux factor*⁴

$$F \equiv 4p_1 \cdot p_2, \quad (2.26)$$

³ Named after Cabibbo, Kobayashi and Maskawa, and Pontecorvo, Maki, Nakagawa and Sakata.

⁴ In the following we assume that the initial state particles are massless.

$d\Phi_n$ is the *Lorentz invariant phase space measure*

$$d\Phi_n = \left[\prod_{i=1}^n \frac{d^4 q_i}{(2\pi)^4} (2\pi) \delta(q_i^2 - m_i^2) \Theta(q_i^0) \right] (2\pi)^4 \delta^{(4)} \left(p_1 + p_2 - \sum_{i=1}^n q_i \right), \quad (2.27)$$

and M_{fi} is the *scattering amplitude* describing the short distance interactions.

The computation of cross sections involves three basic steps:

1. Calculation of the hard scattering amplitude,
2. Phase-space integration,
3. And the convolution with *parton distribution functions* (PDFs).

We will discuss each step in detail below.

2.2.1 The Hard Scattering Amplitude

The Hard Scattering Amplitude describes the transition probability from a specific initial state to a particular final state. Since the scattering is **hard**, it implies that the energy transfer between particles during scattering is large compared to the QCD scale. Thus, we operate within the perturbative regime of QCD and can perform an expansion in terms of the coupling constant

$$M_{ij \rightarrow n} = \alpha_s^{n_{\text{Born}}} \left(M_{ij \rightarrow n}^{(0)} + \frac{\alpha_s}{\pi} M_{ij \rightarrow n}^{(1)} + \left(\frac{\alpha_s}{\pi} \right)^2 M_{ij \rightarrow n}^{(2)} + \mathcal{O}(\alpha_s^3) \right). \quad (2.28)$$

Here, n_{Born} denotes the power of the coupling constant at *leading order* (LO). The coefficients in this series can be computed graphically using *Feynman rules*. These are the set of all allowed propagators and vertices together with the corresponding mathematical prescription. The Feynman rules for the complete SM are listed in Appendix A. To calculate the coefficient $M_{ij \rightarrow n}^{(l)}$ for a specific process, one has to draw all possible connected and amputated Feynman diagrams with the initial state (i, j) and final state n , that contain $2(n_{\text{Born}} + l)$ vertices⁵. Then one uses the Feynman rules to get the mathematical translation, keeping in mind that momentum must be conserved at every vertex and also taking into account possible symmetry factors.

Starting from $M_{ij \rightarrow n}^{(1)}$, but for some processes, called *loop induced processes*, even from $M_{ij \rightarrow n}^{(0)}$, we will encounter loops in the diagrams. Inside a loop, the momentum of the edges cannot be uniquely determined through momentum conservation. Consequently, we must leave momentum unspecified and integrate over all possible values. Typically, it is the computation of these *loop integrals* that makes the calculation of hard scattering amplitudes so challenging. A plethora of powerful techniques has been developed over the years to tackle this daunting task. Still, the computation of loop integrals remains a highly active field of research and two-loop amplitudes with 5 or more scales are only just becoming available. A detailed description of modern techniques is beyond the scope of this thesis. For a comprehensive overview see Ref. [6].

Loop integrals are notorious for exhibiting divergences. To tame these, we introduce *regulators*, i.e. we introduce a parameter, such that the integral becomes function of that parameter with a singularity at the physical value. The most commonly used regularization scheme is

⁵ Quartic vertices are counted twice.

dimensional regularization (DR), here we make the loop-integral a function of the dimension by replacing

$$\int \frac{d^4k}{(2\pi)^4} (\dots) \longrightarrow \bar{\mu}^{2\epsilon} \int \frac{d^d k}{(2\pi)^d} (\dots), \quad d \equiv 4 - 2\epsilon \in \mathbb{C}, \quad \gamma_E = 0.5772 \dots \quad (2.29)$$

The dimensionally regularized integral satisfies the usual integral properties like linearity, translation invariance and rescaling. The mass scale,

$$\bar{\mu}^2 = \frac{\mu^2}{4\pi} e^{\gamma_E} \quad (2.30)$$

was introduced to retain the mass dimension of the measure to 4, while absorbing some common factors of loop integrals. The physical limit then corresponds to $\epsilon \rightarrow 0$. A divergent integral in four dimensions will hence have ϵ -poles in DR. The poles are categorized as *ultraviolet* poles if their origin are large loop momenta, i.e. the four dimensional integral diverges for $k \rightarrow \infty$. Further we categorize poles as *infrared* poles if the singularity arises from loop momenta which are either soft ($k \rightarrow 0$) or *collinear* ($k \cdot p_i \rightarrow 0$) to one of the external massless legs. UV and IR singularities are mutually exclusive since they originate from different regions of the phase space. This means that the poles do not multiply together, and we may only get a single UV pole per loop integration. The soft and collinear singularities are **not** exclusive, meaning that IR singularities can develop one double pole per loop integration.

The IR singularities cancel for inclusive observables as we shall discuss in detail in section 2.2.3. UV poles on the other hand, are removed through a method called *renormalization*. Renormalization hinges on the idea, that the fields, constants and masses we observe in nature are not necessarily the same as the one in our Lagrangian. Instead, they are related through a *renormalization constant*

$$\begin{aligned} W_\mu^{B,a} &= (Z_3^W)^{1/2} W_\mu^{R,a} \\ B_\mu^B &= (Z_3^Z)^{1/2} B_\mu^R \\ A_\mu^{B,a} &= (Z_3^A)^{1/2} A_\mu^{R,a} \\ \Phi^B &= (Z^\Phi)^{1/2} \Phi^R \\ Q_{iL}^B &= (Z_{2i}^L)^{1/2} Q_{iL}^R \\ u_{iR}^{B,a} &= (Z_{2i}^{u,R})^{1/2} u_{iR}^{B,a} \\ d_{iR}^{B,a} &= (Z_{2i}^{d,R})^{1/2} d_{iR}^{B,a} \\ g^B &= Z_g g^R \\ g_Y^B &= Z_Y g_Y^R \\ g_2^B &= Z_2 g_2^R \\ (\mu^2)^B &= Z_\mu (\mu^2)^R \\ \lambda^B &= Z_\lambda \lambda^R \\ y_{ij}^{d,B} &= Z_{y,ij}^d y_{ij}^{d,R} \\ y_{ij}^{u,B} &= Z_{y,ij}^u y_{ij}^{u,R} \end{aligned} \quad (2.31)$$

In these equations B refers to *bare* quantities appearing within our Lagrangian while R signifies renormalized quantities that are finite by definition. In the SM, it can be shown [7, 8] that we can choose renormalization constants, such that *Green's functions*, i.e. vacuum expectation values of time ordered products of local renormalized fields, are free of UV divergences. Scattering amplitudes, generally do not depend on the unphysical fields, which is why the fields can be kept unrenormalized in this case. Since at LO Green's functions do not require renormalization, all renormalization constants are equal to the identity at this order.

The definition of the renormalization constants is not unique. Indeed, the renormalization constants were designed to absorb singularities, but the finite part is a priori unconstrained. We call a prescription which uniquely determines the renormalization constants a *renormalization scheme*. The most widely used renormalization scheme is the $\overline{\text{MS}}$ scheme. Here, beyond the leading 1 and a universal factor of $\bar{\mu}^{\epsilon\rho_i}$, the renormalization constants **only** consist of poles, i.e. the renormalization constants have the structure

$$Z_i(\alpha) = \bar{\mu}^{\epsilon\rho_i} \left(1 + \frac{z_1}{\epsilon} \frac{\alpha}{4\pi} + \left(\frac{z_{22}}{\epsilon^2} + \frac{z_{21}}{\epsilon} \right) \left(\frac{\alpha}{4\pi} \right)^2 + \dots \right). \quad (2.32)$$

ρ_i is the mass dimension of the operator in units of ϵ , so that the factor $\bar{\mu}^{\epsilon\rho_i}$ corrects for the mismatch in mass dimensions between the four-dimensional renormalized and the d -dimensional bare quantities. For example: the coupling constant g^B has mass dimension ϵ , hence the renormalized coupling g^R has mass dimension zero and $\rho_i = 1$.

$\overline{\text{MS}}$ -renormalized masses are generally different from the pole mass. The *on-shell renormalization* (OS) scheme, is an alternative to the $\overline{\text{MS}}$ scheme specifically designed, such that the renormalized mass matches the pole mass. It is therefore the suitable choice for external particles that are asymptotically free. Bare quantities are independent of the chosen renormalization scheme. The invariance under the change of the renormalization scheme defines a group, the *renormalization group* (RG). In the $\overline{\text{MS}}$ scheme, the change from one scale $\bar{\mu}$ to another defines a continuous subgroup of the RG. This means we can formulate the invariance in terms of a differential equation

$$0 = \frac{d}{d \log \mu} a^B = a^R \frac{dZ_a^{\overline{\text{MS}}}}{d \log \mu} + Z_a^{\overline{\text{MS}}} \frac{da^R}{d \log \mu}, \quad (2.33)$$

where a could be a mass or a coupling. Eq. (2.33) is called the *renormalization group equation* (RGE) and it can be leveraged to determine the scale dependence, also called the *running*, of the observable.

The final step in calculating the hard scattering amplitude involves the application of the *Lehmann-Symanzik-Zimmermann* (LSZ) reduction formula. It relates the scattering amplitudes to Green's functions, and it is the reason why we only considered amputated Feynman diagrams. In practice, one just has to multiply each external field with the square root of the corresponding LSZ constant. These constants are defined as the proportionality factor between the propagator of the interacting and the free theory⁶. As such, they are numerically identical to the OS field renormalization constants.

⁶ The interacting field theory might have an additional continuous spectrum.

2.2.2 The Parton Distribution Functions

In hadron collisions, the initial state is not made up of elementary particles, but are bound states thereof. This means that during an inelastic scattering event, the partons which take part in the short-range interaction only carry a fraction of the original hadron momentum

$$p_1 = x_1 P_1, \quad p_2 = x_2 P_2. \quad (2.34)$$

Here p_1 and p_2 denote the momenta of the partons and P_1 and P_2 are the momenta of the hadrons. Since the momentum of the parton can not be larger than that of the hadron, $x_{1,2}$ is restricted to be less than one. Furthermore, since the energy of the parton must be positive the momentum fraction must also be positive. Otherwise, the momentum fraction is a priori unconstrained, we therefore integrate over all allowed values of x_1 and x_2

$$\begin{aligned} d\sigma_{H_1 H_2 \rightarrow n}(S) &= \int_0^1 dx_1 dx_2 f_{H_1,i}(x_1) f_{H_2,j}(x_2) d\hat{\sigma}_{ij \rightarrow n}(x_1 P_1, x_2 P_2, \mu_R) \\ &= \int_0^1 \frac{d\tau}{\tau} \mathcal{L}_{ij}(\tau) d\hat{\sigma}_{ij \rightarrow n}(\tau S, \mu_R) \end{aligned} \quad (2.35)$$

where $S = 2P_1 \cdot P_2$ is hadronic center of mass energy. $f_{H_k,i}(x_k)$ are the (unrenormalized) *parton distribution functions* (PDFs). They describe the probability of finding a parton i with momentum fraction x_k inside the hadron H_k . Lorentz invariance of the partonic cross section allowed us to conclude that it can only depend on the partonic center of mass energy \hat{s}

$$d\hat{\sigma}_{ij \rightarrow n}(x_1 P_1, x_2 P_2, \mu_R) = d\hat{\sigma}_{ij \rightarrow n}(x_1 x_2 S, \mu_R). \quad (2.36)$$

We then defined the *partonic luminosity*

$$\mathcal{L}_{ij}(\tau) \equiv (\tilde{f}_{H_1,i} \otimes \tilde{f}_{H_2,j})(\tau) \equiv \int_0^1 dx_1 dx_2 \tilde{f}_{H_1,i}(x_1) \tilde{f}_{H_2,j}(x_2) \delta(\tau - x_1 x_2), \quad (2.37)$$

where $\tilde{f}_{H,i}(x) \equiv x f_{H,i}(x)$, to arrive at the second line of Eq. (2.35).

At this stage the partonic cross section can still exhibit singularities whenever a final state parton becomes collinear to one of the initial state partons. At LO for example, the divergence due to initial-state collinear emissions reads

$$d\hat{\sigma}_{ab \rightarrow cX}(s, \mu_R) \Big|_{\text{div.}} = -\frac{\alpha_s}{2\pi} \frac{1}{\epsilon} \int_0^1 dz \left(P_{db}^{(0)}(z) d\hat{\sigma}_{ad \rightarrow X}(zs, \mu_R) + P_{da}^{(0)}(z) d\hat{\sigma}_{db \rightarrow X}(zs, \mu_R) \right), \quad (2.38)$$

where $P_{ij}^{(0)}$ are the LO *Altarelli-Parisi splitting kernels*⁷:

$$\begin{aligned} P_{qq}^{(0)}(x) &= C_F \left[\frac{1+x^2}{(1-x)_+} + \frac{3}{2} \delta(1-x) \right], \\ P_{qg}^{(0)}(x) &= T_F [x^2 + (1-x)^2], \\ P_{gq}^{(0)}(x) &= C_F \left[\frac{1+(1-x)^2}{x} \right], \\ P_{gg}^{(0)}(x) &= 2C_A \left[\frac{x}{(1-x)_+} + \frac{1-x}{x} + x(1-x) \right] + \delta(1-x) \frac{\beta_0}{2}. \end{aligned} \quad (2.39)$$

⁷ The definition of β_0 can be found in Eq. (4.51)

We absorb these collinear singularities into the PDFs through a process called *collinear renormalization*, by defining the renormalized PDFs $f_{H,i}(x, \mu_F)$ via

$$f_{H,i}(x) \equiv (Z_{ij}(\cdot, \mu_F) \otimes f_{H,j}(\cdot, \mu_F))(x). \quad (2.40)$$

Beyond the pole term, the renormalization constants are generally scheme dependent. From Eq. (2.38) we see that the $\overline{\text{MS}}$ renormalization constant at NLO are given by

$$Z_{ij}(z, \mu_R, \mu_F) = \delta(1-z)\delta_{ij} + \frac{\alpha_s}{2\pi} \frac{1}{\epsilon} P_{ij}^{(0)}(z) + \mathcal{O}(\alpha_s^2). \quad (2.41)$$

Now the sum

$$d\sigma_{H_1 H_2 \rightarrow cX} + d\sigma_{H_1 H_2 \rightarrow X} \quad (2.42)$$

is guaranteed to be free initial-state collinear divergences.

Since the initial state collinear divergences are of a completely different origin than the UV divergences, we introduce a new scale μ_F , called the factorization scale. This scale separates the long-distance (non-perturbative) physics, contained in the PDFs, from the short-distance (perturbative) physics, contained in the partonic cross sections.



Figure 2.2: The various PDFs multiplied by x as a function of x . The plot was created using the LHAPDF6 [9] interface to the NNPDF31_nnlo_as_0118 [10] PDF set at a scale of $\mu_F = m_H/2$.



Figure 2.3: Displayed is the partonic luminosity for combinations of various partons. The luminosities are defined as $\mathcal{L}_{qg} = 2 \times \sum_i (\mathcal{L}_{q_i g} + \mathcal{L}_{\bar{q}_i g})$, $\mathcal{L}_{q\bar{q}} = 2 \times \sum_i \mathcal{L}_{q_i \bar{q}_i}$, $\mathcal{L}_{qq'} = \sum_{i,j} (\mathcal{L}_{q_i q_j} + \mathcal{L}_{q_i \bar{q}_j} + \mathcal{L}_{\bar{q}_i \bar{q}_j}) - \mathcal{L}_{q\bar{q}}$. The setup is the same as in Fig. 2.2.

The factorization theorem (2.35) is central in the SM as it tells us that the PDFs are universal quantities, i.e. they are not specific to any one process. It is a postulate of the parton model, in which hadrons are thought of as collection of the free elementary particles. In QCD however, the

theorem requires proof [11]! The PDF for all light partons are displayed in Fig. 2.2. In Fig. 2.3 we show the partonic luminosity for exemplary parton combinations. PDFs describe long range interactions, a regime in which QCD is non-perturbative. As such, PDFs are non-perturbative objects which have to be measured in experiments or be calculated non-perturbatively, e.g. on the lattice.

The factorization scale is unphysical in the sense that it is not a parameter in our theory, nor can it be measured in an experiment. As usual we can apply the RGE to determine the running of the renormalized PDFs

$$0 = \frac{d}{d \ln \mu_F} f_{H,i}(x) = \frac{d}{d \ln \mu_F} (Z_{ij} \otimes f_{H,j}(\cdot, \mu_F))(x). \quad (2.43)$$

This can be rewritten to

$$\begin{aligned} \frac{d f_{H,i}(x, \mu_F)}{d \ln \mu_F} &= 2\alpha_s \left(Z_{ij}^{-1} \otimes \frac{d Z_{jk}^{(1)}}{d \alpha_s} \otimes f_{H,k}(\cdot, \mu_F) \right) (x, \mu_F) \\ &= \frac{\alpha_s}{\pi} \left(P_{ij}^{(0)} \otimes f_{H,j}(\cdot, \mu_F) \right) (x) + \mathcal{O}(\alpha_s^2), \end{aligned} \quad (2.44)$$

where $Z_{ij}^{(1)}$ is the residue of the renormalization constant. So even though the PDFs are non-perturbative, their dependence on the factorization scale is. Eq. (2.44) is the famous *Dokshitzer-Gribov-Lipatow-Altarelli-Parisi-evolution equation* (DGLAP equations) [12, 13, 14].

In the derivation above, we have treated the partons inside the hadrons as massless, which leads to real collinear singularities. In reality, all quarks have finite masses, so the phase-space integration only yields logarithmic mass enhancements of the form $\ln(\hat{s}/m_q^2)$ instead of actual singularities. The DGLAP equations then automatically resum these logarithms. For most applications at the LHC, the typical hard scattering scale is orders of magnitudes larger than all quark masses except for the top quark mass. It is therefore beneficial to treat them as massless partons, as the appearance of the large logarithms would otherwise completely destroy the perturbative convergence. However, treating quarks as massless also implies that we neglect their mass-dependent effects in the hard-scattering matrix elements. If the scattering process is sensitive to the quark masses—for example, in processes involving Higgs couplings to quarks—these mass effects might be lost.

The number of quark flavors treated as active (massless) partons defines our *flavor scheme* (FS). For instance, if we treat the lightest four flavors (up, down, strange, charm) as massless, while considering the bottom and top quarks as massive, we are working in the 4FS. Analogously, if the bottom quark is also considered massless, we are working in the 5FS, and so on.

2.2.3 The Phase-Space Integration

Even after renormalization and collinear renormalization can the amplitude exhibit divergences. The scattering amplitude in and of itself is not a physical observable; therefore, it is not required to be finite. Physical observables are cross sections, which are obtained by performing phase-space integrations over the squared amplitudes. However, even after integrating over the phase space, the cross section is not guaranteed to be finite. The reason is that the Born process is indistinguishable from processes with additional infrared radiation. Indeed, no

matter how precise a detector is, below a certain resolution, it becomes impossible to detect a very soft photon or to distinguish two highly collinear jets. Hence, computing a cross section with a fixed final state does not make physical sense. Instead, one must consider sufficiently inclusive observables—so called *IR-safe observables*. For these, Kinoshita, Lee and Nauenberg proved that in unitary theories all IR singularities cancel [15, 16]. This is known as the Kinoshita-Lee-Nauenberg (KLN) theorem.

An example of an observable which is trivially IR safe is the fully inclusive cross section

$$\hat{\sigma}_{ij \rightarrow n+X} = \sum_{k=1}^{\infty} \hat{\sigma}_{ij \rightarrow n+k}, \quad \text{for } \hat{\sigma}_{ij \rightarrow n}^{(0)} \text{ finite}, \quad (2.45)$$

where $n+k$ indicates that in addition to the final state n we now have k massless partons of whatever flavor. In perturbation theory, the infinite sum is truncated at a given order and at each order

$$\hat{\sigma}_{ij \rightarrow n+X}^{(l)} = \sum_{k=0}^l \hat{\sigma}_{ij \rightarrow n+k}^{(l-k)}, \quad (2.46)$$

summed together with the contribution from collinear renormalization will be finite. For example at NLO, the finite inclusive cross section reads

$$\hat{\sigma}_{ij \rightarrow n+X}^{(1)} = \hat{\sigma}_{ij \rightarrow n}^R + \hat{\sigma}_{ij \rightarrow n}^V + \hat{\sigma}_{ij \rightarrow n}^C, \quad (2.47)$$

where

$$\hat{\sigma}_{ij \rightarrow n}^R = \frac{1}{F} \int d\Phi_{n+1} \sum_c |M_{ij \rightarrow n+c}^{(0)}|^2 \quad (2.48)$$

is the real correction,

$$\hat{\sigma}_{ij \rightarrow n}^V = \frac{1}{F} \int d\Phi_n 2\text{Re} \left(\left(M_{ij \rightarrow n}^{(0)} \right)^* M_{ij \rightarrow n}^{(1)} \right) \quad (2.49)$$

is the virtual correction, and

$$\hat{\sigma}_{ij \rightarrow n}^C = \frac{1}{F} \int d\Phi_n \frac{\alpha_s}{2\pi} \frac{1}{\epsilon} \left(\frac{\mu_R^2}{\mu_F^2} \right)^\epsilon \sum_c \int_0^1 dz \left[P_{ci}^{(0)}(z) |M_{cj \rightarrow n}^{(0)}|^2 + P_{cj}^{(0)}(z) |M_{ic \rightarrow n}^{(0)}|^2 \right] \quad (2.50)$$

are the corrections from collinear renormalization. Figure 2.4 provides a pictorial representation of the required partonic cross sections for Higgs boson production in the gluon fusion channel at various perturbative orders.

Although the sum of the contributions to the cross section is guaranteed to be finite due to the KLN theorem, the presence of IR singularities in individual terms poses significant challenges for practical calculations. These singularities prevent a straightforward evaluation of the phase-space integrals. To overcome this, we once again have to introduce regulators (such as dimensional regularization) to make the integrals well-defined. Over the years, numerous techniques have been developed to compute phase-space integrals efficiently. These techniques can generally be categorized into two main types: *Analytic methods*, and *numerical methods*.

As the name suggests, in the former class, the phase-space integrals are solved analytically. One noteworthy member of this class is the *reverse-unitarity method* [17], which was first applied to Higgs production in the gluon fusion channel. The method uses unitarity, to rewrite the phase-space integrals in terms of loop integrals over cut-propagators. One can then apply the remarkable techniques developed for Feynman integrals to these phase-space integrals and



Figure 2.4: Pictorial representation of the needed partonic cross sections at various perturbative orders of the fully inclusive hadronic cross section. The graphic shows the example of Higgs production in the gluon fusion channel.

solve them analytically. The mayor downside of this approach is that it is highly process and observable dependent, meaning that for every process and every observable we have to start over from scratch. Furthermore, by the very nature of the method, you are always restricted to inclusive jet observables. Nevertheless, it has been successfully applied to, among others, Higgs-rapidity and Higgs- p_T distributions [18].

Among the numerical methods, there are two mayor approaches: *slicing* and *subtraction methods*. The former rely on a variable that isolates the IR-sensitive region of the phase space. Consider once again the example of Higgs production. Here, the IR-sensitive region of the phase space corresponds to configurations where the transverse momentum of the Higgs boson, p_T , approaches zero. The phase-space integral can then be decomposed into

$$\int_0^{p_T} dk_T d\hat{\sigma}_{ij \rightarrow H+c} = \int_0^{p_T^{\text{cut}}} dk_T d\hat{\sigma}_{ij \rightarrow H+c} + \int_{p_T^{\text{cut}}}^{p_T} dk_T d\hat{\sigma}_{ij \rightarrow H+c}. \quad (2.51)$$

The first integral on the right-hand side is now finite and can be computed numerically, e.g. using *Monte-Carlo* (MC) techniques. If we choose p_T^{cut} small enough, then we can approximate the integrand in the second integral, by its IR limit and solve the integral analytically. The pole of the integral should then cancel against the poles in the virtual integration and the counter term from collinear renormalization. The mayor advantage of this method is its simplicity. One big downside is its dependence on the unphysical cutoff scale. Ideally it is chosen very small, such that the approximation introduces little to no error. But if chosen too small, the

integrations will have huge logarithmic enhancements which can easily spoil the numerical precision. Another disadvantage is that not all processes or observables have easily identifiable slicing variables, or the analytic integration is very challenging. For example, p_T slicing only works for color singlet production, indeed if we have a jet in the final state, we can encounter collinear divergences also at finite transverse momenta of the jet. For processes involving jets, a possible slicing variable is the N -jettiness

$$\mathcal{T}_N \equiv \sum_k \min_i \left\{ \frac{2p_i \cdot q_k}{Q_i} \right\}, \quad (2.52)$$

with N , the number of jets, q_k , the momenta of the unresolved partons, p_i , the momenta of the resolved jets, and Q_i a normalization factor which can for example be set to the jet energy. However, the analytic integration becomes highly non-trivial and is a matter of active research. Currently, the N -jettiness beam functions are known at N³LO [19], the 0-jettiness soft function is known at N³LO [20, 21] and NNLO 1-jettiness soft functions and jet functions are also known [22, 23, 24, 25].

Subtraction methods on the other hand, work by subtracting the infrared limits at the integrand level. In the *Frixione-Kunszt-Signer subtraction scheme* (FKS subtraction scheme) one first isolates the IR divergence by partitioning the phase space into *sectors* using *selector functions*. These functions isolate specific infrared limits by approaching unity when a particular limit is approached (e.g., when an unresolved parton becomes soft or collinear) and vanish in other limits. For a single unresolved parton, a possible selector function is

$$\mathcal{S}_{n+1,k} \equiv \frac{1}{d_{n+1,k}} \left(\sum_k \frac{1}{d_{n+1,k}} \right)^{-1}, \quad \text{where} \quad d_{n+1,k} \equiv \left(\frac{E_{n+1}}{\sqrt{\hat{s}}} \right)^\alpha (1 - \cos \theta_{n+1,k})^\beta. \quad (2.53)$$

The first index $n+1$ is the index of the unresolved parton, while the second index is the index of the reference parton. E_{n+1} denotes the energy of the unresolved parton, this factor is therefore to identify soft singularities. Consequently, the power α can be set to zero if the unresolved parton is a quark. Other than that, the powers must be strictly positive $\alpha, \beta > 0$. If $n+1$ now becomes collinear to one of the partons, say parton i , then the selector function $\mathcal{S}_{n+1,i}$ will approach one. And since the selector functions are strictly positive and form a decomposition of unity

$$\sum_k \mathcal{S}_{n+1,k} = 1, \quad (2.54)$$

all other selector functions will go to zero simultaneously.

The real emission cross section can then be written as a sum over sectors:

$$\hat{\sigma}_{ij \rightarrow n+u} = \frac{1}{F} \sum_k \int d\Phi_{n+1} |M_{ij \rightarrow n+u}^{(0)}|^2 \mathcal{S}_{n+1,k}. \quad (2.55)$$

Now say we found a way to factorize the phase space, such that the infrared limits of a specific sector, are isolated (see for example Ref. [26]). Then in each sector, we will have two unit integrations over ξ and η which parameterize the soft and collinear limit respectively, i.e. if $\xi \rightarrow 0$, then the momentum of the unresolved parton goes to zero and if $\eta \rightarrow 0$, the unresolved parton will become collinear to the reference momentum of that sector. The amplitude has the singular scaling $|M_{ij \rightarrow n+u}^{(0)}|^2 \sim \xi^{-2} \eta^{-1}$, leading to an integral of the form

$$\int_0^1 \frac{d\eta}{\eta^{1+\epsilon}} \frac{d\xi}{\xi^{1+2\epsilon}} f(\eta, \xi, \dots), \quad (2.56)$$

where f is a function regular in the limits $\eta, \xi \rightarrow 0$. If we now apply the distributional identity

$$\frac{1}{x^{1-\epsilon}} = \frac{1}{\epsilon} \delta(x) + \sum_{k=0} \frac{\epsilon^k}{k!} \left(\frac{\ln^k x}{x} \right)_+, \quad (2.57)$$

we can explicitly carry out all integrations.

The *sector improved residue subtraction scheme* [27] extends the FKS subtraction scheme to NNLO. As of today, it is the only subtraction scheme capable of computing any QCD phase-space integral. Beyond NNLO, developing efficient and general subtraction schemes remains an open challenge in perturbative QCD.

3

THE HIGGS AS A WINDOW TO NEW PHYSICS

As we saw in the previous chapter, the Higgs boson has a very special place in the SM, giving rise to the masses of all other elementary particles. But the fascinating properties of the Higgs boson do not end with the SM. In fact many of the properties of the Higgs boson puzzle physicists to this day, but they can also serve as guidelines to look for physics beyond the SM. The minimal supersymmetric SM (MSSM) for example was primarily proposed to solve the hierarchy problem, i.e. the problem of why the Higgs mass is so much smaller than the Planck scale. Furthermore, state-of-the-art measurements hint towards a metastable Higgs potential, meaning that the universe could at some point transition to a new VEV. The Higgs is also an excellent candidate as a portal to a hidden dark sector, thus possibly explaining the origin of dark matter DM.

Although by no means a complete list of Higgs physics research, we want to highlight these three fields—the Higgs portal to DM, the stability of the Higgs potential, and the Hierarchy problem—and briefly review them in the following chapter. It will also underscore the importance of precision calculations in the SM

3.1 HIGGS PORTAL

Every particle in the SM was uniquely characterized by its mass, spin, the various quantum numbers under the $SU(3)_C \times SU(2)_L \times U(1)$ gauge group. For example, the left-handed up-quark is in a color triplet, has isospin $+1/2$, and weak hypercharge $4/3$, whereas the right-handed electron is charged only under the $U(1)$ group, with hypercharge -2 . It is therefore conceivable, maybe even plausible, that particles could be neutral with respect to all SM gauge interactions. In fact, the right-handed neutrino we introduced in section 2.1 was exactly that. Furthermore, there is strong astrophysical and cosmological evidence for the existence of additional matter that does not, or at least not often, interact with the SM (see Ref. [28] for an overview). This type of matter has the oblique name: dark matter. The nature of this type of matter is still an open question in physics, and countless models have been proposed, explaining it.

In this context, a frequently broad up type of model, are so Higgs-portal models. Here, the DM interacts with SM primarily via Higgs, thus explaining the name. This way, two SM, could annihilate into two DM particles for instance (see Fig. 3.1).

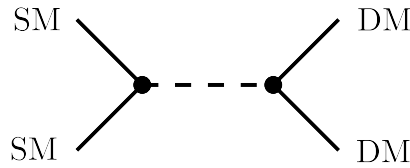


Figure 3.1: Feynman diagram of SM particles decaying into DM particles via a Higgs portal.

Since the DM is a singlet with respect to the $SU(2) \times U(1)$ group, a mass term would not generally break the gauge invariance, i.e. the mass of the DM particles does not have to be, or at least not exclusively, generated through the Higgs mechanism. The Lagrangian of a real scalar, a *Dirac fermion*, and a real vector DM field can therefore have the general structure

$$\begin{aligned}\mathcal{L}_S &= \frac{1}{2} (\partial_\mu S \partial^\mu S - M_S^2 S^2) - \frac{1}{4} \lambda_S S^4 - \frac{1}{4} \lambda_{HSS} \Phi^\dagger \Phi S^2, \\ \mathcal{L}_\chi &= \bar{\chi} (i \not{\partial} - M_\chi) \chi - \frac{1}{2} \frac{\lambda_{H\chi\chi}}{\Lambda} \Phi^\dagger \Phi \bar{\chi} \chi, \\ \mathcal{L}_V &= -\frac{1}{4} V_{\mu\nu} V^{\mu\nu} + \frac{1}{2} M_V^2 V_\mu V^\mu + \frac{1}{4} \lambda_V (V_\mu V^\mu)^2 + \frac{1}{4} \lambda_{HVV} \Phi^\dagger \Phi V_\mu V^\mu, \quad V_{\mu\nu} = \partial_\mu V_\nu - \partial_\nu V_\mu.\end{aligned}\tag{3.1}$$

Here, λ_{HSS} , $\lambda_{H\chi\chi}$, and λ_{HVV} are the dimensionless couplings of the particles to the Higgs, while Λ is the new physics scale. The self-interaction terms proportional to S^4 and V^2 are not important for our purposes. To arrive at Eq. (3.1), we postulated, that the Lagrangians respect a \mathbb{Z}_2 symmetry, that is the symmetry under which all SM particles are symmetric, and all DM particles are antisymmetric. This way, it is ensured, that every vertex must have an even number of DM particles. Consequently, the lightest new particle will be stable, and hence present an excellent DM candidate. The Lagrangian of a *Majorana fermion* would be $1/2 \mathcal{L}_\chi$. Notably, the fermion Lagrangian is not renormalizable, due to the dimensionful coupling introduced by the new physics scale Λ . Nevertheless, the effective Lagrangian is rather convenient to parametrize the effects of new physics at some higher scale. The masses of the new particles are now generated partly through the Higgs mechanism, and partly through plain mass terms, such that the total masses reads

$$\begin{aligned}m_S^2 &= M_S^2 + \frac{1}{4} \lambda_{HSS} v^2, \\ m_\chi &= M_\chi + \frac{1}{4} \frac{\lambda_{H\chi\chi}}{\Lambda} v^2, \\ m_V^2 &= M_V^2 + \frac{1}{4} \lambda_{HVV} v^2.\end{aligned}\tag{3.2}$$

If the DM particle, has a mass less than $m_H/2$, then the Higgs can decay into a DM final state, altering the decay width of the Higgs. The partial decay widths read¹

$$\begin{aligned}\Gamma(H \rightarrow SS) &= \frac{\lambda_{HSS}^2 v^2}{128\pi m_H} \sqrt{1 - \frac{4m_S^2}{m_H^2}}, \\ \Gamma(H \rightarrow VV) &= \frac{\lambda_{HVV}^2 v^2 m_H^2}{512\pi m_V^4} \sqrt{1 - \frac{4m_V^2}{m_H^2}} \left(1 - 4\frac{m_V^2}{m_H^2} + 12\frac{m_V^4}{m_H^4}\right), \\ \Gamma(H \rightarrow \bar{\chi}\chi) &= \frac{\lambda_{H\chi\chi}^2 v^2 m_H}{32\pi \Lambda^2} \left(1 - \frac{4m_\chi^2}{m_H^2}\right)^{3/2}.\end{aligned}\tag{3.3}$$

For a Higgs decay into Majorana fermions the decay width is $1/2 \Gamma(H \rightarrow \bar{\chi}\chi)$.

¹ We note that in Ref. [29] the $H \rightarrow VV$ decay width contains M_V instead of m_V , which we believe to be a typo, since it does not match the results presented in Ref. [30]. Furthermore, in cases where the final state contains identical particles, our results differ by a factor of $1/2$ from Refs. [29, 30]. We suspect that this is due a double counting of the phase-space by the authors.

At colliders like the LHC, one can look for these invisible decays, either directly by looking for missing transverse momentum [31, 32], or indirectly by looking for modifications on the decay width [33, 34]. In both, the branching ratio of Higgs to invisible is constrained by

$$\text{BR}(H \rightarrow \text{inv}) < 20\% \quad (3.4)$$

at the 95% confidence level. This limit is likely to go down to 10% with the inclusion of the run 3 data set, and could even reach a sensitivity of 5% with data from the high-luminosity LHC [35, 36, 37]. With the partial decay widths in Eq. (3.3), we can then derive exclusion bounds on the existence of DM. The results are presented in Fig. 3.2.

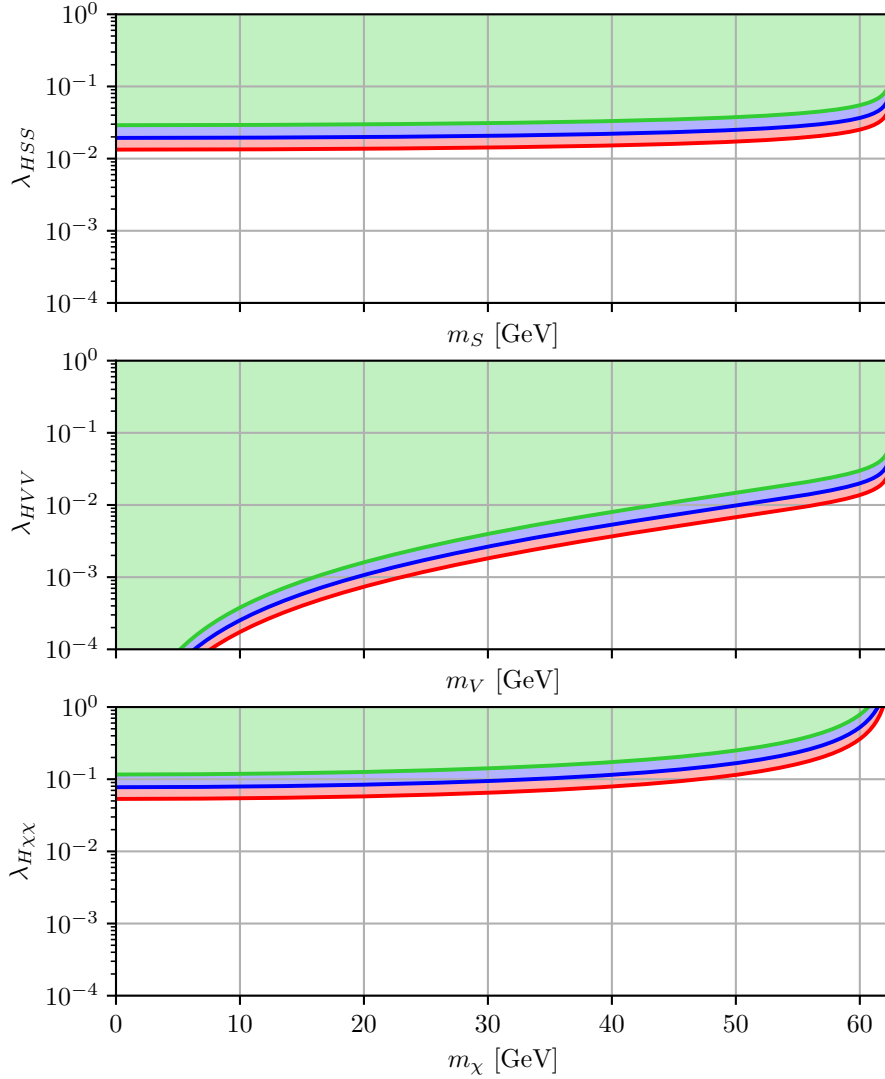


Figure 3.2: Exclusion bounds on the existence of scalar (top panel), vector (middle panel), and fermionic (bottom panel) DM derived by searches for invisible Higgs decays based on the 20% (green) threshold found with current data, the expected 10% (blue) threshold with the Run III data, and the 5% (red) projection for the High-luminosity LHC. The colored areas imply the exclusion of the particle at the 95% confidence level. The computational setup is described in the conventions. The SM decay width was set to $\Gamma_{\text{SM}} = 4.07$ MeV.

3.2 STABILITY OF THE HIGGS POTENTIAL

3.3 THE HIERARCHY PROBLEM

4

HADRONIC HIGGS PRODUCTION

In hadron-hadron collision, a single Higgs boson can be produced in five different channels, namely (sorted in descending order according to their cross sections):

1. Gluon-gluon fusion ($pp \rightarrow H$),
2. Vector-boson fusion ($ppH \rightarrow qqH$),
3. Higgs Strahlung ($pp \rightarrow WH$ or $pp \rightarrow ZH$),
4. $t\bar{t}$ or $b\bar{b}$ associated production ($pp \rightarrow t\bar{t}H$, or $b\bar{b}H$),
5. Single-top associated production ($pp \rightarrow tH$).

The corresponding LO Feynman diagrams are depicted in Fig. 4.1. The production channels

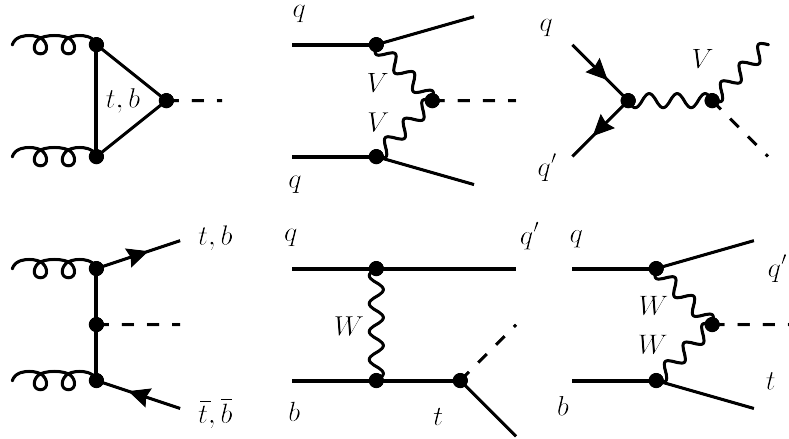


Figure 4.1: All LO Feynman diagrams for the various hadronic Higgs-production channels. From top-left to bottom-right: gluon-gluon fusion, vector-boson fusion, Higgs Strahlung, $t\bar{t}$ or $b\bar{b}$ associated production, and the last two diagrams correspond to single-top associated production. V labels electroweak vector bosons, i.e. either a Z or W boson. In case a fermion line is drawn without an arrow, it indicates that fermion flows are valid. q and q' marks massless quarks.

have cross sections across nearly three orders of magnitude. At the bottom end, there is the single-top associated Higgs production with a cross section with just 0.85 pb at 13 TeV. It is the only of the above channels which has not yet been observed at the LHC. $t\bar{t}H$ and $b\bar{b}H$ are the next rarest production channels with cross sections of 2.6 pb, closely followed by the two Higgs-Strahlung processes $pp \rightarrow WH$ and $pp \rightarrow ZH$. With a cross section of 3.8 pb, the vector-boson fusion is the second most likely production mechanism. But all other channels are dwarfed compared to the gluon-gluon fusion channel with a cross section of approximately 46 pb, making up for almost 90% of all produced Higgs bosons at the LHC. The comparably

high cross section, has enabled experimentalist to determine the cross section with incredible precision. Today, its most precise determination is¹ [38]

$$\sigma_{pp \rightarrow H}(13 \text{ TeV}) = 47.1 \pm 3.8 (\pm 8\%) \text{ pb.} \quad (4.1)$$

In the highly accurate narrow width approximation $\Gamma_H/m_H \ll 1$, subsequent decays of the Higgs boson can be approximated via

$$\sigma_{pp \rightarrow H \rightarrow X} = \sigma_{pp \rightarrow H} \frac{\Gamma_{H \rightarrow X}}{\Gamma_H}, \quad (4.2)$$

where Γ_H is the total decay width of the Higgs. In the high-luminosity phase of the LHC, the cross section for the production of a Higgs and its subsequent decay are expected to be reduced even further (see Tab. 4.1).

Decay Mode	CMS [%]	ATLAS [%]
$H \rightarrow \gamma\gamma$	$\pm 2 \text{ (stat.) } \pm 3 \text{ (sys.)}$	$\pm 2 \text{ (stat.) } \pm 3 \text{ (sys.)}$
$H \rightarrow ZZ^*$	$\pm 2 \text{ (stat.) } \pm 3 \text{ (sys.)}$	$\pm 2 \text{ (stat.) } \pm 4 \text{ (sys.)}$
$H \rightarrow WW^*$	$\pm 1 \text{ (stat.) } \pm 3 \text{ (sys.)}$	$\pm 1 \text{ (stat.) } \pm 4 \text{ (sys.)}$
$H \rightarrow b\bar{b}$	$\pm 3 \text{ (stat.) } \pm 5 \text{ (sys.)}$	$\pm 3 \text{ (stat.) } \pm 4 \text{ (sys.)}$
$H \rightarrow \mu^+\mu^-$	$\pm 9 \text{ (stat.) } \pm 2 \text{ (sys.)}$	$^{+12}_{-13} \text{ (stat.) } \pm 3 \text{ (sys.)}$
$H \rightarrow \tau\tau$	$\pm 3 \text{ (stat.) } \pm 5 \text{ (sys.)}$	$\pm 3 \text{ (stat.) } ^{+12}_{-10} \text{ (sys.)}$

Table 4.1: Projected relative statistical and systematic uncertainties on the Higgs production cross section in the gluon-gluon fusion channel with its subsequent decay for the high luminosity phase of the LHC according to Ref. [37].

For any search for new physics, experimental measurements have to be compared to theory predictions. The more precise the measurements and predictions, the more sensitive we are to new physics, and the tighter we can constrain extensions of the SM. The discovery of the Higgs boson in 2012 [39, 40], has therefore triggered a never ending hunt for increased precision, both on the experimental and the theory side. Being the most precisely measured, the gluon-gluon fusion channel is especially vital to pin down theoretical.

In what follows, we focus on the gluon-gluon fusion channel exclusively. We will present explicit calculations for the LO and approximate NLO cross section, and provide an overview on the current theoretical status and remaining challenges of this channel.

4.1 THE LEADING-ORDER CROSS SECTION

Having established, that the gluon-fusion Higgs production cross section is central for many phenomenological applications, we now want to perform the actual LO calculation, which was first demonstrated by Georgi et al. in 1978 [41]. The calculation not only serves as an instructive example on cross section calculation, and thereby allows us to put our experience from section 2.2 to good use, but it already introduces many important concepts we can transfer to the NNLO computation.

At LO, there are only two possible Feynman diagrams we can draw. They are depicted in Fig. 4.2. As we can see. Gluon-fusion is a loop induced process with two scales: the mass of

¹ This is assuming SM branching ratios.

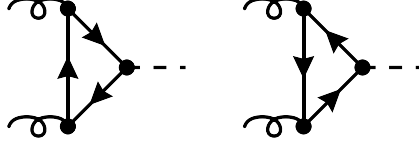


Figure 4.2: LO Feynman diagrams for Higgs production in the gluon-fusion channel.

the quark running in the loop m_q , and the Higgs mass m_H which must simultaneously be the partonic center of mass energy. The initial state gluons carry on the on-shell momenta p_1 and p_2 . Let us then define

$$i\mathcal{M} = i\mathcal{M}^{\mu\nu,ab}\varepsilon_\mu^a(p_1)\varepsilon_\nu^b(p_2). \quad (4.3)$$

With the Feynman rules presented in appendix A we find

$$\begin{aligned} i\mathcal{M}^{\mu\nu,ab} = & - \int \frac{d^4k}{(2\pi)^4} \\ & \times \text{Tr} \left[\frac{-im_q}{v} \delta_{ij} \frac{i(\not{k} + \not{p}_1 + \not{p}_2 + m_q)}{(k + p_1 + p_2)^2 - m_q^2} (ig\gamma^\nu T_{ik}^a) \frac{i(\not{k} + \not{p}_1 + m_q)}{(k + p_1)^2 - m_q^2} (ig\gamma^\mu T_{kj}^b) \frac{i(\not{k} + m_q)}{k^2 - m_q^2} \right] \\ & + \{p_1 \longleftrightarrow p_2, \mu \longleftrightarrow \nu, a \longleftrightarrow b\}, \end{aligned} \quad (4.4)$$

where the extra minus sign in front stems from the fermion trace.

Even without performing the explicit calculation can we already anticipate the general structure of the amplitude. Color wise, the amplitude must be proportional to δ^{ab} , because it is the only available rank-two tensor. Since it is symmetric, the Lorentz structure must also be symmetric in order to satisfy *Bose symmetry*. The only building blocks we have available are $g^{\mu\nu}$, $(p_1^\mu p_2^\nu + p_2^\mu p_1^\nu)$, $p_1^\mu p_1^\nu$, and $p_2^\mu p_2^\nu$, but since all transverse parts drop out of the physical amplitude, the relevant tensors are only $g^{\mu\nu}$ and $p_2^\mu p_1^\nu$. Lastly, we know that the amplitude must satisfy the *Ward identity*, which allows us to restrict the tensor even further, such that we end up with

$$i\mathcal{M}^{\mu\nu,ab} = i\frac{\alpha_s}{\pi} \frac{1}{v} \delta^{ab} (p_2^\mu p_1^\nu - (p_1 \cdot p_2)g^{\mu\nu}) \mathcal{C}(m_H, m_q). \quad (4.5)$$

Notice that we have only made use of very general properties of the amplitude. This is why the decomposition in Eq. (4.5) will hold at every order of α_s . The function $\mathcal{C}(m_H, m_q)$ is called the *Higgs-gluon form factor*. It has mass dimension 0, i.e. its functional dependence on m_q and m_H must be through a mass ratio

$$\mathcal{C}(m_H, m_q) = \mathcal{C}(z), \quad \text{with} \quad z \equiv \frac{m_H^2}{4m_q^2}. \quad (4.6)$$

The factor of 1/4 was introduced, so that the *normal threshold* is located at $z = 1$. Mathematically, this means that $z = 1$ is a solution of the *Landau equations*. Physically, we can interpret the singularity as the point where we have enough energy to produce the quark pair on-shell. We can now project onto the form factor with

$$\mathcal{C}(z) = \frac{\pi v}{i\alpha_s} \frac{1}{N_c^2 - 1} \delta^{ab} \frac{1}{(p_1 \cdot p_2)^2 (d-2)} (p_{2\mu} p_{1\nu} - (p_1 \cdot p_2)g_{\mu\nu}) i\mathcal{M}^{\mu\nu,ab}. \quad (4.7)$$

Let us define the perturbative expansion of the Higgs-gluon form factor as

$$\mathcal{C} = \mathcal{C}^{(0)} + \frac{\alpha_s}{\pi} \mathcal{C}^{(1)} + \left(\frac{\alpha_s}{\pi}\right)^2 \mathcal{C}^{(2)} + \dots \quad (4.8)$$

If we now insert the LO expression of Eq. (4.4) and perform some basic manipulations we find for the leading coefficient

$$\mathcal{C}^{(0)}(z) = T_F \frac{1}{2 - 2\epsilon} \frac{1}{z} \int \frac{d^d k}{i\pi^{d/2}} \frac{1}{[k^2 - m_q^2 + i0^+][(k + p_1 + p_2)^2 - m_q^2 + i0^+]} \times \left(2\epsilon + \frac{m_H^2}{[(k + p_1)^2 - m_q^2 + i0^+]} \left(\frac{1}{z} + \epsilon - 1 \right) \right), \quad (4.9)$$

which, after inserting integrals and expanding in ϵ , finally reduces to

$$\mathcal{C}^{(0)}(z) = T_F \frac{1}{z} \left\{ 1 - \left(1 - \frac{1}{z} \right) \left[\frac{1}{2} \ln \left(\frac{\sqrt{1 - 1/z} - 1}{\sqrt{1 - 1/z} + 1} \right) \right]^2 \right\}. \quad (4.10)$$

We see that the Higgs-gluon form factor is roughly proportional to the square of the mass of the quark running in the loop. One power of m_q is hereby picked up from the Yukawa coupling. The other factor m_q is a consequence of the scalar coupling to Higgs. Indeed, without the quark mass, the trace in Eq. (4.4) would contain an odd number of gamma matrices and vanish consequently. Physically, we can interpret this as a helicity flip of the internal quark at the Higgs interaction vertex. And since massless QCD conserves helicity, the other helicity flip is provided by the mass. Similarly, since the two incoming gluons are vector bosons which should form a spinless final state, we would expect them to always carry opposite spins. This intuition is indeed confirmed by the tensor structure of the amplitude (4.5), as it always vanishes once contracted with two polarization vectors of the same helicity².

The LO Higgs-gluon form factor is plotted in Fig. 4.3. As expected, we pick up an imaginary part starting from the normal threshold at $z = 1$. If we expand the form factor around large quark masses, i.e. we perform a *large mass expansion* (LME), we find that it approaches a constant

$$\mathcal{C}^{(0)}(z) = T_F \left(\frac{2}{3} + \frac{7}{45}z + \frac{4}{63}z^2 + \mathcal{O}(z^3) \right). \quad (4.11)$$

We will discuss the infinite mass limit in more detail in section 4.2. On the other side of the spectrum we can see that if the mass of the Higgs is far greater than the mass the internal quark, the form factor is approximately

$$\mathcal{C}^{(0)}(z) = \frac{T_F}{4z} \left[4 - \log^2(-4z) + \frac{1}{z} (\log(-4z) + \log^2(-4z)) + \mathcal{O}(1/z^2) \right]. \quad (4.12)$$

This expansion is known as *high-energy limit* HEL. The appearing double logarithms $\log^2(m_q^2/m_H^2)$ originate from a soft quark exchange. In fact, the quark mass acts as an infrared regulator of the integral in Eq. 4.9, so the appearance of these logarithms is not entirely unexpected. Numerically, these logarithms can be very large. The bottom quark, for example will yield a double logarithm of about 46. I.e., although suppressed by a factor of m_q^2/m_H^2 , the contributions from lighter quark flavors are logarithmically enhanced and hence highly significant for precision predictions.

If we now apply Eq. (2.25) and perform the phase space integration, which for a single particle is trivial because of the momentum conserving delta function, we get for the partonic cross section

$$\hat{\sigma}_{gg \rightarrow H}(\tau S) = \frac{\pi}{64v^2} m_H^2 \left(\frac{\alpha_s}{\pi} \right)^2 |\mathcal{C}(z)|^2 \delta(\tau S - m_H^2) \frac{1}{1 - \epsilon}. \quad (4.13)$$

2 This can be seen easily by boosting to the center of mass frame and using $\epsilon^\mu(-\mathbf{p}, \lambda) \propto \epsilon^\mu(\mathbf{p}, -\lambda)$.

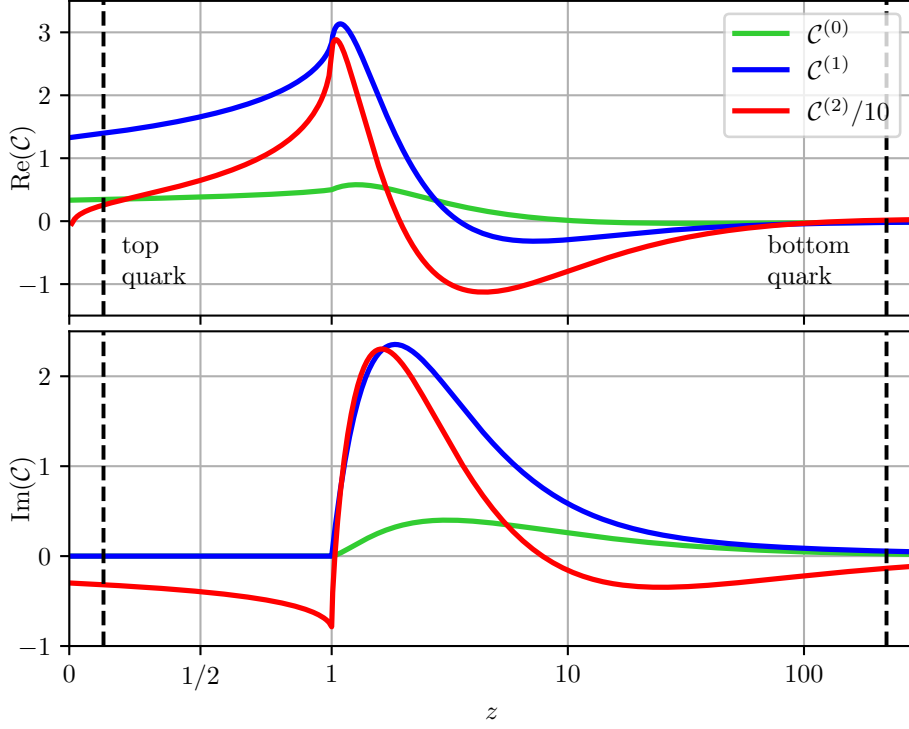


Figure 4.3: Real and imaginary part of the finite part of the Higgs-gluon form factor at various perturbative. NNLO is divided by ten for better visibility. NNLO results also depend on the number of light quark flavors, which has been set to 5 (5FS). Top-quark is renormalized in the OS scheme. Infrared divergences are subtracted in the $\overline{\text{MS}}$ scheme with the help of the \mathbf{Z} operator (see e.g. Ref. [42]). Vertical lines indicate the z values for the top- (on-shell) and bottom-quark ($\overline{\text{MS}}$) masses. The plot was created using the results of Ref. [43].

The initial state was averaged over spin and color. In conventional dimensional regularization, the gluons have $d - 2 = 2(1 - \epsilon)$ spin degrees. Finally, after the convolution with the partonic luminosity we arrive at the LO cross section

$$\sigma_{pp \rightarrow HX}^{\text{LO}}(S) = \frac{\pi}{64v^2} \left(\frac{\alpha_s}{\pi} \right)^2 \mathcal{L}_{gg} \left(\frac{m_H^2}{S} \right) |\mathcal{C}^{(0)}(z)|^2. \quad (4.14)$$

From Fig. 4.3 we can see that the top quark exerts the largest impact on the Higgs-gluon form factor and hence the LO hadron cross section. We can read off the partonic luminosity from Fig. 2.3 and find that the cross section for the top quark induces Higgs production reads³

$$\sigma_{pp \rightarrow HX}^{\text{LO}}(t) = 16.30 \text{ pb} \quad (4.15)$$

at a hadronic center of mass energy of 13 TeV. Although expected to have a less significant impact, we can also include the effects of finite bottom quark masses by coherently summing together the corresponding form factors. We find

$$\sigma_{pp \rightarrow HX}^{\text{LO}}(t + b) = 15.23 \text{ pb}, \quad (4.16)$$

i.e. the bottom quark lowers the cross section by around 6.5% at LO.

³ Values of masses and coupling constants are provided in the conventions.

Without the inclusion of electro-weak corrections, we can always decompose the gluon fusion cross section in terms of the Yukawa couplings Y_i :

$$\sigma_{pp \rightarrow HX} = \sum_{i \leq j} Y_i Y_j \sigma_{ij}. \quad (4.17)$$

We call

$$\sigma_{i \times j} = Y_i Y_j \sigma_{ij}, \quad (4.18)$$

the *i-j-interference contribution* and

$$\sigma_i = Y_i^2 \sigma_{ii} \quad (4.19)$$

the *pure-i contribution* to the cross section. Both contributions are depicted at LO in Fig. 4.4. Clearly, the dominant contribution for the lighter quark flavors comes from the interference with

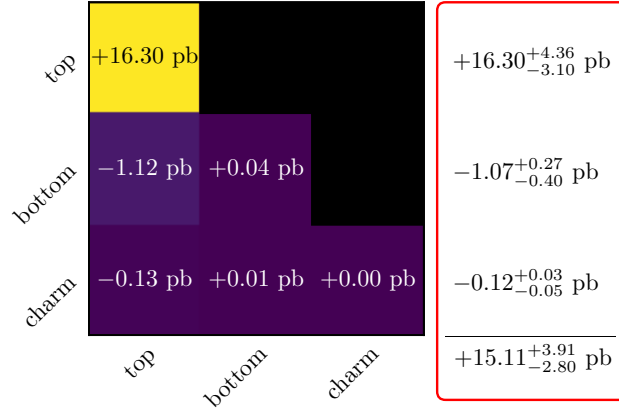


Figure 4.4: σ_i (diagonals) and $\sigma_{i \times j}$ (off-diagonals) at LO for the three heaviest quark flavors. The red box indicates the sum of each row, and hence the combined effects of each additional flavor. The computational setup is described in the conventions. We use the on-shell mass value for the top quark and $\overline{\text{MS}}$ masses for the bottom- and charm-quark. Scale uncertainties are computed with 7-point-variation.

the top-quark. The pure-bottom contribution is already below a percent and the pure-charm quark mass effects are completely negligible. The inclusion of the charm quark lowers the total cross section by around 1%.

4.2 THE HEAVY-TOP LIMIT

The computation of the Higgs production cross section in full QCD is quite challenging. As we saw above, even at leading order we encounter loop integrals with two mass scales. It is therefore maybe not surprising that the first NLO corrections to this process were actually computed in an approximation framework [44]. In the approximation, we assume that the quark, which is coupling to the Higgs is infinitely heavy. That means we are only interested in the leading term of the LME.

The finite distance interaction of the gluon and the Higgs will therefore shrink down to a point like vertex, which we can describe with the effective Lagrangian

$$\mathcal{L}_{\text{HTL}}^{(0)} = \mathcal{L}_{\text{QCD}}^{(n_f-1)} - C_1 \frac{H}{v} \frac{1}{4} G_{\mu\nu}^a G^{a\mu\nu}. \quad (4.20)$$

We see that the coupling constant now has mass dimension -1 , so the theory will not be UV renormalizable. That means that we cannot absorb all UV divergences into multiplicative renormalization constants as we did for the SM (see Eq. (2.31)), but we will generate more and more independent terms in our Lagrangian to cancel all appearing divergences. On the other hand, as long as we restrict ourselves to QCD corrections, and hence only single operator insertions, we can treat the color singlet Higgs as a constant, and renormalize only the gauge invariant operator

$$\mathcal{O}_1 \equiv -1/4 G_{\mu\nu}^a G^{a\mu\nu}. \quad (4.21)$$

To indicate the perturbative order we gave the Lagrangian in Eq. (4.20) a superscript. The superscript $n_f - 1$ of the QCD Lagrangian specifies the number of active flavors. It was reduced by one, since the heaviest quark flavor was integrated out. The constant C_1 is called a *Wilson coefficient*, and it needs to be matched to the full theory in the infinite quark mass limit. At LO for example, we find that the Higgs-gluon form factor in the effective theory simply reads

$$C_1 = -\frac{\alpha_s}{\pi} \mathcal{C}^{(0)} + \mathcal{O}(\alpha_s^2). \quad (4.22)$$

If we compare this to the leading term of our LME (4.11), we find

$$C_1 = -\frac{\alpha_s}{\pi} \frac{2}{3} T_F + \mathcal{O}(\alpha_s^2). \quad (4.23)$$

The main benefit of the approximation lies in the reduced complexity. By integrating out the top quark, we have reduced a loop-induced process to a tree-level process. Moreover, the top-quark mass is eliminated as a scale, hence the appearing Feynman integrals will generally be much simpler to solve.

4.2.1 Renormalization of Gauge Invariant Operators

Beyond LO gauge invariant operator like \mathcal{O}_1 can mix under renormalization with other gauge invariant operators but notably also with operators which are not gauge invariant. In general, we distinguish two types of operators: *Type-II operators*, which give zero when sandwiched between physical states, and *type-I operators*, which can give non-zero matrix elements. The type-II operators can be further subcategorized into operators vanishing by the equation of motion (*type-II_a operators*), and all other operators (*type-II_b operators*). For a polynomial operator with ghost number zero satisfying

$$s\mathcal{O} = 0, \quad (4.24)$$

where s is the *linearized Slavnov operator*, one can proof [45, 46, 47] that

$$\mathcal{O} = sF + \text{gauge invariant operators}. \quad (4.25)$$

Operators of the form sF are also called *Bechi-Rouet-Stora-Tyutin-* (BRST-) *exact operators*, and they vanish between physical states. For \mathcal{O}_1 the above conditions are met, allowing us to

conclude that the \mathcal{O}_{II} operators are BRST-exact. This can be leveraged to find the complete operator basis:

$$\begin{aligned} \mathcal{O}_I & \begin{cases} \mathcal{O}_1 = -\frac{1}{4}G_{\mu\nu}^a G^{a\mu\nu}, \\ \mathcal{O}_2 = \sum_{i=1}^{n_l} m_i \bar{q}_i q_i, \end{cases} \\ \mathcal{O}_{II_a} & \begin{cases} \mathcal{O}_3 = \sum_{i=1}^{n_l} \bar{q}_i \left(\frac{i}{2} \overleftrightarrow{D} - m \right) q_i, \end{cases} \\ \mathcal{O}_{II_b} & \begin{cases} \mathcal{O}_4 = A^{a\mu} D^\nu G_{\nu\mu}^a + g \sum_{i=1}^{n_l} \bar{q}_i \not{A} q_i - \partial^\mu \bar{c}^a \partial_\mu c^a, \\ \mathcal{O}_5 = D_\mu \partial^\mu \bar{c}^a c^a. \end{cases} \end{aligned} \quad (4.26)$$

The operator basis is constructed only of light fields, and the light fields are defined in a decoupled theory.

Since operators of type II cannot generate non-vanishing S -matrix elements through renormalization the renormalization matrix must have the general structure

$$\begin{pmatrix} \mathcal{O}_I^R \\ \mathcal{O}_{II}^R \end{pmatrix} = \begin{pmatrix} z^{I,I} & z^{I,II} \\ 0 & z^{II,II} \end{pmatrix} \begin{pmatrix} \mathcal{O}_I^B \\ \mathcal{O}_{II}^B \end{pmatrix}. \quad (4.27)$$

The final form of our effective Lagrangian therefore reads

$$\mathcal{L}_{\text{HTL}} = \mathcal{L}_{\text{QCD}}^{(5)} + \frac{H}{v} \sum_{i=1}^5 C_i^B \mathcal{O}_i^B. \quad (4.28)$$

As usual, we replace the bare quantities by their renormalized counter parts

$$C_i^B \mathcal{O}_i^B = C_i^B Z_{ij}^{-1} \mathcal{O}_j^R, \quad (4.29)$$

and we identify

$$C^R = (Z^{-1})^T C^B. \quad (4.30)$$

Using the RGE we find that the *anomalous dimension* matrix of the Wilson coefficients is determined through

$$\frac{dC^R}{d \ln \mu} = \left(Z \frac{d(Z^{-1})}{d \ln \mu} \right)^T C^R = - \left(\frac{dZ}{d \ln \mu} Z^{-1} \right)^T \equiv \gamma^T C^R. \quad (4.31)$$

With the structure of the renormalization matrix (4.27), we arrive at an important conclusion: The Wilson coefficients of type-II operators cannot mix into the Wilson coefficients of type-I operators through the running in the scale. Since the type-II operators render no contribution to the scattering matrix element, we can focus our attention on the gauge invariant operators and their Wilson coefficients.

We now want to determine the I, I part of the renormalization matrix, i.e. $z^{I,I}$ to determine the running of the Wilson coefficients. Let us start by defining the generating functional

$$\begin{aligned} Z[J] &\equiv z[J]/z[0], \quad z[J] \equiv \int \prod_i \mathcal{D}\Phi_j e^{i(S+J\cdot\Phi)}, \quad S = S[A, c, \bar{c}, q, \bar{q}] \equiv \int d^d x \mathcal{L}, \\ J &= (J^\mu, \bar{J}, J, \bar{\eta}, \eta), \quad \Phi = \left(\frac{1}{g} A_\mu, c, \bar{c}, q, \bar{q} \right), \end{aligned} \quad (4.32)$$

with the Lagrangian

$$\mathcal{L} \equiv -\frac{1}{4g^2} F_{\mu\nu}^a F^{a\mu\nu} - \frac{1}{2\xi g^2} (\partial \cdot A)^2 + \partial^\mu \bar{c}^a D_\mu c^a + \bar{q} \left(\frac{i \overleftrightarrow{D}}{2} - m_q \right) q. \quad (4.33)$$

The Lagrangian is the QCD Lagrangian with only one active quark flavor and rescaled gauge fields

$$A_\mu^a \longrightarrow \frac{1}{g} A_\mu^a. \quad (4.34)$$

The operators in Eq. (4.26) can now be generated by applying the differential operators⁴

$$\begin{aligned} D_1 &= -\frac{1}{2}g \frac{\partial}{\partial g} + \xi \frac{\partial}{\partial \xi} - \frac{1}{2}J_\mu \cdot \frac{\delta}{\delta J_\mu}, \\ D_2 &= -m_q \frac{\partial}{\partial m_q}, \end{aligned} \quad (4.35)$$

on the generating functional

$$z_{\mathcal{O}_k}[J] \equiv \int \prod_j \mathcal{D}\Phi_j \hat{\mathcal{O}}_k(0) e^{i(S+J \cdot \Phi)} = -iD_k z[J]. \quad (4.36)$$

Here $\hat{\mathcal{O}}_k(0)$ is the Fourier transform of the operator $\mathcal{O}(x)$ at zero momentum. The normalization of the generating functional then properly subtracts the vacuum expectation value of the operators

$$-iD_k Z[J] = \frac{1}{z[0]} \int \prod_j \mathcal{D}\Phi_j \left(\hat{\mathcal{O}}_k(0) - \langle \Omega | \mathcal{O}_k(0) | \Omega \rangle \right) e^{i(S+J \cdot \Phi)} \equiv Z_{\mathcal{O}_k}. \quad (4.37)$$

In the $\overline{\text{MS}}$ scheme, the R -operation commutes with the differential operators in Eq. (4.35), i.e. the renormalized operators can be generated from the renormalized generating functional

$$Z_{\mathcal{O}_k^R} = -iD_k Z^R[J], \quad (4.38)$$

where the renormalized generating functional is defined as

$$\begin{aligned} Z^R[J] &= z^R[J]/z^R[0], \\ z^R[J] &= \int \prod_i \mathcal{D}\Phi_i e^{i(S^R+J \cdot \Phi)}, \\ S^R &\equiv S[Z_3'^{1/2} A^R, Z_3'^{-1/2} c^R, \tilde{Z}_3'^{-1/2} \bar{c}^R, Z_2'^{1/2} q^R, Z_2'^{1/2} \bar{q}^R, Z_g g, Z_m m_q, Z_g^{-2} Z_3' \xi^R]. \end{aligned} \quad (4.39)$$

Using the chain rule we find that

$$-iD_k z^R[J] = \int \prod_j \mathcal{D}\Phi_j \left[\hat{\mathcal{O}}_k(0) + \sum_i (D_k \ln Z_i) \frac{\partial S^R}{\partial \ln Z_i} \right] e^{iS^R+J \cdot \Phi}, \quad Z_i \in \{Z_3', \tilde{Z}_3', Z_2, Z_g, Z_m\}. \quad (4.40)$$

And with

$$Z_g \frac{\partial S^R}{\partial Z_g} = -2\hat{\mathcal{O}}_1(0), \quad \text{and} \quad Z_m \frac{\partial S^R}{\partial Z_m} = -\hat{\mathcal{O}}_2(0), \quad (4.41)$$

⁴ We only provide the operators for the type-I operators, since they are the only ones necessary for computing physical amplitudes.

we find that the renormalization constants are given by

$$\begin{aligned} z_{11}^{I,I} &= 1 - 2D_1 \ln Z_g = 1 + g \frac{\partial \ln Z_g}{\partial g}, & z_{12}^{I,I} &= -D_1 \ln Z_m = \frac{g}{2} \frac{\partial \ln Z_m}{\partial g} \\ z_{21}^{I,I} &= 0, & z_{22}^{I,I} &= 1. \end{aligned} \quad (4.42)$$

Here we made use of the fact, that the $\overline{\text{MS}}$ -renormalization constants are independent of the quark mass and the gauge parameter. We can rewrite the appearing derivatives in terms of the β -function and the mass-anomalous dimension. Indeed,

$$\begin{aligned} \frac{4\pi}{\alpha_s} \bar{\beta} &\equiv \frac{d \ln \alpha_s}{d \ln \mu} = -\frac{d \ln Z_{\alpha_s}}{d \ln \mu} = -\left(\frac{\partial \ln Z_{\alpha_s}}{\partial \ln \alpha_s} \frac{d \ln \alpha_s}{d \ln \mu} + \frac{\partial \ln Z_{\alpha_s}}{\partial \ln \mu} \right) = -\left(\frac{4\pi}{\alpha_s} \bar{\beta} \frac{\partial \ln Z_{\alpha_s}}{\partial \ln \alpha_s} + 2\epsilon \right) \\ &\Rightarrow \frac{\partial \ln Z_{\alpha_s}}{\partial \ln \alpha_s} = g \frac{\partial \ln Z_g}{\partial g} = -1 - 2\epsilon \frac{\alpha_s}{4\pi \bar{\beta}} = -1 + \frac{1}{1 - \frac{\beta}{2\epsilon} \frac{4\pi}{\alpha_s}}, \end{aligned} \quad (4.43)$$

where in the last step we used the relation between the d - and four-dimensional β -functions

$$\bar{\beta} = \beta - 2\epsilon \frac{\alpha_s}{4\pi}. \quad (4.44)$$

Similarly, we find

$$\begin{aligned} \gamma_m &\equiv -\frac{d \ln m_q}{d \ln \mu} = \frac{d \ln Z_m}{d \ln \mu} = \frac{\partial \ln Z_m}{\partial \ln \alpha_s} \frac{\partial \ln \alpha_s}{\partial \ln \mu} = \frac{\partial \ln Z_m}{\partial \ln \alpha_s} \frac{4\pi}{\alpha_s} \bar{\beta} \\ &\Rightarrow \frac{\partial \ln Z_m}{\partial \ln \alpha_s} = g \frac{\partial \ln Z_m}{\partial g} = \frac{\alpha_s}{4\pi} \frac{1}{\bar{\beta}} \gamma_m = -\frac{\gamma_m}{2\epsilon} \frac{1}{1 - \frac{\beta}{2\epsilon} \frac{4\pi}{\alpha_s}} \end{aligned} \quad (4.45)$$

Finally, we want to use the above results to calculate the anomalous dimension matrix in Eq. (4.31). The entries of the renormalization constant only depend on scale through the coupling constant, i.e.

$$\gamma^{I,I} = -\frac{dz^{I,I}}{d \ln \mu} (z^{I,I})^{-1} \Big|_{\epsilon=0} = -\frac{\partial z^{I,I}}{\partial \alpha_s} (z^{I,I})^{-1} 4\pi \bar{\beta} \Big|_{\epsilon=0} = \frac{\partial z^{I,I(1)}}{\partial \alpha_s} 2\alpha_s. \quad (4.46)$$

Where we used that $z^{I,I}$ consists only of poles in the $\overline{\text{MS}}$ scheme, and once again applied the relation between the β -functions in Eq. (4.44). $z^{I,I(1)}$ denotes the residue of the renormalization matrix

$$z^{I,I} = \mathbb{1} + \sum_{i=1} z^{I,I(i)} \epsilon^{-i}. \quad (4.47)$$

We then find for the anomalous dimension matrix

$$\gamma^{I,I} = \begin{pmatrix} 4\pi \alpha_s \frac{d}{d \alpha_s} \left(\frac{\beta}{\alpha_s} \right) & -\alpha_s \frac{d \gamma_m}{d \alpha_s} \\ 0 & 0 \end{pmatrix}. \quad (4.48)$$

The structure of this matrix reveals, that the C_1 Wilson coefficient, which is relevant coefficient for the HTL, is completely independent of the other Wilson coefficients. The RGE for the Wilson coefficient (4.31) can now be written as

$$\frac{\partial C_1}{\partial \alpha_s} 4\pi \beta + \frac{\partial C_1}{\partial \ln \mu} = 4\pi \alpha_s \frac{d}{d \alpha_s} \left(\frac{\beta}{\alpha_s} \right) C_1. \quad (4.49)$$

The β -function has the general expansion

$$\beta = \left(\frac{\alpha_s}{4\pi}\right)^2 \sum_{i=0} \beta_i \left(\frac{\alpha_s}{4\pi}\right)^i. \quad (4.50)$$

For example at one-, and two-loop, it can be shown [48, 49, 50, 51, 52, 53]

$$\begin{aligned} \beta_0 &= -\frac{11}{3}C_A + \frac{4}{3}T_F n_f, \\ \beta_1 &= -\frac{34}{3}C_A^2 + \frac{20}{3}C_A T_F n_f + 4C_F T_F n_f. \end{aligned} \quad (4.51)$$

We can solve the partial differential equation in Eq. (4.49) perturbatively by proposing the Ansatz

$$\begin{aligned} C_1 &= \frac{\alpha_s}{4\pi} C_1^{(0,0)} + \left(\frac{\alpha_s}{4\pi}\right)^2 \left(C_1^{(1,0)} + C_1^{(1,1)} \ln \frac{\mu}{\mu_0} \right) \\ &+ \left(\frac{\alpha_s}{4\pi}\right)^3 \left(C_1^{(2,0)} + C_1^{(2,1)} \ln \frac{\mu}{\mu_0} + C_1^{(2,2)} \ln^2 \frac{\mu}{\mu_0} \right) + \dots. \end{aligned} \quad (4.52)$$

The constants coefficients $C_1^{(i,0)}$ mark the initial conditions; they need to be matched to the full theory in the infinite mass limit. The coefficients of the logarithms on the other hand can be determined through a comparison of coefficients, they read

$$\begin{aligned} C_1^{(1,1)} &= 0, \\ C_1^{(2,1)} &= C_1^{(0,0)} \beta_1 - C_1^{(1,0)} \beta_0, \quad C_1^{(2,2)} = 0, \\ C_1^{(3,1)} &= 2C_1^{(0,0)} \beta_2 - 2C_1^{(2,0)} \beta_0, \quad C_1^{(3,2)} = \beta_0^2 C_1^{(1,0)} - \beta_0 \beta_1 C_1^{(0,0)}, \quad C_1^{(3,3)} = 0. \end{aligned} \quad (4.53)$$

It is clear from the structure of the differential equation, that the all coefficients $C_1^{(i,i)}$ are in fact all zero except for $C_1^{(0,0)}$.

4.2.2 Matching of Wilson Coefficients

By expanding the Higgs-gluon form for large quark masses we were able to determine the LO Wilson coefficient. Of course, if we would need the full Higgs-gluon form factor to determine the Wilson coefficient, the HTL would be of little use, since it would not bring any simplifications. Fortunately, the large quark mass limit can already be used at the integrand level using the large mass expansion.

Alternatively, one may find the matching coefficients by means of *low-energy theorems* [54, 55, 56]:

$$-iG_{\mathcal{O}_1, \dots, \mathcal{O}_n, \bar{q}_i q_i}^B(p_1, \dots, p_{n-1}, 0) \Big|_{\text{connected}} = \frac{\partial}{\partial m_i^B} G_{\mathcal{O}_1, \dots, \mathcal{O}_n}^B(p_1, \dots, p_{n-1}) \Big|_{\text{connected}}. \quad (4.54)$$

Here, $\mathcal{O}_1, \dots, \mathcal{O}_n$ are local operators and $G_{\mathcal{O}_1, \dots}^B|_{\text{connected}}$ denotes the momentum space representation of the corresponding connected Green's functions

$$\begin{aligned} &\int \left(\prod_{i=1}^n d^d x_i e^{ip_i \cdot x_i} \right) \langle \Omega | T [\mathcal{O}_1^B(x_1) \dots \mathcal{O}_n^B(x_n)] | \Omega \rangle \Big|_{\text{connected}} \\ &\equiv (2\pi)^d \delta^{(d)} \left(\sum_{i=1}^n p_i \right) G_{\mathcal{O}_1, \dots, \mathcal{O}_n}^B(p_1, \dots, p_{n-1}) \Big|_{\text{connected}}, \end{aligned} \quad (4.55)$$

$|\Omega\rangle$ denotes the vacuum of the interacting theory and T is the *time ordering operator*. The theorem relates the mass derivative of a Green's function with a Green's function of the same operators but with the insertion of $\bar{q}_i q_i$ at zero momentum.

It follows upon application of the *Gell-Mann–Low formula*

$$\begin{aligned} \frac{\partial}{\partial m_i^B} \langle \Omega | T [\mathcal{O}_1^B(x_1) \dots \mathcal{O}_n^B(x_n)] | \Omega \rangle \Big|_{\text{connected}} = \\ \langle 0 | T \left[\mathcal{O}_{1,I}^B(x_1) \dots \mathcal{O}_{n,I}^B(x_n) (-i) \int d^d x \left(1 + \frac{H_I^B(x)}{v} \right) \bar{q}_i^B(x) q_i^B(x) \exp \left(-i \int d^d z \mathcal{H}_{\text{int},I}^B(z) \right) \right] | 0 \rangle \end{aligned} \quad (4.56)$$

The subscript I indicates interaction picture fields, $|0\rangle$ is the vacuum state, now of the free theory, and \mathcal{H}_{int} is the interaction part of the *Hamiltonian*. Without the inclusion of electroweak corrections, we can omit the field of the Higgs⁵ in the intergral. This also implies, that all operators $\mathcal{O}_1, \dots, \mathcal{O}_n$, do not contain any electroweak fields. After switching to momentum space, we immediately arrive at Eq. (4.54).

Since the proof relied on relations on the level of the Lagrangian, the statement is only true for bare amplitudes and Green's functions beyond LO. It can be straightforwardly generalized to include an arbitrary number of massive particles, by simply summing over all massive particles. Lastly, we note that the differential operator does not act on masses in the operators themselves, should they contain any.

We can now apply the low-energy theorem on the gluon self energy. Let us consider first the *amputated* Green's function of two gluons with the insertion of the composite operator $\mathcal{O}_h = \bar{h}^B h^B$. In momentum space, it reads

$$\begin{aligned} G_{A,A,\mathcal{O}_h}^{B,ab\mu\nu}(p,0) \Big|_{\text{amp.}} &= \int d^d x d^d y e^{ip \cdot (x-y)} \langle \Omega | T [A^{B,a\mu}(x) A^{B,b\nu}(y) \mathcal{O}_h(0)] | \Omega \rangle \Big|_{\text{amp.}} \\ &\equiv \delta^{ab} \left[-g^{\mu\nu} p^2 G_{A,A,\mathcal{O}_h}^B(p^2) \Big|_{\text{amp.}} + \text{terms proportional to } p^\mu p^\nu \right], \end{aligned} \quad (4.57)$$

where T denotes the time ordering operator and p is the momentum along the gluon line. As discussed in detail above, in the limit of infinite quark mass $m_h^B \rightarrow \infty$, the operator $\bar{h}h$ can be written in terms of a linear combination of the operators $\mathcal{O}_1, \dots, \mathcal{O}_5$

$$\begin{aligned} G_{A,A,\mathcal{O}_h}^{B,ab\mu\nu}(p,0) \Big|_{\text{amp.}} &\simeq \\ &- \int d^d x d^d y e^{ip \cdot (x-y)} \langle \Omega | T \left[A^{B,a\mu}(x) A^{B,b\nu}(y) \frac{\alpha_s}{\pi} \frac{1}{m_h^B} \sum_{i=1}^5 C_i^B \mathcal{O}_i^B(0) \right] | \Omega \rangle \Big|_{\text{amp.}}. \end{aligned} \quad (4.58)$$

The \simeq indicates, that the relation holds only up to power corrections of order $1/m_h^{B^2}$.

In the $\overline{\text{MS}}$ scheme, the *Appelquist–Carazzone decoupling theorem* [57] does not hold in its naïve sense, i.e. heavy degrees of freedom, do not decouple at low energy. The standard method to circumvent this issue, is by the introduction decoupling constants, which relate quantities at in the decoupled theory (denoted with a superscript (n_l)) with the full high energy theory:

$$\begin{aligned} g^{B,(n_l)} &= \zeta_g^B g^B, \quad m_i^{B,(n_l)} = \zeta_{m_i}^B m_i^B, \quad \xi^{B,(n_l)} - 1 = \zeta_3^B (\zeta^B - 1), \\ q_i^{B,(n_l)} &= \sqrt{\zeta_2^B} q_i^B, \quad A_\mu^{B,(n_l),a} = \sqrt{\zeta_3^B} A_\mu^{B,a}, \quad c^{B,(n_l),a} = \sqrt{\tilde{\zeta}_3^B} c^{B,a}. \end{aligned} \quad (4.59)$$

⁵ Not to be confused with the Higgs field.

The relations hold up to power corrections of $1/m_h^2$. The decoupling constants are functions of g^B, m_i^B and the scale μ , but the function arguments are left implicit. The amputated Green's functions then becomes⁶

$$G_{A,A,\mathcal{O}_h}^{B,ab\mu\nu}(p,0)\Big|_{\text{amp.}} \simeq -\zeta_3^B \int d^d x d^d y e^{ip\cdot(x-y)} \langle \Omega | T \left[A^{B,(n_l),a\mu}(x) A^{B,(n_l),b\nu}(y) \frac{\alpha_s}{\pi} \frac{1}{m_h^B} \sum_{i=1}^5 C_i^B \mathcal{O}_i^B(0) \right] | \Omega \rangle \Big|_{\text{amp.}} \quad (4.60)$$

At LO in α_s , we will have only contributions from the operators \mathcal{O}_1 and \mathcal{O}_4 , because all other operators would create disconnected contributions

$$G_{A,A,\mathcal{O}_h}^{B,ab\mu\nu}(p,0)\Big|_{\text{amp.}} \simeq -\frac{\alpha_s}{\pi} \frac{1}{m_h^B} \delta^{ab} (-g^{\mu\nu} p^2 \zeta_3^B (C_1^B + 2C_4^B) + \mathcal{O}(\alpha_s)) + \text{terms proportional to } p^\mu p^\nu. \quad (4.61)$$

We now set the mass of the light quarks in the QCD Lagrangian to zero; the light quark masses in the definition of the operators in Eq. (4.26) can still be non-vanishing. In the limit of vanishing gluon momentum $p \rightarrow 0$, the coefficient of the transverse part does not receive any α_s -corrections in DR, because all appearing Feynman integrals are necessarily scaleless. We have thus shown the all order result

$$G_{A,A,\mathcal{O}_h}^B(0,0)\Big|_{\text{amp.}} \simeq -\frac{\alpha_s}{\pi} \frac{1}{m_h^B} \zeta_3^B (C_1^B + 2C_4^B). \quad (4.62)$$

By application of the LSZ reduction formula we can rewrite the amputated Green's functions in terms of connected ones. The operator \mathcal{O}_h is hereby irrelevant as it is not considered to be external, i.e. (4.54) holds for regular, connected and 1-particle-irreducible Green's functions. Application of Eq. (4.54) yields

$$\frac{\alpha_s}{\pi} (C_1^B + 2C_4^B) = \frac{\partial \ln \zeta_3^B}{\partial \ln m_h^B}. \quad (4.63)$$

We can repeat the same analysis for $G_{\bar{c},c,\mathcal{O}_h}(p,0)$ and $G_{\bar{c},c,g,\mathcal{O}_h}(p,p,0)$ and in the limit $p \rightarrow 0$ obtain

$$\begin{aligned} \frac{\alpha_s}{\pi} (-C_4^B - C_5^B) &= \frac{\partial \ln \tilde{\zeta}_3^B}{\partial \ln m_h^B} \\ \frac{\alpha_s}{\pi} (-C_5^B) &= \frac{\partial}{\partial \ln m_h^B} \ln \left(\tilde{\zeta}_3^B \sqrt{\zeta_3^B} \zeta_g^B \right) \end{aligned} \quad (4.64)$$

Eq. (4.63) and (4.64) form a linear system of equations which we can solve for the Wilson coefficients. The solution for the physical Wilson coefficient reads

$$\frac{\alpha_s}{\pi} C_1^B = -\frac{\partial \ln \zeta_g^{B^2}}{\partial \ln m_h^B}. \quad (4.65)$$

In the $\overline{\text{MS}}$ scheme, the renormalization constant of the heavy quark mass is independent of the mass, i.e.

$$\frac{\partial}{\partial \ln m_h^B} = \frac{\partial}{\partial \ln m_h}. \quad (4.66)$$

⁶ Keep in mind, that the amputated Green's function is an antilinear functional of the fields.

With the renormalization matrix in Eq. (4.42) we can then find the renormalized version of Eq. (4.65)

$$\frac{\alpha_s}{\pi} C_1 = -\frac{\partial \ln \zeta_g^2}{\partial \ln m_h}. \quad (4.67)$$

The decoupling constants are known at two-, three-[58] and four-loop [59, 60] order. Notice that we only require the logarithmic dependence of the decoupling constants to obtain the Wilson coefficients. The logarithmic structure on the other hand may be reconstructed from lower order terms in combination with the β -function and the mass anomalous dimension [56]. The four-loop decoupling constant is therefore sufficient, to match the Wilson coefficient up to N⁴LO. Here we only provide the Wilson coefficient up to N³LO, as it is the highest order for which full cross section calculations are available at present

$$\begin{aligned} C_1^{(0,0)} &= -\frac{4}{3} \\ C_1^{(1,0)} &= -\frac{44}{3} \\ C_1^{(2,0)} &= -\frac{5554}{27} + \frac{76}{3} \ln\left(\frac{m_h^2}{\mu^2}\right) + n_l \left[\frac{134}{9} + \frac{64}{9} \ln\left(\frac{m_h^2}{\mu^2}\right) \right] \\ C_1^{(3,0)} &= \frac{2892659}{486} - \frac{897943}{108} \zeta(3) + \frac{13864}{27} \ln\left(\frac{m_h^2}{\mu^2}\right) - \frac{836}{3} \ln^2\left(\frac{m_h^2}{\mu^2}\right) - \frac{64}{81} \ln^3\left(\frac{m_h^2}{\mu^2}\right) \\ &\quad + n_l \left[-\frac{40291}{243} + \frac{110779}{162} \zeta(3) + \frac{7040}{81} \ln\left(\frac{m_h^2}{\mu^2}\right) - \frac{184}{3} \ln^2\left(\frac{m_h^2}{\mu^2}\right) \right] \\ &\quad + n_l^2 \left[\frac{13730}{729} + \frac{308}{81} \ln\left(\frac{m_h^2}{\mu^2}\right) + \frac{128}{27} \ln^2\left(\frac{m_h^2}{\mu^2}\right) \right]. \end{aligned} \quad (4.68)$$

Notice that the decoupling constant ζ_g is a function of $\alpha_s^{(n_l+1)}$, i.e. we must recursively apply the decoupling relations (4.59) to express everything in terms of decoupled quantities. The heavy mass m_h is the $\overline{\text{MS}}$ mass.

4.2.3 Higher-Order Corrections

With the effective theory matched, we are ready to discuss higher order corrections to the Higgs production cross section. In the HTL the cross section was computed up to N³LO in the literature [44, 61, 17, 62]. Here, we will briefly recapitulate the NLO calculation, as it nicely illustrates the methods introduced in section 2.2.

We start with the computation of the hard scattering amplitudes. At NLO we require the one-loop Higgs-gluon form factor, and the tree-level amplitudes for $q\bar{q} \rightarrow Hg$, $qg \rightarrow Hq$, and $gg \rightarrow Hg$.

The careful reader might wonder why we do not have to compute the $q\bar{q} \rightarrow H$ amplitude. The reason is, that these amplitudes will be zero to all orders. Indeed, the corresponding amplitude would be of the form

$$\mathcal{M}_{q\bar{q} \rightarrow H} = i \frac{\alpha_s}{\pi} \bar{v}(p_2) [\dots] u(p_1) \delta_{c_1 c_2} \frac{1}{v} C_{q\bar{q}H}, \quad (4.69)$$

where the dots indicate an a priori unknown number of γ -matrices. But since there is no external vector field, the γ -matrices must be fully contracted. The only available objects to contract a γ -matrix with, are either another γ -matrix, or the momenta p_1 or p_2 . Contractions among the

γ -matrices can always be reduced by applying the anti-commutation relations provided by the Clifford algebra of the γ -matrices. Afterwards, we are left only with contractions with p_1 or p_2 . These on the other hand vanish in Eq. (4.69) because of the equation of motion.

The virtual contributions to the cross sections are obtained by evaluating the Feynman diagrams in Fig. 4.5. The result is the NLO correction to the Higgs-gluon form factor in the HTL and reads

$$\mathcal{C}(0) = \frac{1}{3} \left\{ 1 + \frac{\alpha_s}{\pi} \left(-\frac{m_H^2 + 0^+}{\mu^2} \right)^{-\epsilon} \left(-\frac{3}{2} \frac{1}{\epsilon^2} + \frac{11}{4} + \frac{\pi^2}{8} \right) \right\} \quad (4.70)$$

Using Eq. (4.13) for the partonic $gg \rightarrow H$ cross section, we then find

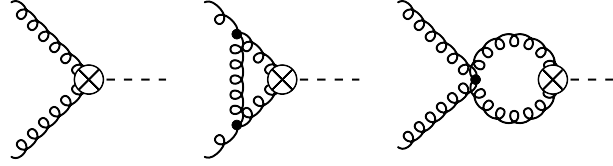


Figure 4.5: One-loop corrections to the Higgs-gluon form factor. The first diagram contributes through the NLO Wilson coefficient.

$$\begin{aligned} \hat{\sigma}_{gg \rightarrow H} &= \frac{\pi}{576v^2} \xi \left(\frac{\alpha_s}{\pi} \right)^2 \delta(1 - \xi) \\ &\times \left[(1 + \epsilon + \mathcal{O}(\epsilon^2)) + \frac{\alpha_s}{\pi} \left(\frac{m_H^2}{\mu^2} \right)^{-\epsilon} \left(-\frac{3}{\epsilon^2} - \frac{3}{\epsilon} + \frac{5}{2} + \frac{7\pi^2}{4} + \mathcal{O}(\epsilon) \right) + \mathcal{O}(\alpha_s^2) \right] \end{aligned} \quad (4.71)$$

where we defined ξ as the of the Higgs mass over the partonic center of mass energy

$$\xi = \frac{m_H^2}{s} = \frac{m_H^2}{\tau S}. \quad (4.72)$$

As expected, the NLO partonic cross section is not finite on its own, because the IR divergences only cancel in inclusive observables. We must therefore also compute the real radiation corrections as well as the contributions from collinear renormalization. For the former, we evaluate the diagrams in Fig. 4.6 and obtain the averaged squared amplitude

$$\overline{|\mathcal{M}_{gg \rightarrow Hg}|^2} = \frac{1}{N_A^2 4(1 - \epsilon)^2} \frac{\alpha_s^3}{v^2} \left(\frac{32}{3\pi} \right) \left[(1 - 2\epsilon) \frac{m_H^8 + s^4 + t^4 + u^4}{stu} + \frac{\epsilon}{2} \frac{(m_H^4 + s^2 + t^2 + u^2)^2}{stu} \right], \quad (4.73)$$

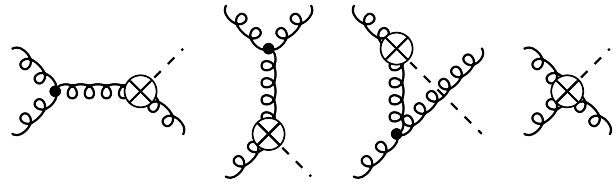


Figure 4.6: Feynman diagrams for the real radiation corrections in the gluon-gluon channel.

where N_A is the dimension of the adjoint representation, i.e. $N_A = N^2 - 1$ for $SU(N)$ groups. The symbols s , t and u denote the usual *Mandelstam variables*. Since the Mandelstam variables are not completely independent, as they must satisfy

$$s + t + u = m_H^2, \quad (4.74)$$

the squared matrix element only depends on the final state momenta through t or u . The phase-space integral is $2 * d$ dimensional. We can reduce one of the d dimensional integrals via the momentum conserving delta function. Using spherical coordinates and the remaining two delta functions which ensure on-shellness of the Higgs and the final state gluon, we can carry out the energy and momentum magnitude integral explicitly. This is particularly simple in the center of mass frame. We are hence left with an integral over the \mathcal{S}_1^{d-2} sphere. If we now apply the recursion relation

$$\int_{\mathcal{S}_1^{d-2}} = \int d\cos\theta \sin^{d-4}\theta \int_{\mathcal{S}_1^{d-3}}, \quad (4.75)$$

and use that the amplitude only depends on the azimuthal angle, i.e. the scattering angle of the Higgs (or gluon), we can carry out the integral over the \mathcal{S}_1^{d-3} sphere explicitly. In the end the phase-space integral is a single one-dimensional integral

$$\text{P.S.} = \frac{1}{8\pi} \frac{1}{\Gamma(1-\epsilon)} \left(\frac{s}{\mu^2 e^{\gamma_E}} \right)^{-\epsilon} (1-\xi)^{1-2\epsilon} \Theta(1-\xi) \int_0^1 d\omega \omega^{-\epsilon} (1-\omega)^{-\epsilon}, \quad (4.76)$$

where ω is related to the scattering angle of the Higgs via

$$\omega = \frac{1 + \cos\theta}{2}. \quad (4.77)$$

The amplitude in Eq. (4.73) is proportional to $1/tu$, i.e. it diverges if the final state gluon becomes collinear to one of the initial state gluons. Consequently, we expect the appearance of poles once we perform the phase-space integration. Indeed, we find after a straightforward integration

$$\begin{aligned} \hat{\sigma}_{gg \rightarrow Hg} &= \frac{1}{576\pi^2} \frac{\alpha_s}{v^2} (1-\xi)^{-1-2\epsilon} \left(\frac{s}{\mu^2} \right)^{-\epsilon} \Theta(1-\xi) \\ &\times \left[-\frac{3}{\epsilon} (1 + \xi^4 + (1-\xi)^4) - \frac{11}{2} (1-\xi)^4 - 6(1-\xi + \xi^2)^2 + \epsilon \left(\frac{3\pi^2}{2} - 6 + (1-\xi) \cdot (\dots) \right) \right]. \end{aligned} \quad (4.78)$$

The cross section also has a soft singularity at $\xi \rightarrow 1$, which can be regulated by applying the distributional identity in Eq. (2.57). The $\mathcal{O}(\epsilon)$ terms proportional to $(1-\xi)$ we only hinted at in Eq. (4.78) will hence not contribute as they are only integrated together with the delta function $\delta(1-\xi)$. The final result then reads

$$\begin{aligned} \hat{\sigma}_{gg \rightarrow Hg} &= \frac{1}{576\pi^2} \frac{\alpha_s^3}{v^2} \left(\frac{s}{\mu^2} \right)^{-\epsilon} \Theta(1-\xi) \left\{ \left[\frac{3}{\epsilon^2} + \frac{3}{\epsilon} + 3 - \frac{3\pi^2}{4} \right] \delta(1-\xi) \right. \\ &\quad - \frac{6\xi}{\epsilon} \left[\frac{\xi}{(1-\xi)_+} + \frac{1-\xi}{\xi} + \xi(1-\xi) \right] (1+\epsilon) - \frac{11}{2} (1-\xi)^3 \\ &\quad \left. + 6 \left(\frac{\log(1-\xi)}{1-\xi} \right)_+ [1 + \xi^4 + (1-\xi)^4] \right\}. \end{aligned} \quad (4.79)$$

The poles proportional to the delta function $\delta(1 - \xi)$ exactly cancel between real (4.79) and virtual contributions (4.13). The remaining divergences should cancel after coupling and collinear renormalization. According to Eq. (2.38), the additional contribution from collinear renormalization is

$$\hat{\sigma}_{gg \rightarrow Hg}^C = 2 \times \frac{\alpha_s}{2\pi} \frac{1}{\epsilon} \int_0^1 dz P_{gg}^{(0)}(z) \hat{\sigma}_{gg \rightarrow H}(zs) = \frac{1}{576\pi^2} \frac{\alpha_s^3}{v^2} \frac{1}{\epsilon} \xi P_{gg}(\xi) (1 + \epsilon). \quad (4.80)$$

With the definition of the splitting kernel in Eq. (2.39), we see that the remaining poles in the real radiation contribution are indeed canceled. The additional pole introduced by the collinear renormalization is finally canceled by the charge renormalization. Gathering the fruits of our labor, we determined that the inclusive partonic cross section at NLO reads

$$\begin{aligned} \hat{\sigma}_{gg \rightarrow HX} = & \frac{\alpha_s^2}{576\pi v^2} \Theta(1 - \xi) \left\{ \delta(1 - \xi) \right. \\ & + \frac{\alpha_s}{\pi} \left[\delta(1 - \xi) \left(\pi^2 + \frac{11}{2} \right) - \frac{11}{2} (1 - \xi)^3 + 6 (1 + \xi^4 + (1 - \xi)^4) \left(\frac{\log(1 - \xi)}{1 - \xi} \right)_+ \right. \\ & \left. \left. + \xi P_{gg}(\xi) \log \left(\frac{s}{\mu^2} \right) \right] \right\} \end{aligned} \quad (4.81)$$

We can carry out the same analysis for the $q\bar{q}$ and qg channel. The Feynman diagrams are depicted in Fig. 4.7. The amplitude for $q\bar{q} \rightarrow Hg$ does not exhibit any collinear or soft

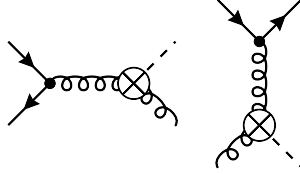


Figure 4.7: Feynman diagrams contributing to the $q\bar{q}$ (left) and qg (right) channel of the Higgs production cross section.

divergences, rendering collinear renormalization unnecessary. The result for the cross section reads

$$\hat{\sigma}_{q\bar{q} \rightarrow Hg} = \frac{1}{486\pi^2} \frac{\alpha_s^3}{v^2} \Theta(1 - \xi) (1 - \xi)^3. \quad (4.82)$$

The qg -channel on the other hand has a collinear divergence when the final state quark becomes collinear to the initial state quark. After collinear renormalization we find for the cross section

$$\begin{aligned} \hat{\sigma}_{qg \rightarrow Hg} + \hat{\sigma}_{qg \rightarrow Hg}^C = & \frac{\alpha_s^3}{576\pi^2 v^2} \Theta(1 - \xi) \\ & \times \left\{ (1 - \xi) \frac{3\xi - 7}{3} + \frac{1}{2} \xi P_{gq}(\xi) \left[1 + \log \left(\frac{s}{\mu^2} \right) + 2 \log(1 - \xi) \right] \right\}. \end{aligned} \quad (4.83)$$

After convolution of the partonic cross section with the partonic luminosity we get the hadronic cross section, which is displayed in Fig. 4.8 as a function of the hadronic center of mass energy. The cross section is split into the various channels. The “soft + virtual” channel denotes all contributions which originate from integrating the delta function $\delta(1 - \xi)$ and irreducible plus distributions, i.e. terms of the form

$$\left(\frac{f(\xi)}{1 - \xi} \right)_+ \mathcal{O}((1 - \xi)^0) \quad (4.84)$$

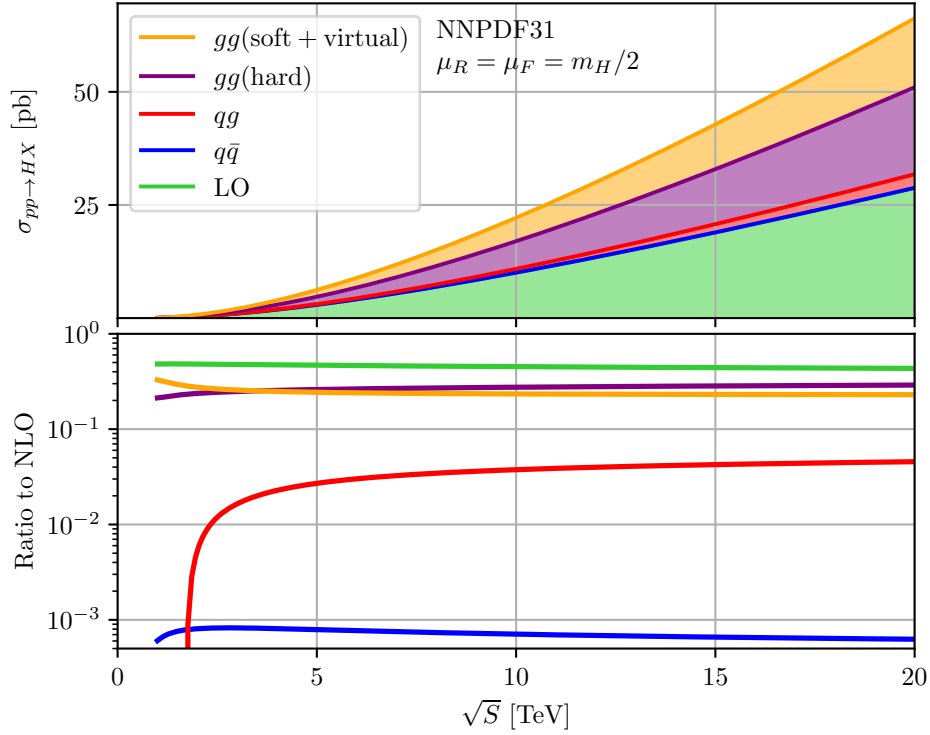


Figure 4.8: Hadronic cross section as function of the hadronic center of mass energy. The total cross section is partitioned into its various channels. The channel denoted “soft + virtual” collects the leading terms of the threshold expansion around $(1 - \xi)$ in Eq. (4.81), that is all terms proportional to $\delta(1 - \xi)$ and irreducible plus distributions. The lower plot shows the ratio of the various channels to the leading order cross section. Computational setup is described in the conventions.

At NLO, it only comes from gluon-induced Higgs production (4.13).

The majority of the hadronic cross section is due to a gluon-gluon initial state, making up more than 95% over the full spectrum of energies. Roughly half of this contribution comes from LO. The other half is composed, yet again of roughly two equal parts, the “soft + virtual” contribution and the remaining real radiation part. The quark-gluon initial state has the second largest impact, whereas the quark-quark induced Higgs production is completely negligible, contributing below 1%. The large suppression of the $q\bar{q}$ channel is almost entirely due to the reduced partonic luminosity of the channel. Indeed, from Fig. 2.3, we see that the $q\bar{q}$ flux is roughly 30 times smaller than the qg one. This is also the order of magnitude of the ratio of the qg and $q\bar{q}$ induced Higgs production cross section.

The gluon-gluon and quark-gluon luminosity on the other hand is rather similar, especially close to the production threshold, where most of the contributions to the cross section comes from, since larger values are suppressed by \mathcal{L}/τ . Yet we observe that quark-gluon-channel contribution is almost an order of magnitude smaller than in the gluon-gluon channel. To investigate the origin of this suppression, we can look at the coefficient of the logarithm $\log(\mu^2)$ which is predetermined by the RGE

$$\frac{\partial \hat{\sigma}_{qg \rightarrow Hq}}{\partial \log \mu^2} = -\frac{\alpha_s}{2\pi} \int_0^1 d\xi P_{gq}(\xi) \hat{\sigma}_{gg \rightarrow H}, \quad \frac{\partial \hat{\sigma}_{gg \rightarrow Hg}}{\partial \log \mu^2} = -2 \times \frac{\alpha_s}{2\pi} \int_0^1 d\xi P_{gg}(\xi) \hat{\sigma}_{qg \rightarrow H}. \quad (4.85)$$

At the threshold, the ratio quark-gluon to gluon-gluon logarithmic coefficients is thus $C_F/(4C_A) = 1/9$, which is also roughly the ratio we observed in their contribution to the cross section. The origin of the suppression, is thus partly due to the difference in the color factor and the additional combinatorial factors in the gluon-gluon channel.

Since the NLO corrections are of the same magnitude as the LO cross section, the perturbative result is not yet reliable. One would need to go to even more loops and higher multiplicities in the hope to reach perturbative convergence.

4.2.4 Phenomenological Application

Having discussed the HTL at length, it is important to investigate how well the approximation works for phenomenological applications. In Fig. 4.9, we show the relative error of the cross section in the HTL compared to the results with a finite quark mass for different powers of α_s in the various partonic channels.

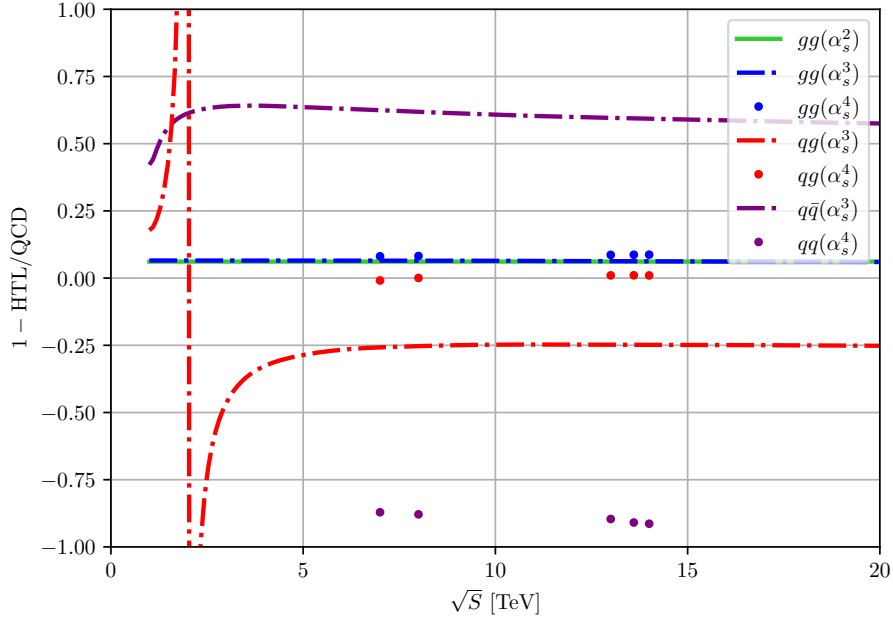


Figure 4.9: Relative error of the HTL compared to the results with finite top-quark mass for various center of mass energies. Displayed are contributions to the cross section in each partonic channels. The computational setup is described in the conventions. The methods to compute the NNLO results with finite top-quark mass are described in chapter 5.

At LO, the HTL underestimates the cross section by around 6.5%. In the HTL, the Higgs-gluon form factor, is accurate up to power corrections of order $z = m_H^2/4m_t^2 \approx 13\%$, so the observed accuracy of the approximation aligns with our expectations. For radiative corrections, $m_H^2/m_t^2 \approx 52\%$ is the more natural expansion parameter and the quark-gluon as well as the quark-quark channel show, that they are indeed only roughly 50% accurate.

The gluon-gluon channel on the other hand shows a remarkable property: the accuracy of the HTL stays quite constant across perturbative orders in α_s . In our opinion, this feed is explained by the fact, that much of the structure of the perturbative corrections is dictated by lower orders, and that, for this channel in particular, these kinds of corrections turn out to be numerically large. Indeed, we can apply *Catani's I operator* [63] to predict the poles, as well

as the overall factor $(-m_H^2/\mu^2)^{-\epsilon}$, of the Higgs-Gluon form factor in Eq. (4.70). So the part of the partonic cross section which is derived from LO reads

$$\begin{aligned} \hat{\sigma}_{gg \rightarrow H} \Big|_{\alpha\sigma_{gg \rightarrow H}^{(0)}} &= \frac{\pi}{576v^2} \xi \left(\frac{\alpha_s}{\pi} \right)^2 \delta(1 - \xi) \\ &\times \left[(1 + \epsilon + \mathcal{O}(\epsilon^2)) + \frac{\alpha_s}{\pi} \left(\frac{m_H^2}{\mu^2} \right)^{-\epsilon} \left(-\frac{3}{\epsilon^2} - \frac{3}{\epsilon} - 3 + \frac{3\pi^2}{2} + \mathcal{O}(\epsilon) \right) + \mathcal{O}(\alpha_s^2) \right]. \end{aligned} \quad (4.86)$$

Numerically, the finite part is largely dominated by the π^2 term which originated from the analytic continuation of the Sudakov (double) logarithm. The analytic continuation needed at time-like momentum transfer thus causes a large logarithm. The logarithm on the other hand stems from a soft gluon exchange in the loop.

For the real radiation cross section, we can once again already anticipate initial state collinear as well as the soft divergences

$$\begin{aligned} \hat{\sigma}_{gg \rightarrow Hg} &= \frac{1}{576\pi^2} \frac{\alpha_s}{v} (1 - \xi)^{-1-2\epsilon} \left(\frac{s}{\mu^2} \right)^{-\epsilon} \Theta(1 - \xi) \\ &\times \left[-\frac{1}{\epsilon} \xi(1 - \xi) P_{gg}^{(0)}(\xi) \frac{2(-1 + 2\epsilon)\Gamma(-\epsilon)}{\Gamma(3 - 2\epsilon)} + (1 - \xi)^2 \cdot (\dots) \right]. \end{aligned} \quad (4.87)$$

The $(1 - \xi)^2$ terms, which we denoted by (\dots) are finite and regular in the soft limit $\xi \rightarrow 1$. We know, that there cannot be any terms of order $(1 - \xi)$ apart from those in the splitting function, because every term in the matrix element (4.73) which is constant in the soft limit, still has collinear divergences in the phase-space. I.e. all next to soft contributions are captured in the splitting function. In fact, if we compare with the cross section in Eq. (4.78), then we see that the actual lowest order term is even $(1 - \xi)^4$.

The partonic luminosity together with the factor $1/\tau$ cause a strong enhancement of the phase-space region close to the threshold $\xi \rightarrow 1$ or $\tau \rightarrow m_H^2/S$. Therefore, the hadronic cross section will be well approximated by convoluting the inclusive cross section

$$\begin{aligned} \hat{\sigma}_{gg \rightarrow HX} \Big|_{\alpha\sigma_{gg \rightarrow H}^{(0)}} &= \frac{\alpha_s^2}{576\pi v^2} \Theta(1 - \xi) \left\{ \delta(1 - \xi) \right. \\ &+ \frac{\alpha_s}{\pi} \left[\delta(1 - \xi) \pi^2 \left(\frac{3}{4} + \mathcal{O}(1/\pi^2) \right) + 6(1 + \xi^4 + (1 - \xi)^4) \left(\frac{\log(1 - \xi)}{1 - \xi} \right)_+ \right. \\ &\quad \left. \left. + \xi P_{gg}(\xi) \log \left(\frac{s}{\mu^2} \right) \right] \right\}. \end{aligned} \quad (4.88)$$

Numerically, we find that the approximation is around 90% accurate at NLO. The main deviations are caused by the soft-virtual channel. We can therefore expect to see deviations in the rescaling factor

$$r^{\text{N}^n\text{LO}} = \frac{\sigma_{pp \rightarrow HX}^{\text{QCD, N}^n\text{LO}}}{\sigma_{pp \rightarrow HX}^{\text{HTL, N}^n\text{LO}}} \quad (4.89)$$

across perturbative orders of the order of $10\% \times z \approx 1\%$. **TODO:** Add reference to results for finite top-quark masses.

Strictly speaking, our discussion was limited to NLO. However, we claim that most of the arguments are transferable to higher orders in perturbation theory. Indeed, the factor π^2

from analytic continuation can be included to all order by resumming the Sudakov logarithm we encountered [64], i.e. the driving contribution is indeed proportional to the born cross section. This procedure is also sometimes referred to as π^2 -*resummmation*. At high orders of perturbation theory, it was demonstrated [62], that the quality of the resummation deteriorates, that mean that the Sudakov logarithms are no longer the driving contributor to the soft-virtual contribution. We can therefore expect to see larger deviations from the exact rescaling at higher orders. Similarly, our discussion on how to obtain the leading coefficients of the threshold expansion by requiring cancelation of initial-state collinear divergences can also be transferred to higher order [65]. At N³LO, one can correctly predict the three leading logarithms $\log^{5,4,3}(1 - \xi)$.

We can leverage the small corrections on the rescaling parameter to improve the HTL cross section results by rescaling the HTL results by

$$\sigma_{pp \rightarrow HX}^{\text{rHTL, N}^n\text{LO}} = r^{\text{LO}} \sigma_{pp \rightarrow HX}^{\text{HTL, N}^n\text{LO}}, \quad (4.90)$$

where the superscript “rHTL”, now refers to the *rescaled heavy top limit*. Since the gluon-gluon channel is the dominant production channel and the rescaling factor remains quite constant across the perturbative orders, the rHTL cross section will yield a good approximation ($\sim 1\%$) for the Higgs production cross section⁷.

4.3 THEORY STATUS

Having analyzed the gluon-gluon fusion Higgs production cross section at LO, and NLO in the HTL. We are now equipped with all concepts to discuss state-of-the-art theory predictions.

As already mentioned, the most precise theoretical predictions come from N³LO cross sections in the HTL [66, 62]. They apply the method of reverse unitarity (see section 2.2.3) to perform the phase-space integration fully analytically. The cross section is calculated in terms of a deep expansion in the threshold parameter $(1 - \xi)$

$$\hat{\sigma}_{ij \rightarrow HX} = \delta_{ig} \delta_{jg} \hat{\sigma}_{\text{SV}} + \sum_{n=0}^N c_{ij}^{(n)} (1 - \xi)^n, \quad (4.91)$$

where $\hat{\sigma}_{\text{SV}}$ is the leading term, the soft-virtual contribution we already encountered. The soft-virtual contribution has been calculated in Ref. [67]. Because the partonic luminosity is concentrated heavily around the threshold region, one would expect, to see good convergence of the hadronic cross section. Indeed, Ref. [66] computed the first 37 terms of the threshold expansion found that the hadronic cross section is already well approximated by the first five terms.

In the meantime, results without reliance on the threshold expansion have become available [68], confirming the expected accuracy of the threshold expansion and shifting the total cross section by around +0.10 pb at 13 TeV.

In Fig. 4.10 we show the results for the gluon-gluon fusion cross section in the rHTL at various perturbative orders as a function of the hadronic center of mass energy.

⁷ Excluding the effects from light quark masses.

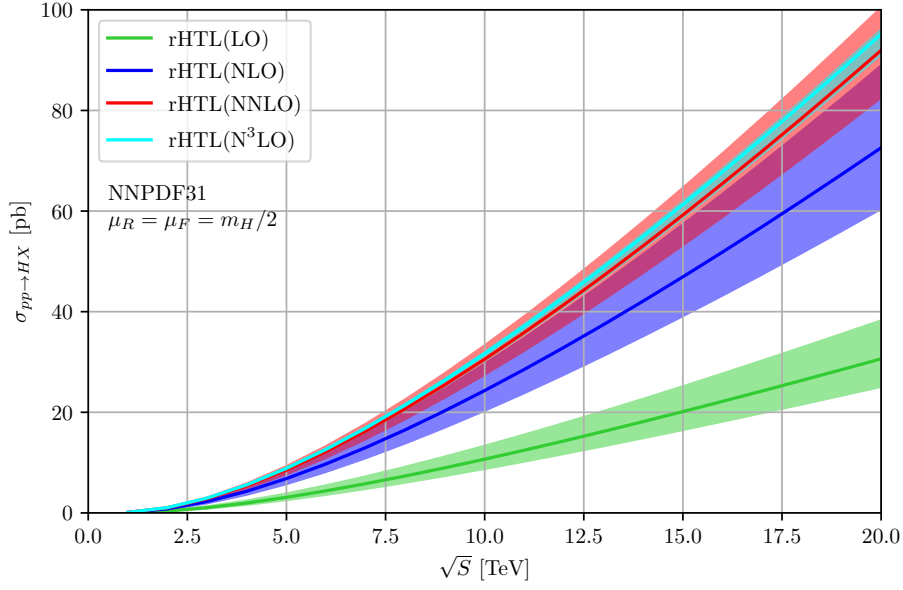


Figure 4.10: Gluon-gluon fusion hadronic cross section as a function of the center of mass energy. Displayed are results computed in the rHTL at various perturbative orders. Transparent bands indicate the scale uncertainty calculated by variation of μ_R in the range $[m_H/4, m_H]$. The computational setup is described in the conventions. The plot was created with the help of `SusHi` [69, 70].

As we discussed before, the NLO cross section is about twice as large as predicted in the Born approximation. NNLO corrections are still sizeable, contribution roughly 20% to the cross section. The NLO scale uncertainties underestimate the effect of higher orders, as the central NNLO cross section is outside the previous uncertainty bands. Only when we go to N³LO do we see perturbative convergence and corrections consistent with the previous scale uncertainty bands. The scale uncertainties at this order are below 4% for the displayed collision energies.

At this level of precision, it becomes important to investigate other sources of uncertainty and perform a careful evaluation of their impact on the cross section. The most important sources are

- The scale uncertainties,
- The PDF uncertainties,
- Uncertainties related to electroweak corrections,
- Uncertainties related to finite top-quark masses,
- Uncertainties related to light quarks.

In the following we will discuss them one-by-one.

4.3.1 Scale Uncertainties

Scale uncertainties serve as an estimate of missing higher order corrections. They are typically computed by 7-point-scale variation, that means the cross section is evaluated at a central scale

μ and the additional 6 points $(\mu_R, \mu_F) = (\mu/2, \mu/2), (\mu/2, \mu), (\mu, \mu/2), (2\mu, \mu), (\mu, 2\mu), (2\mu, 2\mu)$. The envelope of the cross section at the seven points then form the scale uncertainty. Since the renormalization and factorization scale is unphysical, physical observables like the cross section are in principle independent of the scales. However, as we are truncating the perturbative series at some fixed order, we are left with some residual dependence of the scale. The scale dependence is therefore a good indicator of missing higher orders. Even so, at low orders the scale uncertainties cannot always be trusted as Fig. 4.10 illustrates nicely.

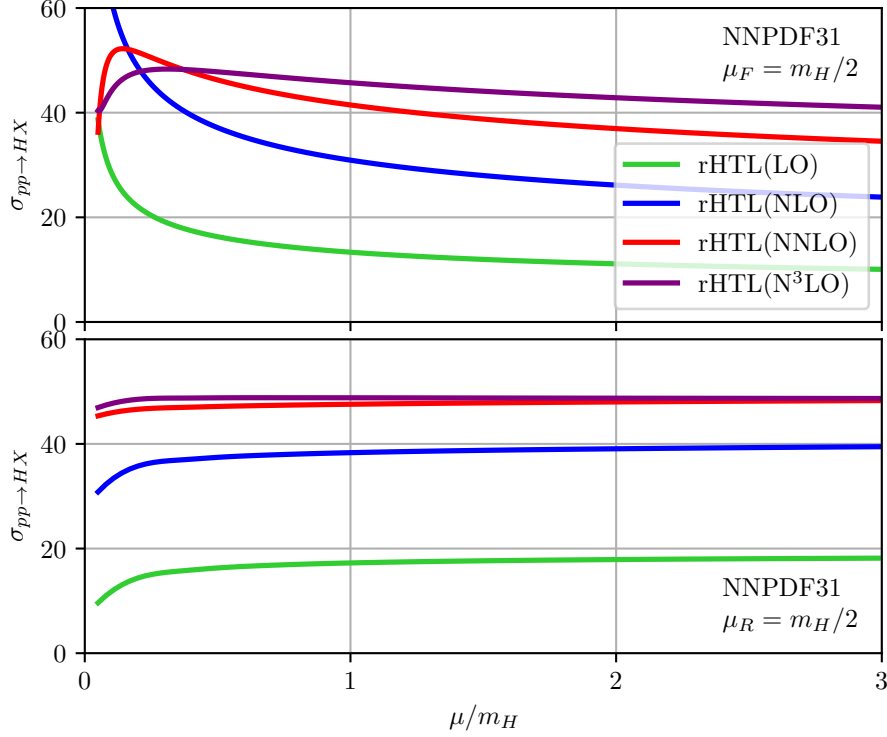


Figure 4.11: Hadronic cross section as a function of the renormalization scale (top panel) and factorization scale (bottom panel). The respective other scale is kept fixed at $m_H/2$. The computational setup is described in the conventions. The plot was created with the help of **SusHi** [69, 70].

Fig. 4.11 shows the functional dependence of the hadronic cross section on the renormalization and factorization scale for various perturbative orders. We see that there is very little dependence on the factorization scale, i.e. the vast majority of the scale uncertainties derive from the variation of renormalization scale. This also justifies, why the scale uncertainties in Fig. 4.10 are computed with a fixed factorization scale. We also observe that the dependence on the scale nicely stabilizes as we increase the perturbative precision. For the central scale, $\mu_R = \mu_F = m_H/2$ has become the de facto standard for the inclusive cross section and is also the recommendation of the Higgs Working Group [71]. The observed functional dependence in Fig. 4.11 supports this choice, as the $N^3\text{LO}$ corrections are minor at this scale and the cross section is particularly flat in this regime. It should be noted, that the miniature dependence on the factorization scale is only observed for the total cross section. If instead, we are considering individual production channels, the functional dependence remains very large, because the DGLAP equations mix the quark and gluon PDFs.

The scale uncertainties can be further reduced by including higher order corrections. Although full $N^4\text{LO}$ predictions are still beyond the current state-of-the-art in computational capabilities, we can predict at least some parts of the higher order corrections.

Results in the soft-virtual approximation

Since the partonic luminosity is sharply peaked around the threshold (see Fig. 2.3) $\xi \rightarrow 1$ or alternatively $\tau \rightarrow m_H^2/S$, we can get a good approximation of the hadronic cross section, by expanding the partonic cross section around the threshold as seen in Eq. (4.91). The leading term, i.e. the soft-virtual approximation has been already been computed up to 3 loops [72] in the HTL. Furthermore, as we discussed in section 4.2.4, the cancelation of initial state collinear divergences can be leveraged to determine the leading 3 logarithms of the first subleading term. This means that at N⁴LO we can predict the coefficients of the logarithms⁸

$$\log^{7,6,5}(1 - \xi) \quad (4.92)$$

in $c_{ij}^{(0)}$. This is especially important to stabilize the factorization scale dependence, since otherwise we would introduce an additional contribution to the cross section which is only present in one channel, the gluon-gluon channel, which would scale with running of the PDFs.

At the central scale of $\mu_R = \mu_F = m_H/2$, the partial N⁴LO results shift the cross section by around -0.1% . Scale uncertainties are reduced from around 4% to below 2.5%. The systematic uncertainty coming from the truncation of the threshold expansion is estimated by comparing the full cross section results with the soft-virtual approximation at lower order, and rescaling the error to the N⁴LO correction. The error is estimated to be well below 1% of the total cross section. **TODO: This seems very large. Ask Gotam!**

Threshold Resummation

The threshold logarithms appearing in $c_{ij}^{(0)}$ can actually be resummed to all orders. The Hadronic cross section can be cast into the form

$$\sigma(N) = \sum_{ij} f_i(N, \mu_F) f_j(N, \mu_F) \hat{\sigma}_{ij}(N, \mu_R, \mu_F), \quad (4.93)$$

where we switched from τ -space to N -space by means of a *Mellin transform*

$$\sigma(N) = \int_0^1 d\tau \tau^{N-1} \frac{\sigma(\tau)}{\tau}. \quad (4.94)$$

In N -space, also called *Mellin space*, the threshold region $\tau \rightarrow m_H^2/S$ corresponds to the limit $N \rightarrow \infty$. In this limit, it can be shown [73, 74, 75, 76], that the partonic cross section satisfies the resummed form

$$\hat{\sigma}_{ij}(N) = \delta_{ig} \delta_{jg} \hat{\sigma}_{gg \rightarrow H}^{\text{LO}} C_{gg} \exp[\mathcal{G}_H(\log N)] + \mathcal{O}(1/N). \quad (4.95)$$

C_{gg} collects all constant contributions for $N \rightarrow \infty$ and can therefore be extracted from lower orders in the large N limit. \mathcal{G}_H contains the threshold logarithms, which get resummed by exponentiation. It requires the cusp anomalous dimension, known today at four-loop accuracy [77], which enables the computation of full N³LO + next-to-next-to-next-to-leading logarithm cross section results. The results⁹ [62] show, that at the central scale, the fixed and resummed cross section is nearly identical. This can be interpreted as additional validation of our scale choice. Additionally, it confirms the N⁴LO soft virtual approximation, which also found that the corrections at the central scale are very close to zero.

π^2 -Resummation

In section 4.2.4, we showed that the soft-virtual contribution to the cross section is dominated

⁸ In fact one can also get parts of the $\log^4(1 - \xi)$ coefficient.

⁹ The authors of that reference use a Padé approximation for the four-loop cusp anomalous dimension, as the full result was still unknown at that point in time. They claim that the approximation is highly accurate.

by a Sudakov logarithm at time-like momentum transfer. This fact can be exploited to predict numerically large coefficients at higher orders and ultimately can be used to perform an all order resummation, sometimes referred to as π^2 -resummation [64].

Since the logarithm stems from a soft gluon exchange, we can apply techniques from *soft-collinear effective theory* (SCET) [78, 79] to map the Higgs-gluon form factor to a Wilson coefficient of SCET. In SCET we integrate out all the hard modes, such that we can approximate

$$G_{\mu\nu}^a G^{a\mu\nu} \longrightarrow C_S(-q^2)(-q^2)g_{\mu\nu}\mathcal{A}_{n\perp}^{a\mu}\mathcal{A}_{\bar{n}\perp}^{a\nu}, \quad (4.96)$$

where $\mathcal{A}_{n\perp}^{a\mu}$ and $\mathcal{A}_{\bar{n}\perp}^{a\nu}$ are effective, gauge invariant operators representing gluons traveling along the light-like directions n and \bar{n} defined by the momenta of the incoming hadrons. q^2 is the square of the momentum of the operator and C_S is the Wilson coefficient. The Higgs-gluon form factor in SCET, and hence the leading logarithmic contribution to the full Higgs-gluon form factor is then simply given by **TODO: Why?**

$$\mathcal{C}(0)\Big|_{\text{SCET}} = C_S(-m_H^2 - i0^+), \quad (4.97)$$

which we can use to match the Wilson coefficient

$$C_S(Q^2) = 1 + \frac{\alpha_s}{4\pi} C_A \left(-\ln^2\left(\frac{Q^2}{\mu^2}\right) + \frac{\pi^2}{6} \right). \quad (4.98)$$

The key benefit of working in the SCET framework, is that we can now apply RGE methods. Indeed, the Wilson coefficient satisfies the RGE

$$\frac{dC_S}{d\ln\mu} = \left[\Gamma_{\text{cusp}}^A \ln \frac{Q^2}{\mu^2} + \gamma^S \right] C_S, \quad (4.99)$$

where Γ_{cusp}^A is the cusp anomalous dimension of Wilson lines with light-like segments in the adjoint representation, and γ^S is the anomalous dimension of the operator. The solution of the differential equation, therefore automatically yields a resummed expression of the Higgs-gluon form factor. The solution can be written in terms of the recursive equation

$$\begin{aligned} |C_S(-m_H^2)|^2 &= U(m_H^2) |C_S(-m_H^2)|^2, \\ \text{with } \ln U(m_H^2) &= \frac{\alpha_s(m_H^2)}{\pi} \frac{C_A \pi^2}{2} \left\{ 1 + \frac{\alpha_s(m_H^2)}{4\pi} \left[C_A \left(\frac{67}{9} - \frac{\pi^2}{3} \right) - T_F n_l \frac{20}{9} \right] + \mathcal{O}(\alpha_s^2) \right\}. \end{aligned} \quad (4.100)$$

We see that the leading π^2 term matches our findings in Eq. (4.86).

The resummation drastically improves results at low order of perturbation theory. However, at higher orders, the quality of the resummation deteriorates. This indicates, that at these orders the factors of π^2 are no longer dominant. The procedure should therefore **not** be used to “improve” the N³LO cross sections.

4.3.2 PDF Uncertainties

All results presented so far, were computed using NNLO PDF sets, including all N³LO cross section results. This creates a mismatch between the hard scattering matrix elements and the PDFs, and the cross sections predictions do in fact not entirely have N³LO accuracy. The reason for applying PDF sets at NNLO accuracy is the lack thereof at N³LO.

PDFs are usually fitted to experimental data and then evolved to the desired scale using the DGLAP equation (2.44). To achieve N³LO accuracy, we therefore require

1. hard scattering amplitudes the PDFs can be matched to,
2. and the N³LO splitting functions for the DGLAP evolution.

Regarding the first point, the exact N³LO coefficient function for *deep-inelastic scattering* in the massless limit are known for a long time [80, 81, 82, 83, 84, 85], whereas massive coefficient functions are only available in approximation frameworks [86, 87]. Furthermore, N³LO predictions for charged- and neutral-current *Drell-Yan* production are also available, both for the total [88, 89, 90] and for differential cross sections [91, 92]. These processes are especially valuable for the matching of the PDFs, since there are experimentally very clean.

In Mellin space, the DGLAP equation (2.44) transforms from an integral-differential equation to just a partial differential equation

$$\frac{\partial f_{H,i}}{\partial \log \mu} = -\gamma_{ij}(N, \alpha_s(\mu)) f_{H,j}(N, \mu), \quad (4.101)$$

where $\gamma_{ij}(N, \alpha_s)$ is related to the Mellin transform of the splitting functions

$$\gamma_{ij}(N, \alpha_s(\mu)) = -\frac{\alpha_s}{\mu} \int_0^1 dx x^{N-1} P_{ij}(x, \alpha_s(\mu)). \quad (4.102)$$

Much progress has been made in evaluating specific moments of the splitting functions [93, 94, 95, 96, 97, 98, 99]. Additionally, parts of the splitting functions can be predicted through resummation techniques at low Bjorken- x , a leading logarithmic [100] and next-to-leading logarithmic [101, 102, 103] accuracy. Very recently, all splitting amplitudes were computed fully analytical by Mistlberger et al. [104], these describe the limit of amplitudes in which two of the external partons become collinear. It represents one important ingredient of the splitting kernel.

Although the evolution kernel are not yet fully known, the ingredients we do have can be still be used to at least construct an approximate N³LO PDF set. Results for such PDF sets were recently published by the MSHT [105] as well as the NNPDF [106] collaboration, which were then combined in Ref. [107]. They use the available data for deep-inelastic scattering and Drell-Yan production to fit the PDFs. For the running they use (most of) the known Mellin moments of the splitting kernels and smoothly interpolate between them.

In Fig. 4.12 and Tab. 4.2, we compare the gluon-gluon fusion rHTL cross section results at N³LO computed with different approximate N³LO PDF sets. The NNPDF40_an3lo_as_01180_mh0u includes *missing higher order uncertainties*. This encompasses the scale uncertainties of the hard scattering matrix elements the PDFs are fitted to, and estimates of the omitted terms in the incomplete N³LO splitting kernels. In the NNPDF40_an3lo_as_01180_pdfas PDF set, the replicas are created with different values of α_s between $\alpha_s(m_Z) = 0.117$ and 0.119, in order to estimate the α_s uncertainties. PDF sets ending with “_qed”, also include corrections from quantum electrodynamics (QED).

Before the publication of aN³LO PDF sets, the uncertainty due to the mismatch of the PDF was estimated through lower orders rescaled to N³LO

$$\delta(\text{PDF} - \text{th}) = \left| \sigma_{gg \rightarrow HX}^{\text{NNLO, NNLO PDF}} - \sigma_{gg \rightarrow HX}^{\text{NNLO, NLO PDF}} \right| \times \left(\frac{\sigma_{gg \rightarrow HX}^{\text{N}^3\text{LO}}}{\sigma_{gg \rightarrow HX}^{\text{NNLO}}} - 1 \right). \quad (4.103)$$

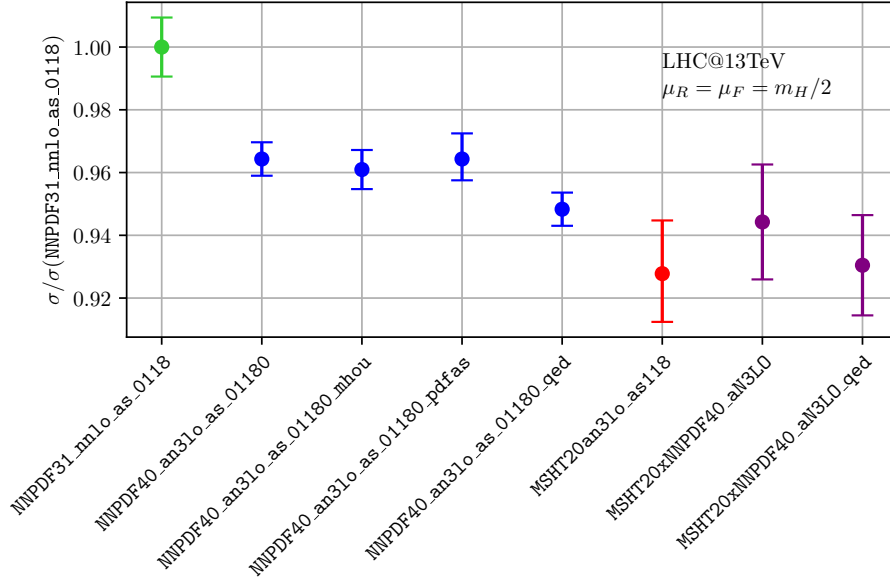


Figure 4.12: Gluon-Gluon fusion cross section in the rHTL at N³LO for various PDF sets normalized by the cross section computed with the `NNPDF31_nnlo_as_0118` PDF set. The provided uncertainties only include the PDF uncertainties. The uncertainty of the normalization is not propagated. The computational setup is described in the conventions. Results were computed using `iHixs 2` [108].

For the `NNPDF31_nnlo_as_0118` PDF set at 13 TeV, this uncertainty turns out to be close to 1%. However, from Fig. 4.12, we can see that with this approach the impact of the N³LO PDFs is severely underestimated, as the results computed with the aN³LOPDFs is shifted by around 4-6%.

We can also see that the different approaches followed by the `NNPDF` and `MSHT` collaboration, yield central values which are not compatible within the uncertainty bands. Furthermore, the PDF-uncertainty estimates differ by around a factor of three.

Provided that the provided missing higher order uncertainties are accurate, the approximations of the splitting kernel seems to be very accurate, effecting the cross sections only on the level of 1‰.

The α_s -uncertainties, make up about half of the total PDF uncertainty, as visible from the error increase between the `NNPDF40_an3lo_as_01180` and `NNPDF40_an3lo_as_01180_pdfas` PDF set.

The inclusion of QED effects shifts the cross section by around -0.6 pb at 13 TeV.

Because of considerably sized difference between the PDFs of the collaboration, we advise to use the combined PDF sets. We estimate the α_s and missing higher order uncertainties with the `NNPDF` PDF sets and rescale them by

$$\frac{\delta(\text{MSHT20xNNPDF40_aN3LO})}{\delta(\text{NNPDF40_an3lo_as_01180})} \approx 3.5, \quad (4.104)$$

where $\delta(\text{PDF})$ is the PDF uncertainty of the total cross section.

PDF	$\sigma_{gg \rightarrow HX}$ [pb]
NNPDF31_nnlo_as_0118	48.8 ± 0.46
NNPDF40_an3lo_as_01180	47.06 ± 0.26
NNPDF40_an3lo_as_01180_mhou	46.90 ± 0.30
NNPDF40_an3lo_as_01180_pdfas	$47.06^{+0.40}_{-0.33}$
NNPDF40_an3lo_as_01180_qed	46.28 ± 0.26
MSHT20an3lo_as118	$45.28^{+0.83}_{-0.75}$
MSHT20xNNPDF40_aN3LO	46.08 ± 0.89
MSHT20xNNPDF40_aN3LO_qed	45.41 ± 0.78

Table 4.2: Gluon-Gluon fusion cross section in the rHTL at N³LO for various PDF sets. The provided uncertainties only include the PDF uncertainties. The computational setup is described in the conventions. Results were computed using iHixs 2 [108].

4.3.3 Electroweak Corrections

Besides the discussed QCD corrections, we can also consider electroweak corrections. These are generally suppressed because of the smaller coupling constant $\alpha(m_Z) \approx 1/127$, but the percentage level precision of our predictions makes an investigation of electroweak effects indispensable.

The electroweak corrections to the LO QCD partonic cross section can be classified into two categories: the light-quark contributions and the top-quark contributions. The top-quark

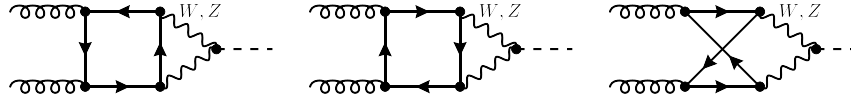


Figure 4.13: Light quark contribution to the LO electroweak corrections of the gluon-gluon fusion Higgs production cross section.

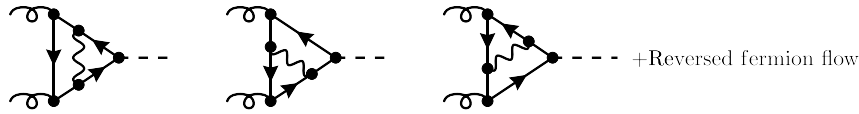


Figure 4.14: Top quark contribution to the LO electroweak corrections of the gluon-gluon fusion Higgs production cross section. The wavy line represents all electroweak gauge bosons (γ, W, Z).

contribution contains a Yukawa-coupling of the top, and the light quark contributions contains all the remaining diagrams. The respective diagrams are depicted in Fig. 4.13 and 4.14. Real radiative electroweak corrections like those depicted in Fig. 4.15, do not contribute to the cross section, since two diagrams which only differ by the direction of the fermion flow exactly cancel. Even though the preconditions are not strictly met this can be shown analogous to *Furry's theorem*¹⁰.

¹⁰ Furry's theorem states that the abelian part of the sum of two diagrams that differ only by the direction of a closed fermion vanishes, if there are an odd number of vertices proportional to the γ -matrices. In the present case, the color factor $\delta^{c_1 c_2}$, i.e. fully abelian. There is an even number of vertices, however one of the vertices is

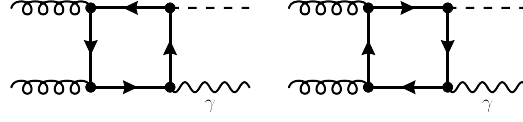


Figure 4.15: Example Feynman diagrams of radiative electroweak corrections to the gluon-gluon fusion Higgs production cross section. The remaining Feynman diagrams four diagrams can be obtained by permutation of external gluon, photon and Higgs. Two diagrams which differ only by the direction of the fermion flow exactly cancel.

The two-loop light-quark contribution to the Higgs-gluon form factor was calculated in Ref. [109]. The top-quark contribution was then worked out in Refs. [110, 111, 112]. The latter reference also includes the effect from finite bottom quark masses, including diagrams in which we encounter flavor changes due to a W -boson exchange. The leading electroweak corrections increase the LO cross section by around 5%. Almost the entirety of this correction is due to the light-quark contribution.

Beyond LO in α_s , the hadronic cross section was first estimated at $\mathcal{O}(\alpha_s^3\alpha)$ using the HTL and also treating the massive vector bosons as infinitely heavy [113]. Furthermore, since the top-quark contribution was negligible at LO, the authors only considered light-quark contribution to the cross section. With this approximation, the electroweak corrections can be incorporated through a modification of the Wilson coefficient

$$C_1 = \left[\frac{\alpha_s}{4\pi} C_1^{(0)} + \left(\frac{\alpha_s}{4\pi} \right)^2 C_1^{(1)} + \mathcal{O}(\alpha_s^3) \right] + \frac{\alpha}{4\pi} \left[\frac{\alpha_s}{4\pi} C_{1,w}^{(0)} + \left(\frac{\alpha_s}{4\pi} \right)^2 C_{1,w}^{(1)} + \mathcal{O}(\alpha_s^3) \right]. \quad (4.105)$$

One then finds for the electroweak coefficient

$$C_{1,w}^{(0)} = -\frac{2}{\sin^2 \theta_W \cos^2 \theta_W} \left[\frac{5}{4} - \frac{7}{3} \sin^2 \theta_W + \frac{22}{9} \sin^4 \theta_W \right] - \frac{4}{\sin^2 \theta_W}, \quad (4.106)$$

$$C_{1,w}^{(1)} = C_{1,w}^{(0)} \frac{14}{3}.$$

The same contribution was later reevaluated in the limit of massless electroweak gauge bosons [114], as well as in the soft-gluon approximation [115]. Even though, the approximations make completely different assumptions about the mass spectrum, the phenomenological results turn out to be quite similar, increasing the NLO cross section between 5.4 and 5.2%. This shows, that the cross section is not very sensitive to the mass of the vector bosons.

Still, results without relying on approximations would be highly desirable and were recently provided by Ref. [116]. The results found that the electroweak corrections increase the NLO cross section by around 5.1%, confirming that the previous approximations were indeed accurate. The $\mathcal{O}(\alpha_s^3\alpha^2)$ QCD predictions are rescaled to order $\mathcal{O}(\alpha_s^5\alpha^2)$ using the rHTL with electroweak corrected Wilson coefficients (see Eq. (4.105)). The electroweak corrections increase the N³LO rHTL cross section by $4.6 \pm 0.6\%$. By far the dominating error of this contribution comes from missing higher order uncertainties. Errors related to the omission of the top-quark contribution, finite quark-mass effects, or partonic channels at $\mathcal{O}(\alpha_s^3\alpha^2)$ make up less than 0.1%.

a Yukawa interaction and hence does not introduce a γ -matrix. It is easy to show that with these conditions, Furry's theorem still applies.

channel	$\sigma_{\text{rHTL}}^{\text{NNLO}}$ [pb]	$(\sigma_t^{\text{NNLO}} - \sigma_{\text{rHTL}}^{\text{NNLO}})$ [pb]		$(\sigma_t^{\text{NNLO}} - \sigma_{1/m_t}^{\text{NNLO}})$ [pb]
	$\mathcal{O}(\alpha_s^2) + \mathcal{O}(\alpha_s^3) + \mathcal{O}(\alpha_s^4)$	$\mathcal{O}(\alpha_s^3)$	$\mathcal{O}(\alpha_s^4)$	$\mathcal{O}(\alpha_s^4)$
$\sqrt{S} = 8 \text{ TeV}$				
gg	$7.39 + 8.58 + 3.88$	+0.0353	+0.0879	-0.047
qg	$0.55 + 0.26$	-0.1397	-0.0153	+0.001
qq	$0.01 + 0.04$	+0.0171	-0.0191	-
total	$7.39 + 9.14 + 4.18$	-0.0873	+0.0535	-0.046
$\sqrt{S} = 13 \text{ TeV}$				
gg	$16.30 + 19.64 + 8.76$	+0.0345	+0.2431	-0.145
qg	$1.49 + 0.84$	-0.3696	-0.0408	+0.015
qq	$0.02 + 0.10$	+0.0322	-0.0501	-
total	$16.30 + 21.15 + 9.70$	-0.3029	+0.1522	-0.130

Table 4.3: Comparison of cross sections computed in the rHTL (σ_{rHTL}), the cross section with finite top-quark masses (σ_t), and the cross section computed with power corrections (σ_{1/m_t}) at NNLO. The computational setup is described in the conventions. Exact results were extracted from Ref. [122]. The power corrections were computed using iHixs 2 [108]. The quark-quark channel is not yet available with power corrections, which is why we do not include it in the above table. The channel is suppressed by the PDFs, i.e. the total cross section will be left almost unaffected.

4.3.4 Finite Top-Quark Mass Effects

So far our discussion of perturbative corrections was mainly focused on the HTL approximation. In section 4.2.4, we explained how the approximation can be improved to also encompass some finite top-quark mass effects by means of rescaling the cross sections. We argued that in the dominating gluon-gluon channel especially, the rHTL approximation will be highly accurate. Nevertheless, we also saw significant deviations, in particular for the other partonic channels, which might yield important corrections to the rHTL cross section.

This makes the higher order corrections with finite top-quark mass indispensable. The LO calculation with finite top-quark masses presented in section 4.1 was extended to NLO in Refs. [117, 118]. Later, power corrections to the HTL of the form $\mathcal{O}(m_H^4/m_t^4)$ became available at NNLO [119, 120, 121]. Still, a residual theoretical uncertainty of about 1% of the total cross section persisted. Only with the computation of the exact top-quark mass dependence of the NNLO cross section [122] could the uncertainty be eliminated.

The main results of that reference are displayed in Tab. 4.3 (also see Fig. 4.9). We also compare the cross sections with exact top-quark mass dependence with the m_H/m_t expansion. We see that the finite-top-quark-mass effects are small ($< 0.4\%$). In the gluon-gluon channel the rHTL works exceptionally well, approximating the NNLO cross section with percent-level accuracy. Again we expect this kind of accuracy on the basis of the rescaling procedure. In the other partonic channels the approximation works significantly worse, showing deviations of up to 19%. The sheer dominance of the gluon-gluon channel assures that the total cross section is approximated well by the rHTL.

The power corrections m_H^4/m_t^4 power corrections to the HTL do not significantly improve the rHTL, but they do get the order of magnitude as well as the sign right.

The residual theoretical uncertainty of the finite-top-quark-mass effects can be estimated from the scale uncertainty of difference $\sigma_t - \sigma_{\text{rHTL}}$, taking into account all correlations. Alternatively, one may proceed as suggested by the *Higgs Working Group*¹¹ (HWG) [71] and estimate the uncertainty based on lower orders, rescaled to the N³LO cross section. At NNLO, this turns out to be less than 0.1‰ of the total cross section and is hence completely negligible. Since it is σ_t , not the difference of $\sigma_t - \sigma_{\text{rHTL}}$, which scales approximately with the rHTL cross section, we do not believe that this is an appropriate estimate of the error, and we will estimate the uncertainty based on the 7-point scale variation going forward.

Since the perturbative series of the cross section is truncated at some fixed order, it will have some residual renormalization scheme dependence. The scheme-dependence of the cross section was investigated in Ref. [62] and by us in Ref. [4]. The difference between the on-shell and $\overline{\text{MS}}$ scheme was found to be less than 1‰ of the total cross section, rendering also the uncertainty on the scheme dependence completely negligible.

4.3.5 Effect of Light Quarks

In section 4.1, we investigated to what extent light quarks effect the gluon-gluon fusion Higgs production cross section at LO. Here, we found that the main contribution arises from the interference with top-quark induced Higgs production. The inclusion of the bottom quark lowered the cross section by around 11% at 13 TeV. The next-heavy quark—the charm—further reduced the cross section, this time by 1.9%.

Since perturbative corrections are typically quite large in gluon-gluon fusion, it is once again vital to also compute higher order corrections to the interference. The NLO cross section for arbitrary quark masses was computed in Ref. [118].

Once again, we estimate the theoretical uncertainty for missing higher orders based the assigned scale uncertainties. The HWG, instead suggests estimating the uncertainty based on lower orders and rescale them to the N³LO correction in the rHTL. Since the light-quark-mass effects are not expected to scale with the cross section of the rHTL, we do believe that this is not reliable estimate of the uncertainty and do not apply them going forward.

The NLO results for the pure-flavor and the interference effects are displayed in Fig. 4.16. We see that the top-bottom interference contribution to the cross section increased in magnitude by 65% from LO to NLO. We once again observe that the top-bottom interference contribution is by far the most important one among the light quarks. All other light-quark mass effects are still within the scale uncertainty of the top-bottom contribution. Improving these contributions beyond NLO is therefore completely unnecessary. Interestingly, we observe that the scale uncertainties of the pure-top and the top-bottom contribution are almost perfectly anti-correlated.

With the scale uncertainty, we can estimate that effects due to missing higher orders of the light-quark contribution to be of the order of 7‰. However, this estimate is too naïve. Indeed,

¹¹ In the 2016 version of the HWG recommendations, they simply assign an uncertainty of 1\$ to the missing finite top quark mass effects at NNLO. With the publication of full NNLO cross sections with exact top-quark mass dependence, the theoretical uncertainty will be estimated similarly to what is described here in the upcoming update of the HWG recommendations.

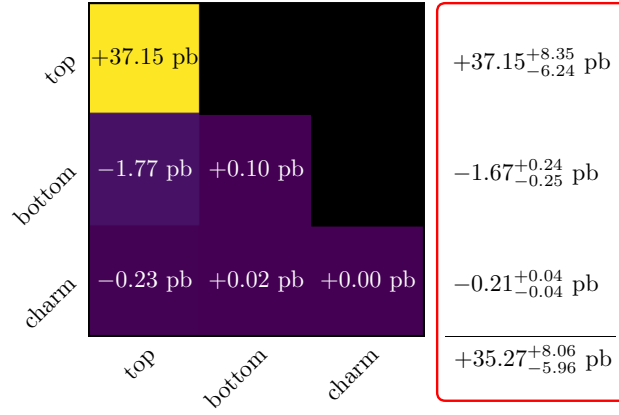


Figure 4.16: σ_i (diagonals) and $\sigma_{i \times j}$ (off-diagonals) at NLO for the three heaviest quark flavors at a hadronic center of mass energy of 13 TeV. The red box indicates the sum of each row, and hence the combined effects of each additional flavor. The computational setup is described in the conventions. We use the on-shell scheme for the top-quark mass and the $\overline{\text{MS}}$ scheme for the charm- and bottom-quark masses. The scale uncertainties are computed using 7-point variation.

if we choose a different renormalization scheme for the bottom quark mass, say the on-shell mass, the top-bottom interference contribution at NLO becomes (again at $\sqrt{S} = 13$ TeV)

$$\sigma_{t \times b} = -2.42^{+0.19}_{-0.12} \text{ pb}, \quad (4.107)$$

which differs from our previous $\overline{\text{MS}}$ renormalized cross section contribution by -0.66 pb or 38%. The large discrepancy between the results is somewhat expected, since the hard scattering amplitude in the high energy limit roughly scales with m_b^2 (see Eq. (4.12)) and the relation between the on-shell and the $\overline{\text{MS}}$ bottom-mass converges very poorly [123, 124]. Therefore, the cross section can only show a good perturbative convergence in one of the schemes if any. At NLO, we have not determined enough coefficients of the perturbation series to make a reliable argument about the convergence, making higher order predictions indispensable. If we assign the error in a way to encompass both the on-shell- and $\overline{\text{MS}}$ -renormalized results, it will constitute a 1.7% uncertainty on the total cross section, making it one of the leading sources of uncertainty.

Eliminating this source of uncertainty by computing higher order corrections to the top-bottom interference contribution is one of the major aims of this PhD thesis. With these predictions we want to investigate the perturbative convergence in the different mass-renormalization schemes.

The cross sections presented in this section were all computed in the 5FS, i.e. the bottom- and charm-quark were considered massless and could appear in the initial state. Since the hard scattering matrix element vanishes for massless particles, we then proceeded to set the light quark masses to non-vanishing values in all closed quark loops which couple to the Higgs¹². This ad hoc introduction of quark masses has become the de facto standard for light-quark mass effects in gluon-gluon fusion, but well grounded justifications of this procedure have been lacking so far. With this PhD thesis we want to close this gap, and explore the validity of this massification procedure by comparing the results of top-bottom-interference contributions to the same but computed in the 4FS, in which the quark-masses are treated consistently.

¹² We will later show that this method indeed ensures gauge-invariant IR-safe cross sections.

4.3.6 Differential Cross Sections

Up to this point our the main focus of our discussion has been the total cross section of the gluon-gluon fusion channel. However, differential cross sections can shine some light on the production kinematics of the Higgs and additionally offer a plethora of rich phenomenology and experimental applications. In this section, will briefly summarize the current status on differential cross sections of Higgs production in the gluon-gluon fusion channel. The possibilities to study the Higgs production cross section in terms of its kinematics are endless, so our discussion is by no means complete, instead we will focus on the most phenomenologically relevant distributions.

The Higgs- p_T Distribution

Arguably the most important distribution is the Higgs- p_T distributions

$$\frac{d\sigma_{pp \rightarrow HX}}{dp_T}, \quad (4.108)$$

where p_T is the transverse momentum of the Higgs with respect to the beam axis. p_T -distributions have been calculated up to third order in perturbation theory using the rHTL [125, 126], including subsequent decays to photons [127] and leptons [128]. The rHTL only provides as a good approximation of the cross section up to $p_T \sim m_H$. For larger p_T , the distribution is well described by a power law, which can be understood with a simple dimensional analysis. Indeed, at large p_T , the transverse momentum is the dominant scale, and we can neglect the top-quark mass. In order to match the mass dimension, -3 , of the differential partonic cross section $d\sigma_{pp \rightarrow HX}/dp_T$, we require the scaling behavior

$$\frac{d\hat{\sigma}_{ij \rightarrow HX}}{dp_T} \sim p_T^{-3}. \quad (4.109)$$

In the rHTL on the other hand, the coupling constant is proportional to $1/v^2$ and hence has a non-vanishing mass dimension. The large p_T scaling of the partonic cross section is therefore

$$\frac{d\hat{\sigma}_{ij \rightarrow HX}^{\text{rHTL}}}{dp_T} \sim v^{-2} p_T^{-1}. \quad (4.110)$$

Consequently, the ratio of the hadronic cross section in the rHTL and the exact theory must satisfy

$$\frac{d\sigma_{pp \rightarrow HX}^{\text{rHTL}}}{dp_T} \bigg/ \frac{d\sigma_{pp \rightarrow HX}}{dp_T} \sim p_T^2/v^2 \quad (4.111)$$

at $p_T \gg m_H$. The inclusion of finite top quark mass effects is therefore of immense importance especially at large p_T and has been studied up to NNLO in Refs. [129, 130, 131].

At smaller transverse momentum $p_T \sim m_H/2$ we can resolve the effects of the lighter quark masses. This is particularly interesting, because it demonstrates that this region is sensitive to the Yukawa coupling of the light quarks [132, 133]. In a recent study by the CMS collaboration [134], the authors fitted experimental data to the Higgs- p_T spectrum and could indirectly determine the following constraints on the coupling modifiers

$$-1.2 < \kappa_b < 1.1, \quad -4.9 < \kappa_c < 4.8. \quad (4.112)$$

The effect of light quark masses on the Higgs- p_T spectrum has been studied up to NNLO in Refs. [135, 136, 137, 4].

At LO and in all virtual corrections, the Higgs is produced with vanishing p_T , because there is no other final state particle, the Higgs could recoil against. The LO and all virtual corrections, will therefore only contribute to the zero-bin of the distribution. The transverse momentum hence acts as a slicing parameter. Consequently, at small transverse momentum, the cross section will receive large logarithmic enhancements because the cut-off threshold acts as an IR regulator. These logarithms cancel in the exact cross section, but due to the truncation of the perturbative series, fixed order results still suffer from their appearance and yield inaccurate results whenever these logarithms become dominant. To stabilize the behavior in these phase-space regions, the logarithms can be resummed to all orders [138, 129, 139, 140, 141, 142, 143, 144].

The Higgs-Rapidity Distribution

The Higgs rapidity is defined as

$$\eta_H \equiv \frac{1}{2} \ln \frac{p_H^0 + p_H^3}{p_H^0 - p_H^3}, \quad (4.113)$$

where p_H is the momentum of the Higgs, and the z -axis aligns with the beam direction. The rapidity is an inclusive observable, meaning that all contributions, be it real or virtual can contribute to any bin of the distribution. Consequently, the respective distribution will not show any logarithmic enhancements that require resummation as we saw for the p_T -distribution.

The Higgs-rapidity distribution has been calculated up to N³LO in the HTL [145, 146]. The effect of finite top-quark masses has been studied at NNLO in Ref. [144]. The effect of finite bottom quark masses on the other hand was recently presented by us [4] and will be discussed in this PhD thesis.

5 | COMPUTATIONAL DETAILS

Our final goal is clear now: We want to investigate the effect of finite top- and bottom-quark masses on the Higgs production cross section, both on the inclusive and the differential cross section level. In particular, we want to study the impact of the mass renormalization scheme on the cross section to eliminate one of the main remaining uncertainties of the cross section. Furthermore, in addition to the commonly used 5FS, we want to explore the impact of alternative FSs to assess the validity of the treatment of light quark masses in the 5FS.

In this chapter, we will describe the necessary methods for computing the Higgs production cross section with full top- and bottom-quark mass dependence at NNLO.

5.1 COMPUTING THE AMPLITUDES

The base ingredients of the calculation are the scattering amplitudes. In addition to the LO amplitude for $gg \rightarrow H$ presented in section 4.1 and the NLO amplitudes computed in Ref. [118], we require amplitudes for the following partonic processes

- Real-Real Corrections (One-loop):
 1. $gg \rightarrow Hgg$
 2. $gg \rightarrow Hq\bar{q}$
 3. $q\bar{q} \rightarrow Hq'\bar{q}'$
 4. + processes related by crossing symmetry
- Real-Virtual Amplitudes (Two-loop):
 1. $gg \rightarrow Hg$
 2. $q\bar{q} \rightarrow Hg$
 3. + processes related by crossing symmetry
- Virtual-Virtual Amplitudes (Three-loop):
 1. $gg \rightarrow H$.

In the following, we discuss the computation of each element one-by-one.

In this section, we are exclusively working in the 5FS. The necessary modifications for adapting the amplitudes to the 4FS will be presented in section 5.2. When working in the 5FS, the bottom-quark mass is generally zero. Since this would imply that the total top-bottom interference contribution is vanishing, one then sets the mass to its actual value inside all closed quark loops that couple to the Higgs. Therefore in Feynman diagrams like those depicted in Fig. 5.3, the bottom quark is treated as massive, but if the top- and bottom-quark are

exchanged, the bottom quark mass is set to zero. With a massification prescription like this, it is essential to verify that gauge invariance and IR safety are not lost in the process.

The proof that it is not proceeds by the replica technique. Consider the SM but only with the following quark content: n_b identical copies of the bottom quark, $n_{b'}$ massless quarks b' serving as our massless bottom quark, and the top-quark. Without the inclusion of electroweak effects this theory is equivalent to QCD with the addition of a Yukawa interaction to the Higgs; ergo this theory is gauge invariant and free of IR-divergences. Furthermore, gauge invariance and IR-safety also hold for each individual Yukawa coupling contribution (Y_t or Y_b) and each power of n_b and $n_{b'}$, as these are arbitrary parameters from the point of QCD. This means that the parts of the amplitude which are proportional to $Y_t n_b$ are separately gauge invariant, and so are the parts which are proportional to $Y_b n_b n_{b'}$, and so on. Examples of Feynman diagrams contributing to a selection of Y_t , Y_b , n_b and $n_{b'}$ power-combinations are depicted in Fig. 5.1. Likewise, after squaring, the contribution $Y_t Y_b n_b n_{b'}$ is going to be separately IR finite.

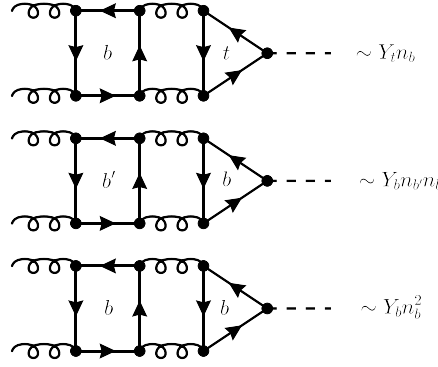


Figure 5.1: Example Feynman diagrams and their scaling with the Yukawa coupling, n_b , and $n_{b'}$.

We have thus shown, that contributions with a massive bottom-quark loop which does **not** couple to the Higgs does not mix gauge dependent terms or IR divergences with the selected contribution from our massification procedure.

5.1.1 The Real-Real Corrections

The real-real corrections only contain a single loop, with either a top or a bottom quark running in the loop. Examples of different Feynman diagrams for various partonic channels are depicted in Fig. 5.2.

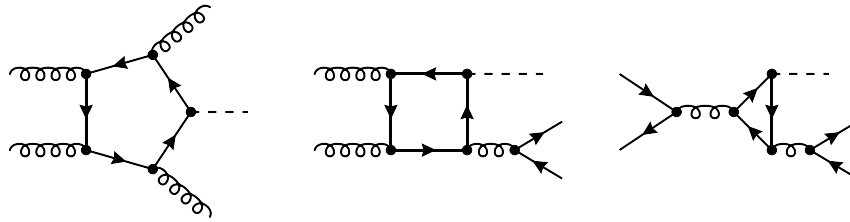


Figure 5.2: Example Feynman diagrams for one-loop real-real corrections in various partonic channels.

As one-loop amplitudes, they can be computed numerically with publically available libraries like **Recola** [147]. However, the real-real corrections often represent the bottleneck of the computation of the phase-space integrals, which makes an efficient evaluation of the amplitudes desirable. We therefore instead use the analytic form of the amplitude computed in Ref. [148]. We use the implementation of the amplitudes provided by **MCFM** [149, 150, 151], which in turn uses **QCDLoop** [152, 153] for the evaluation of one-loop integrals.

We found that with the analytic expressions, the evaluation time of the amplitudes is sped up by a factor of 20 compared to the numerical evaluation in **Recola**.

5.1.2 The Real-Virtual Corrections

For the real-virtual corrections we, for the first time encounter Feynman diagrams with two different mass scales running in the loop. Fig. 5.3 shows all (up to inversion of the fermion flow inside the triangle loops) Feynman diagrams with two internal quark loops. We observe,

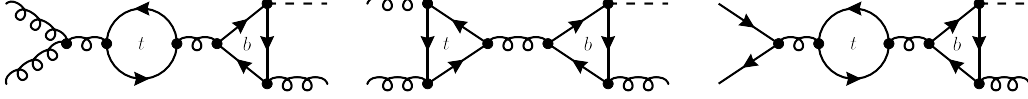


Figure 5.3: Feynman diagrams for the two-loop real-virtual corrections with two massive quarks. Amplitudes for the $qg \rightarrow Hq$ channel can be obtained via crossing from the $q\bar{q} \rightarrow Hg$ amplitudes. Triangle loops with reversed fermion flow are not explicitly shown. The external gluons must be accounted for with all permutations which render a different Feynman diagrams. In the 5FS, the bottom-quark is always coupling to the Higgs.

that all two-loop integrals actually factorize into two separate one-loop integrals making them quite straight-forward to solve.

The contributions to the scattering amplitude containing only a single massive quark involve genuine two-loop integrals. Fig. 5.4 shows a selection of contributing Feynman diagrams. Two loop integrals, especially non-planar ones, with three mass scales are very challenging

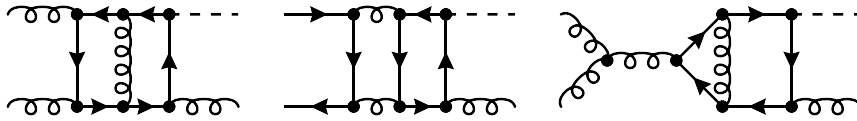


Figure 5.4: Example Feynman diagrams for the two-loop real-virtual corrections with a single massive quark in various partonic channels.

to compute analytically, even with state-of-the-art methods, and as of today the analytic computation of these amplitudes are still unknown, however approximations for a nearly massless bottom quark have been calculated relatively recently [154, 155]. We therefore decided to instead evaluate the appearing two-loop integrals numerically at fixed phase-space points and interpolate between them during the phase-space integration.

In any case, for both the one-mass and two-masses contribution we first have to reduce the amplitude to form factors. To make possible symmetries more apparent, we cross the radiated parton to the initial state, i.e. we consider the amplitudes

$$g(p_1) + g(p_2) + g(p_3) \longrightarrow H(p_4), \quad \bar{q}(p_1) + q(p_2) + g(p_3) \longrightarrow H(p_4). \quad (5.1)$$

Projection to Form Factors

We can factor out the external polarization vectors, spinors and color factors to rewrite the amplitudes in terms of their amputated counterpart

$$\mathcal{M}_{ggg \rightarrow H} = \mathcal{M}_{\mu\nu\rho} \epsilon_1^\mu \epsilon_2^\nu \epsilon_3^\rho f^{c_1 c_2 c_3}, \quad \mathcal{M}_{\bar{q}qg \rightarrow H} = \bar{v}(p_1) \mathcal{M}_\rho u(p_2) \epsilon_3^\rho T_{c_1 c_2}^{c_3}. \quad (5.2)$$

After squaring the amplitude and summing over the color of the external partons, we get the color factors

$$f^{c_1 c_2 c_3} f^{c_1 c_2 c_3} = C_A N_A = 24, \quad T_{c_1 c_2}^{c_3} T_{c_2 c_1}^{c_3} = C_F N_c = 4. \quad (5.3)$$

It is convenient, to choose polarization vectors which are cyclically transverse to the external momenta, i.e.

$$\epsilon_1 = \epsilon(p_1; p_2), \quad \epsilon_2 = \epsilon(p_2; p_3), \quad \epsilon_3 = \epsilon(p_3; p_1), \quad (5.4)$$

where the second argument indicates the gauge vector. We can then propose the form factor decomposition of the amplitudes

$$\begin{aligned} \mathcal{M}^{\mu\nu\rho} &= g^{\mu\nu} p_2^\rho F_1 + g^{\mu\rho} p_1^\nu F_2 + g^{\nu\rho} p_3^\mu F_3 + p_3^\mu p_1^\nu p_2^\rho F_4, \\ \bar{v}(p_1) \mathcal{M}^\rho u(p_2) &= \bar{v}(p_1) \left[\not{p}_3 p_1^\rho - (p_1 \cdot p_3) \gamma^\rho \right] u(p_2) G_1 + \bar{v}(p_1) \left[\not{p}_3 p_2^\rho - (p_2 \cdot p_3) \gamma^\rho \right] u(p_2) G_2. \end{aligned} \quad (5.5)$$

We used the Ward identity, to restrict the tensor coefficients in \mathcal{M}^ρ . $\mathcal{M}^{\mu\nu\rho}$ also satisfies Ward identity.

The tensor coefficients span a vector space with respect to the scalar product

$$\langle a_{\mu_1, \dots, \mu_{n_g}} | b^{\mu_1, \dots, \mu_{n_g}} \rangle \equiv \sum_{\text{pol.}} a_{\mu_1, \dots, \mu_{n_g}}^* \left[\prod_i^{n_g} \epsilon_i^{*\mu_i} \epsilon_i^{\nu_i} \right] b_{\nu_1, \dots, \nu_{n_g}} \quad (5.6)$$

where n_g is the number of external gluons, i.e. $n_g = 3$ for $ggg \rightarrow H$ and $n_g = 1$ for $\bar{q}qg \rightarrow H$ and the summation is performed over the polarizations of all external particles. The tensor coefficients hence form a—not necessary orthonormal—basis.

Any vector can be written as a linear sum over basis vectors

$$|v\rangle = \sum_i v_i |e_i\rangle. \quad (5.7)$$

Then the projector to the j -th basis vector can be found via

$$\langle e_j | P \equiv P_j = \sum_k G_{jk}^{-1} |e_k\rangle, \quad (5.8)$$

where G is the Gram-matrix

$$G_{ij} = \langle e_i | e_j \rangle. \quad (5.9)$$

With this little interlude from linear algebra it is then easy to verify that the projectors for the F_1, \dots, F_4 form factors are given by

$$\begin{aligned} P_1^{\mu\nu\rho} &= \frac{1}{d-3} \left(g^{\mu\nu} p_2^\rho \frac{t}{su} - p_3^\mu p_1^\nu p_2^\rho \frac{1}{su} \right), \\ P_2^{\mu\nu\rho} &= \frac{1}{d-3} \left(g^{\mu\rho} p_1^\nu \frac{u}{st} - p_3^\mu p_1^\nu p_2^\rho \frac{1}{st} \right), \\ P_3^{\mu\nu\rho} &= \frac{1}{d-3} \left(g^{\nu\rho} p_3^\mu \frac{s}{tu} - p_3^\mu p_1^\nu p_2^\rho \frac{1}{tu} \right), \\ P_4^{\mu\nu\rho} &= \frac{1}{d-3} \left(-g^{\mu\nu} p_2^\rho \frac{1}{su} - g^{\mu\rho} p_1^\nu \frac{1}{st} - g^{\nu\rho} p_3^\mu \frac{1}{tu} + p_3^\mu p_1^\nu p_2^\rho \frac{d}{stu} \right). \end{aligned} \quad (5.10)$$

To be even more explicit: the form factors are given by

$$F_i = \langle e_i | P_{\mu\nu\rho} | \mathcal{M}^{\mu\nu\rho} \rangle = P_i^{\mu_1\nu_1\rho_1} \left(-g_{\mu_1\mu_2} + \frac{p_1\mu_1 p_2\mu_2 + p_2\mu_1 p_1\mu_2}{p_1 \cdot p_2} \right) \\ \times \left(-g_{\nu_1\nu_2} + \frac{p_2\nu_1 p_3\nu_2 + p_3\nu_1 p_2\nu_2}{p_2 \cdot p_3} \right) \left(-g_{\rho_1\rho_2} + \frac{p_3\rho_1 p_1\rho_2 + p_1\rho_1 p_3\rho_2}{p_3 \cdot p_1} \right) \mathcal{M}^{\mu_2\nu_2\rho_2}. \quad (5.11)$$

Here we used the standard identity

$$\sum_{\lambda} \epsilon_{\mu}^*(p, n, \lambda) \epsilon_{\nu}(p, n, \lambda) = -g_{\mu\nu} + \frac{p_{\mu} n_{\nu} + p_{\nu} n_{\mu}}{p \cdot n} \quad (5.12)$$

to rewrite the sum over the polarization vectors.

Similarly, using

$$\sum_{\lambda} u(p, \lambda) \bar{u}(p, \lambda) = \not{p}, \quad \text{and} \quad \sum_{\lambda} v(p, \lambda) \bar{v}(p, \lambda) = \not{p}, \quad (5.13)$$

we find the projectors of G_1 and G_2 ¹

$$\bar{v}(p_1) P_1^{\mu} u(p_2) = \frac{1}{2st(d-3)} \bar{v}(p_1) \left[\frac{d-2}{t} \left(\not{p}_3 p_1^{\mu} - \frac{t}{2} \gamma^{\mu} \right) - \frac{d-4}{u} \left(\not{p}_3 p_2^{\mu} - \frac{u}{2} \gamma^{\mu} \right) \right] u(p_2), \\ \bar{v}(p_1) P_2^{\mu} u(p_2) = \frac{1}{2su(d-3)} \bar{v}(p_1) \left[\frac{d-2}{u} \left(\not{p}_3 p_2^{\mu} - \frac{u}{2} \gamma^{\mu} \right) - \frac{d-4}{t} \left(\not{p}_3 p_1^{\mu} - \frac{t}{2} \gamma^{\mu} \right) \right] u(p_2). \quad (5.14)$$

These allow the extraction of the form factors via

$$G_i = \langle e_i | P_{\mu} | \mathcal{M}^{\mu} \rangle = \left(-g_{\mu_1\mu_2} + \frac{p_3\mu_1 p_1\mu_2 + p_1\mu_1 p_3\mu_2}{p_3 \cdot p_1} \right) \text{tr} \{ P_i^{\mu_1} \mathcal{M}^{\mu_2} \}, \quad (5.15)$$

where we have used Eq. (5.13) once again, to rewrite the polarization sum in terms of a Dirac-trace.

Helicity Amplitudes

Since the form factors dependent on the choice of our tensor basis, we would rather express our end result in terms of helicity amplitudes

$$\mathcal{M}_{ggg \rightarrow H}^{\lambda_1 \lambda_2 \lambda_3} = \mathcal{M}_{\mu\nu\rho} \epsilon^{\mu}(p_1, p_2, \lambda_1) \epsilon_2^{\nu}(p_2, p_3, \lambda_2) \epsilon_3^{\rho}(p_3, p_1, \lambda_3), \\ \mathcal{M}_{q\bar{q}g \rightarrow H}^{\lambda_1 \lambda_2 \lambda_3} = \bar{v}(p_1, \lambda_1/2) \mathcal{M}_{\rho} u(p_2, \lambda_2/2) \epsilon_3^{\rho}(p_3, p_1, \lambda_3). \quad (5.16)$$

To find the relation between the form factors and the helicity amplitudes, we consider all independent helicity configurations and use the *spinor-helicity formalism* (see Ref. [156] for a pedagogical introduction to the topic) to rewrite them in terms of spinor products

$$\langle ij \rangle \equiv \bar{u}(p_i, -1/2) u(p_j, 1/2), \quad [ij] \equiv \bar{u}(p_i, 1/2) u(p_j, -1/2). \quad (5.17)$$

The results for the $ggg \rightarrow H$ amplitudes read

$$\mathcal{M}_{ggg \rightarrow H}^{+++} = \frac{1}{\sqrt{2}} \frac{su}{\langle 12 \rangle \langle 23 \rangle \langle 31 \rangle} \left(F_1 + \frac{t}{u} F_2 + \frac{t}{s} F_3 + \frac{t}{2} F_4 \right), \\ \mathcal{M}_{ggg \rightarrow H}^{++-} = \frac{1}{\sqrt{2}} \frac{[12]^3}{[13][23]} \frac{u}{s} \left(F_1 + \frac{t}{2} F_4 \right), \\ \mathcal{M}_{ggg \rightarrow H}^{+-+} = \frac{1}{\sqrt{2}} \frac{[13]^3}{[12][23]} \frac{s}{t} \left(F_2 + \frac{u}{2} F_4 \right), \\ \mathcal{M}_{ggg \rightarrow H}^{-++} = \frac{1}{\sqrt{2}} \frac{[23]^3}{[12][13]} \frac{t}{u} \left(F_3 + \frac{s}{2} F_4 \right). \quad (5.18)$$

¹ Note that the projectors are defined as the entire left-hand side.

The other four helicity amplitudes can be determined via charge conjugation

$$\mathcal{M}^{\lambda_1, \lambda_2, \lambda_3} = \mathcal{M}^{-\lambda_1, -\lambda_2, -\lambda_3} \Big|_{\langle ij \rangle \leftrightarrow [ji]}. \quad (5.19)$$

Similarly, for the $\bar{q}qg \rightarrow H$ process we find the helicity amplitudes

$$\begin{aligned} \mathcal{M}_{\bar{q}qg \rightarrow H}^{-++} &= -\frac{1}{\sqrt{2}} \frac{[13]^2}{[12]} sF_1, \\ \mathcal{M}_{\bar{q}qg \rightarrow H}^{+-+} &= \frac{1}{\sqrt{2}} \frac{[23]^2}{[12]} sF_2. \end{aligned} \quad (5.20)$$

The $+-+$ and $-+-$ amplitudes can be determined with Eq. (5.19) and all other helicity configurations render vanishing amplitudes due to the conservation of angular momentum.

The form factors, amplitudes and helicity amplitudes admit a perturbative expansion in α_s . We define

$$\mathcal{M}_{ijk \rightarrow H}^{\lambda_1 \lambda_2 \lambda_3} = \frac{4\pi}{v} \left(\frac{\alpha_s}{4\pi} \right)^{3/2} \sum_{i=0} \left(\frac{\alpha_s}{4\pi} \right)^i \mathcal{M}^{(i), \lambda_1 \lambda_2 \lambda_3}. \quad (5.21)$$

Mapping to Topologies and the Reduction to Master Integrals

We generate all diagrams with **DiaGen/IdSolver**, our in-house software tool for the generation of Feynman diagrams. As output, we obtain **FORM** [157, 158] code we can further manipulate. We apply the color algebra and project to the form factors as described above. **DiaGen/IdSolver** is also capable to find *prototypes*, i.e. it automatically identifies a minimal set of integral families and assigns appearing integrals accordingly.

In principle, **DiaGen/IdSolver** is also able to find relations between appearing Feynman integrals, so called *integration-by-parts identities* (IBP), by means of the *Laporta algorithm* [159]. However, due to the immense complexity of the problem at hand, intermediate expressions are prone to become very large. This makes solving the appearing linear system of equation by traditional methods like Gaussian elimination highly inefficient. The appearance of large intermediate expressions can be circumvented by using *finite field* methods. In a nutshell, one inserts fractional samples for the appearing kinematic invariants and then performs the Laporta algorithm with reduced kinematics, making it much simpler to solve. The final IBP identities relate the master integrals by rational functions, one can then reconstruct the functional dependence on the kinematic variables through repeated sampling, like when performing a fit. The rational values are mapped to finite fields—explaining the name of the method—which allows computations without loss of precision. We use this workflow implemented in the publically available tool chain **Kira** \oplus **Firefly** [160, 161, 162].

After application of the IBP identities we end up with three integral families for amplitudes with a single internal massive quark. We adapt the definition provided in Ref. [154]. The propagators of the each family are printed in Tab. 5.1. Notice, that the Feynman diagrams can never have more than seven internal lines, meaning that integrals appearing in physical amplitudes are missing at least two of the propagators. The physical subsector of the integral families are depicted graphically in Figs. 5.5, 5.6, and 5.7. For the contributions containing two massive internal quarks, we do not provide the integral families since the two-loop integrals factorize to one-loop integrals.

UV-Renormalization, IR-Subtraction and LSZ-Reduction

So far our analysis was concerned with bare amplitudes regulated in dimensional regularization. The UV-poles are eliminated through renormalization of the coupling constant and the quark masses. Following the description in section 2.2 we replace the bare coupling constant and

#	Planar 1 (PL1)	Planar 2 (PL2)	Non-planar (NPL)
1	k_1^2	$k_1^2 - m^2$	$k_1^2 - m^2$
2	$(k_1 - p_1)^2$	$(k_1 - p_1)^2 - m^2$	$(k + p_1)^2 - m^2$
3	$(k_1 - p_1 - p_2)^2$	$(k_1 - p_1 - p_2)^2 - m^2$	$(k_1 - p_2 - p_3)^2 - m^2$
4	$(k_1 - p_1 - p_2 - p_3)^2$	$(k_1 - p_1 - p_2 - p_3)^2 - m^2$	$k_2^2 - m^2$
5	$k_2^2 - m^2$	$k_2^2 - m^2$	$(k_2 + p_1)^2 - m^2$
6	$(k_2 - p_1)^2 - m^2$	$(k_2 - p_1)^2 - m^2$	$(k_2 - p_3)^2 - m^2$
7	$(k_2 - p_1 - p_2)^2 - m^2$	$(k_2 - p_1 - p_2)^2 - m^2$	$(k_1 - k_2)^2$
8	$(k_2 - p_1 - p_2 - p_3)^2 - m^2$	$(k_2 - p_1 - p_2 - p_3)^2 - m^2$	$(k_1 - k_2 - p_2)^2$
9	$(k_1 - k_2)^2 - m^2$	$(k_1 - k_2)^2$	$(k_1 - k_2 - p_2 - p_3)^2$

Table 5.1: Integral families for all contributions with only one internal massive quark as defined in Ref. [154]. m is the mass of the internal top- or bottom-quark.

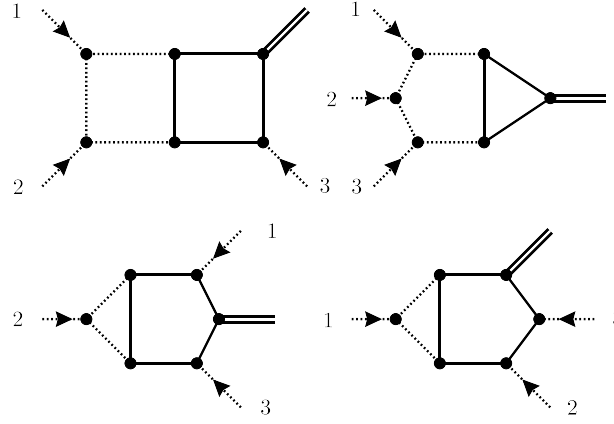


Figure 5.5: Graphical representation of the physical sectors embedded in the first integral family (PL1). Dotted lines represent massless propagators, while solid lines have the quark mass in the propagator.

masses by their renormalized counterparts and subsequently expand in α_s . The $\alpha_s^{5/2}$ term is singled out to get the NNLO correction to the amplitude. We employ the $\overline{\text{MS}}$ scheme for the α_s , and—for now—the OS scheme for all the quark masses.

To obtain physical amplitudes, we employ the LSZ reduction formula. This means for each external particle, multiplying by the square root of the corresponding LSZ-constant. In dimensional regularization, the LSZ constants only get contributions from heavy fields, since all other contributions render scaleless integrals. This means that the gluon LSZ constants are already non-trivial at one-loop, whereas the quark LSZ constants only gets non-trivial corrections at two-loop, which makes them irrelevant for the calculation at hand. Since bottom-quarks are treated as massless whenever they are not coupling to the Higgs, they do not contribute to the LSZ constants, i.e. only the top-quark mass enters the LSZ constants.

The remaining poles are of IR origin. They would cancel against poles arising during phase-space integration, so we can subtract them already on the amplitude level. We employ the $\overline{\text{MS}}$ scheme and subtract only the divergences predicted by the \mathbf{Z} operator (see for example Ref. [42]).

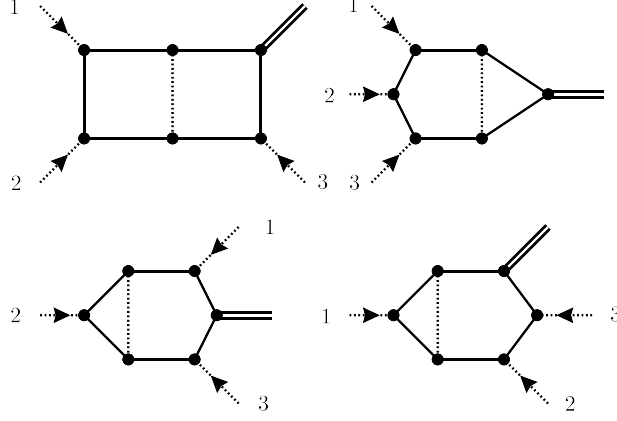


Figure 5.6: Same as Fig. 5.5 but for the second integral family (PL2).

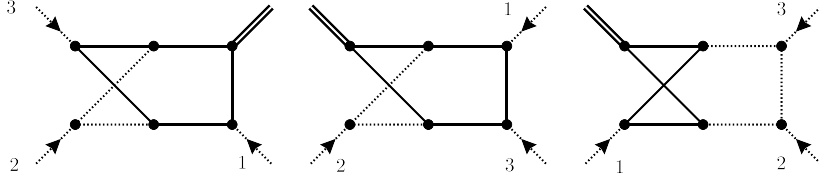


Figure 5.7: Same as Fig. 5.5 but for the third non-planar integral family (NPL).

Results for the Contributions with Two Heavy Quarks

Once we performed all the above steps, we separate the contributions which contain two heavy quark loops from the rest of the amplitude. The IR-poles, do not receive contributions from heavy internal lines and are therefore irrelevant for this contribution. The LSZ constants of the gluons on the other hand, do contribute. In the coupling renormalization constants, we single out the contributions from the top quark, i.e. we set the number of fermions to

$$n_f = n_l + n_h \quad (5.22)$$

Here n_l is the number of light quarks, and n_h is the number of heavy quarks. In the 5FS we have $n_l = 5$ and $n_h = 1$. The renormalization constant in the $\overline{\text{MS}}$ scheme then reads

$$Z_g = 1 - \frac{\alpha_s}{4\pi} 2\beta_0 \frac{1}{\epsilon} + \mathcal{O}(\alpha_s^2) = 1 + \frac{\alpha_s}{4\pi} \frac{1}{\epsilon} \left(-\frac{11}{6} C_A + \frac{2}{3} (n_l + n_h) T_F \right) + \mathcal{O}(\alpha_s^2). \quad (5.23)$$

To single out the contributions from the top-quark we only take terms proportional to n_h and set n_h to one afterwards. We can then apply the decoupling relations of Eq. (4.59) to replace the coupling constant by its decoupled counterpart in the lower order amplitudes². We can absorb these terms into the renormalization of the coupling constant, such that we end up with the effective renormalization constant

$$Z_g^{(n_l)}|_{\alpha_{n_h}} = \frac{\alpha_s}{4\pi} \frac{2}{3} T_F \left(\frac{1}{\epsilon} - \ln \left(\frac{m_t^2}{\mu^2} \right) \right) + \mathcal{O}(\alpha_s^2). \quad (5.24)$$

This is nothing else than the top-quark contribution to the OS coupling renormalization constant. The decoupling constants were specifically introduced to cure the $\overline{\text{MS}}$ scheme from

² In the renormalization constants we can simply set $\alpha_s^{(n_l+n_h)} = \alpha_s^{(n_l)}$ at this order in perturbation theory.

the appearance of non-decoupling effects. In the OS scheme this issue does not arise because of the Appelquist-Carrazone theorem (see section 4.2.2). The equality of the renormalization constants is therefore not accidental.

At one-loop, the top-quark contribution to the renormalization constant is of abelian nature. In QED, the Ward identity implies the all order relation $Z_e = Z_3^{-1/2}$. We can therefore conclude, or verify explicitly that the one-loop renormalization constant is also related to the gluon LSZ constant

$$2Z_g^{(n_l)}|_{\alpha_{n_h}} = -Z_3 + \mathcal{O}(\alpha_s^2). \quad (5.25)$$

This has the profound effect, that if the external number of gluons is identical to the power of the coupling constant (at lower order), then the contributions exactly cancel. This is for example the case in the $ggg \rightarrow H$ amplitude.

The result for the helicity amplitude of the $ggg \rightarrow H$ amplitude read

$$\begin{aligned} \mathcal{M}_{ggg \rightarrow H}^{(1),+++} \Big|_{2 \text{ masses}} &= \frac{1}{\sqrt{2}} \frac{1}{\langle 12 \rangle \langle 23 \rangle \langle 31 \rangle} \left\{ -\frac{4m_t^2 stu}{(s+t)} \tilde{C}_0(u, m_t^2) \left[\tilde{B}(m_H^2, m_b^2) \right. \right. \\ &\quad \left. \left. + \frac{s+t}{u} + 2\frac{m_b^2}{u} (4m_b^2 - s - t) \tilde{C}_1(u, m_H^2, m_b^2) - \frac{4m_b^2}{s+t} \tilde{B}(u, m_l^2) \right] \right. \\ &\quad \left. + (s \rightarrow t, t \rightarrow u, u \rightarrow s) + (s \rightarrow u, u \rightarrow t, t \rightarrow s) \right\} \end{aligned} \quad (5.26)$$

$$\begin{aligned} \mathcal{M}_{ggg \rightarrow H}^{(1),-++} \Big|_{2 \text{ masses}} &= -\frac{1}{\sqrt{2}} \frac{[23]^3}{[12][13]} \frac{4m_t^2 st}{u(s+t)} \tilde{C}_0(u, m_t^2) \left[\tilde{B}(m_H^2, m_b^2) \right. \\ &\quad \left. + \frac{s+t}{u} + 2\frac{m_b^2}{u} (4m_b^2 - s - t) \tilde{C}_1(u, m_H^2, m_b^2) - \frac{4m_b^2}{(s+t)} \tilde{B}(u, m_b^2) \right] \end{aligned} \quad (5.27)$$

Where we defined the auxiliary functions³

$$\begin{aligned} \tilde{B}(s, m^2) &\equiv \beta(s, m^2) \log \left(-\frac{1 - \beta(s, m^2)}{1 + \beta(s, m^2)} + i0^+ \right), \\ \tilde{C}_0(s, m^2) &\equiv \frac{1}{2s} \log^2 \left(-\frac{1 - \beta(s, m^2)}{1 + \beta(s, m^2)} + i0^+ \right) + \frac{2}{s} \left(\tilde{B}(s, m^2) + 2 \right), \\ \tilde{C}_1(s_1, s_2, m^2) &\equiv \frac{1}{2} \frac{1}{s_1 - s_2} \left[\log^2 \left(-\frac{1 - \beta(s_1, m^2)}{1 + \beta(s_2, m^2)} + i0^+ \right) - \log^2 \left(-\frac{1 - \beta(s_2, m^2)}{1 + \beta(s_2, m^2)} + i0^+ \right) \right], \end{aligned}$$

with $\beta(s, m^2) \equiv \sqrt{1 - \frac{4m^2}{s}}$.

(5.28)

All other helicity amplitudes are either related via charge conjugation (5.19), or by relabeling of the external momenta

$$\mathcal{M}_{ggg \rightarrow H}^{+--} = \mathcal{M}_{ggg \rightarrow H}^{-++} \Big|_{p_1 \leftrightarrow p_2}, \quad \mathcal{M}_{ggg \rightarrow H}^{++-} = \mathcal{M}_{ggg \rightarrow H}^{--+} \Big|_{p_1 \leftrightarrow p_3}. \quad (5.29)$$

Note that the Mandelstam variables are defined in terms of incoming gluon momenta, i.e.

$$s = (p_1 + p_2)^2, \quad t = (p_1 + p_3)^2, \quad u = (p_2 + p_3)^2. \quad (5.30)$$

³ The functions are closely related to the finite part of the bubble integrals, and the triangle integrals with on-shell, and one off-shell leg. The functions are modified slightly to simplify the expressions, however we keep the standard notation, where B functions indicate bubbles and C functions triangle integrals. The tilde is added to make the distinction from the original integrals more apparent.

For the quark channel the result reads

$$\mathcal{M}_{\bar{q}qg \rightarrow H}^{(1),-++} \Big|_{2 \text{ masses}} = \frac{1}{\sqrt{2}} \frac{[13]^2}{[12]} \frac{4}{9(t+u)} \left(5s + 12m_t^2 + (3s + 6m_t^2) \tilde{B}(s, m_t^2) \right) \left[\tilde{B}(m_H^2, m_b^2) + \frac{t+u}{s} + 2 \frac{m_b^2}{s} (4m_b^2 - t - u) \tilde{C}_1(s, m_H^2, m_b^2) - \frac{4m_b^2}{t+u} \tilde{B}(s, m_b^2) \right]. \quad (5.31)$$

Once again all other amplitudes can be obtained through a relabeling of the external momenta and charge conjugation. We see that the functional dependence on the Mandelstams is identical in all amplitudes in Eqs. (5.26), (5.27), and (5.31). This is because the expression is related to the off-shell gluon-Higgs form factor, appearing in all Feynman diagrams of this contribution (see Fig. 5.3).

Contributions With One Heavy Quark

For completeness, we also reproduce the LO helicity amplitudes computed in Ref. [163].

$$\begin{aligned} \mathcal{M}_{ggg \rightarrow H}^{(0),+++} = & \frac{1}{\sqrt{2}} \frac{16m^2 stu}{\langle 12 \rangle \langle 23 \rangle \langle 31 \rangle} \left\{ -8 \left[\frac{1}{ut} + \frac{1}{tt_1} + \frac{1}{uu_1} \right] - \frac{8}{s} \left[\frac{2s+t}{u_1^2} B_1(u) + \frac{2s+u}{t_1^2} B_1(t) \right] \right. \\ & - \frac{2(s-4m^2)}{stu} [s_1 C_1(s) + (u-s)C_1(t) + (t-s)C_1(u)] - 16m^2 \left[\frac{1}{tt_1} C_1(t) + \frac{1}{uu_1} C_1(u) \right] \\ & \left. + \frac{8m^2}{s} D(u, t) + \frac{s-4m^2}{stu} [stD(s, t) + usD(u, s) - utD(u, t)] - \frac{4}{s^2} E(u, t) \right\} \end{aligned} \quad (5.32)$$

$$\begin{aligned} \mathcal{M}_{ggg \rightarrow H}^{(0),-++} = & \frac{1}{\sqrt{2}} \frac{[23]^3}{[12][13]} \frac{16m^2 st}{u} \left\{ \frac{8m_H^2}{stu} + \frac{2(m_H^2 - 4m^2)}{stu} [s_1 C_1(s) + u_1 C_1(u) + t_1 C_1(t)] \right. \\ & \left. - \frac{m_H^2 - 4m^2}{stu} [stD(s, t) + usD(u, s) + utD(u, t)] \right\} \end{aligned} \quad (5.33)$$

$$\mathcal{M}_{\bar{q}q \rightarrow H}^{(0),-++} = \frac{1}{\sqrt{2}} \frac{[13]^2}{[12]} \frac{m^2}{s_1} \left[2 + 2 \frac{s}{s_1} B_1(s) + (4m^2 - u - t) C_1(s) \right] \quad (5.34)$$

Here m is the internal quark mass and we defined

$$s_1 = s - m_H^2, \quad t_1 = t - m_H^2, \quad u_1 = u - m_H^2. \quad (5.35)$$

The appearing functions are directly linked to standard Feynman integrals which we provide in Appendix B. **TODO: Check numerically**

Although there is one less scale in the contributions with only one quark mass, the two-loop amplitudes are a lot more complex because the integrals do no longer factorize. Instead of attempting to solve the remaining integrals analytically, we followed a numerical approach, where the amplitudes are evaluated at fixed phase-space points. These points can then be used as grid points for interpolations during the phase-space integration. For the numerical evaluation of the master integrals we follow the strategy outlined in Ref. [122], which itself is based on methods presented in Ref. [164]. The general idea is to derive a system of differential equation for each integral family, find suitable boundary conditions analytically, and then solve the differential equations numerically.

The amplitude is a function of four variables, e.g. s, t, u and the quark mass m . The Higgs mass is not a free parameter since it can be expressed as a sum over the Mandelstams. We can

however simply factor our one scale, say the collision scale s to make everything dimensionless, and we are left with only three. We choose to parametrize the amplitude in terms of the dimensionless variables

$$z \equiv -\frac{t+u}{s}, \quad \lambda \equiv \frac{t}{t+u}, \quad x \equiv \frac{m^2}{s} = \frac{m^2}{m_H^2}(1-z). \quad (5.36)$$

These variables are advantageous because they parametrize soft and collinear limits. Indeed, soft limits are described with $z \rightarrow 0$, whereas the collinear limits are captured by $\lambda \rightarrow 0$ for the t -collinear and $\lambda \rightarrow 1$ for u -collinear. Furthermore, z and λ are bounded by

$$0 \leq z \leq 1, \quad 0 \leq \lambda \leq 1, \quad \text{and} \quad 0 \leq x \quad (5.37)$$

for physical production kinematics.

To apply the method of differential equations, we need to apply derivatives with respect to our variables, but the master integrals are functions of the external momenta. We can apply the chain rule to relate the derivatives

$$\begin{aligned} \left(z \frac{\partial}{\partial z} \right) &= \left(t \frac{\partial}{\partial t} \right) + \left(u \frac{\partial}{\partial u} \right) + \frac{t+u}{s+t+u} \left(x \frac{\partial}{\partial x} \right) \\ &= \left(p_3^\mu \frac{\partial}{\partial p_3^\mu} \right) - \frac{z}{1-z} \left(x \frac{\partial}{\partial x} \right), \end{aligned} \quad (5.38)$$

$$\begin{aligned} \left(\lambda \frac{\partial}{\partial \lambda} \right) &= \left(t \frac{\partial}{\partial t} \right) - \frac{\lambda}{1-\lambda} \left(u \frac{\partial}{\partial u} \right) \\ &= \frac{1}{2} \left(\left(p_1^\mu \frac{\partial}{\partial p_1^\mu} \right) - \left(p_2^\mu \frac{\partial}{\partial p_2^\mu} \right) + (1-2\lambda) \left(p_3^\mu \frac{\partial}{\partial p_3^\mu} \right) \right). \end{aligned} \quad (5.39)$$

The derivative with respect to x remains unchanged. One can now proceed to apply the differential operators onto the master integrals. The derivatives result in new integrals, which we can relate to our master integrals through the repeated use of IBPs.

We found that it is advantageous shift almost all the appearing master integrals from $d = 4 - 2\epsilon$ to $d + 2$ dimensions, by application of *dimension-shift relations* (see Ref. [6] for a comprehensive introduction). This way, all spurious poles of the top-level sector are removed, and the integrals must only be computed up to ϵ^0 . As a byproduct, we found that the coefficients in front of the master integrals are significantly reduced in complexity.

In order to solve the differential equation, we need to find suitable boundary conditions. Since the HTL has already been extensively studied, it suggests itself to use it as boundary conditions. To this end, we expand the integrals in the limit of a large internal mass m , $x \rightarrow \infty$ by means of the *large mass expansion* (see Ref. [165] for a comprehensive introduction). It allows expanding integrals in the limit of large masses already at the integral level, i.e. the remaining integrals are devoid of the large mass. The expansion is implemented in the workflow of **DiaGen/IdSolver**. The only required integrals are massless four-point functions and vacuum integrals which can be found in the appendix of Ref. [166].

The solutions found at the boundary $x \rightarrow \infty$ can now be transported to the physical plane, i.e. to finite quark masses by solving the differential equation in the x -direction. This strategy is illustrated in Fig. 5.8. The differential equation is solved numerically using the *Bulirsch-Stoer algorithm*. Since we are working within the physical parameter space defined by Eq. (5.36), we can no longer relate the various matrix elements by means of crossing relations Eq. (5.29). We

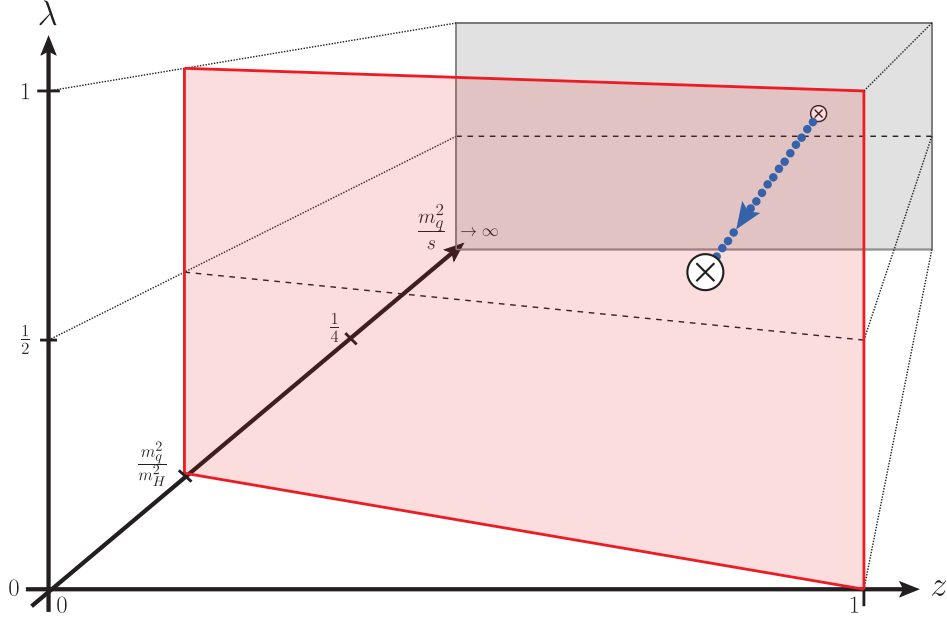


Figure 5.8: Graphical illustration of the parameter space and the strategy for transporting the boundary conditions at $x \rightarrow \infty$ to the physical plane shown in red. Figure taken (with slight modification) from Ref. [166].

will therefore have to switch to a physical momentum configuration and compute all matrix elements⁴

$$\begin{aligned} &\mathcal{M}_{gg \rightarrow Hg}^{+++}, \mathcal{M}_{gg \rightarrow gH}^{--+}, \mathcal{M}_{gg \rightarrow gH}^{+-+}, \mathcal{M}_{gg \rightarrow gH}^{++-}, \mathcal{M}_{gg \rightarrow gH}^{+++}, \\ &\mathcal{M}_{\bar{q}q \rightarrow gH}^{++-}, \mathcal{M}_{\bar{q}q \rightarrow gH}^{+-+}, \mathcal{M}_{g\bar{q} \rightarrow \bar{q}H}^{++-}, \mathcal{M}_{g\bar{q} \rightarrow \bar{q}H}^{+-+}, \mathcal{M}_{qg \rightarrow qH}^{++-}, \mathcal{M}_{qg \rightarrow qH}^{+-+} \end{aligned} \quad (5.40)$$

individually. Notice that we can still apply the charge conjugation identity in Eq. (5.19) if we first pull out the spinor-helicity factors. Nevertheless, the exchange of the first two momenta does not take us out of the physical parameter space and hence the crossing symmetry (followed by charge conjugation) can still be exploited.

$$|\mathcal{M}_{gg \rightarrow gH}^{\lambda_1 \lambda_2 \lambda_3}|^2(\lambda, z, x) = |\mathcal{M}_{gg \rightarrow gH}^{\lambda_2 \lambda_1 \lambda_3}|^2(1 - \lambda, z, x), \quad (5.41)$$

$$|\mathcal{M}_{\bar{q}q \rightarrow gH}^{\lambda_1 \lambda_2 \lambda_3}|^2(\lambda, z, x) = |\mathcal{M}_{\bar{q}q \rightarrow gH}^{\lambda_2 \lambda_1 \lambda_3}|^2(1 - \lambda, z, x), \quad (5.42)$$

$$|\mathcal{M}_{qg \rightarrow qH}^{\lambda_1 \lambda_2 \lambda_3}|^2(\lambda, z, x) = |\mathcal{M}_{qg \rightarrow qH}^{\lambda_2 \lambda_1 \lambda_3}|^2(1 - \lambda, z, x). \quad (5.43)$$

We relate the squared amplitudes to avoid phase factors arising from the spinor-helicity factors. The physical parameter space is therefore effectively cut in half. Consequently, we only have to solve the amplitude for $1/2 \leq \lambda \leq 1$ and can infer the remaining space with these symmetry relations.

We therefore choose initial conditions which are just above the symmetry line $\lambda = 1/2$, and then sample different values in z . The solutions of the differential equation in x for these samples then serve as initial conditions for the differential equation in λ . This is illustrated in Fig. 5.9. At $z \rightarrow 0$, we encounter a soft divergence. These divergences will cancel in the end, but it is therefore important to map out this parameter space with particular care. We therefore sample z logarithmically. Furthermore, for $z \rightarrow 1$ the poles of the differential equation

⁴ The helicities are assigned to the partons in the order they appear in the corresponding process, i.e. the first helicity belongs to the first appearing parton, the second to the second, and the third to the third.

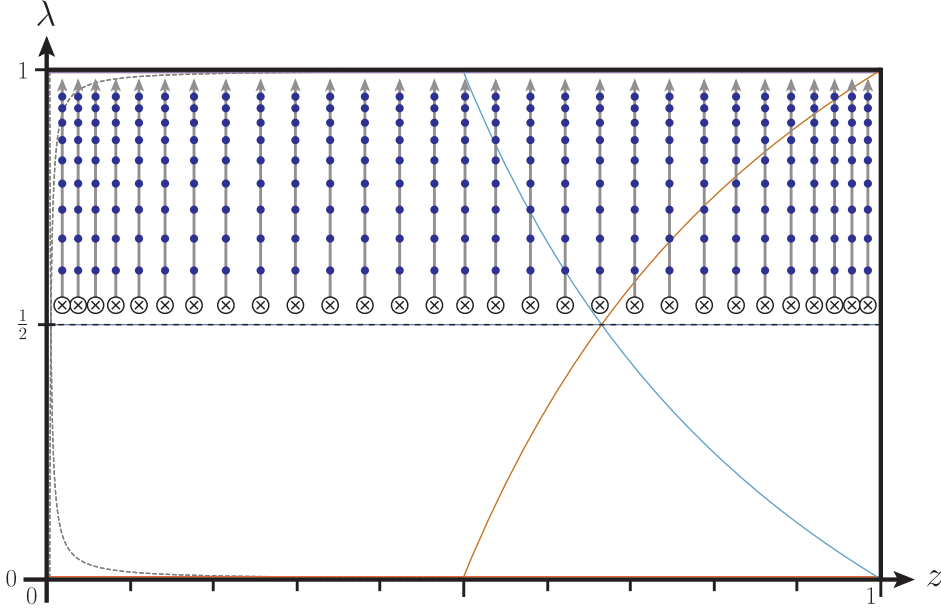


Figure 5.9: Illustration of the physical plane (shown in red in Fig. 5.8) for a bottom quark with a mass ratio of $m_b^2/m_H^2 = 1/684$. The colored thin lines indicate poles of the differential equation in λ . The circled crosses with the errors indicate the boundary condition for the differential equation in λ and the path along which the differential equation is solved. The integration paths are not to scale and are for illustrative purposes only.

are very close together. This once again causes large cancellations. To avoid mismodelling the amplitudes in these regions of the parameter space we therefore also sample more points close to this boundary. In the end we sample around 1000 values of z , ranging from 10^{-4} to $1 - 10^{-4}$.

The poles of the differential equation in λ are dealt with via a contour deformation in the complex plane. Once again we sample λ logarithmically, such that we obtain more points towards the IR-sensitive $\lambda \rightarrow 1$ region. In total, we sample around 500 points, yielding dense grid of the physical plane of around 10^6 grid points.

Around the IR sensitive regions $z \rightarrow 0$ and $\lambda \rightarrow 0, 1$, the amplitudes are dominated by the singularities $1/z$ and $1/\sqrt{\lambda}$, a contribution which will eventually cancel against other IR divergences. On the other hand, the dominance of the singularity will negatively impact the precision of the interpolation for the non-divergent terms. We would therefore like to subtract the IR-divergences before performing the interpolation. It is well known, that the leading IR behavior factorizes from the amplitude. Consider for example, the limit of two almost collinear outgoing partons with momenta

$$p_1^\mu = z_1 p^\mu + k_\perp^\mu - \frac{k_\perp^2}{z_1} \frac{n^\mu}{2p \cdot n}, \quad p_2^\mu = (1 - z_1) p^\mu - k_\perp^\mu - \frac{k_\perp^2}{1 - z_1} \frac{n^\mu}{2p \cdot n}, \quad (5.44)$$

where $k_\perp \cdot p = k_\perp \cdot n = 0$, and p and n are on-shell ($p^2 = n^2 = 0$). Further p and n are not collinear, i.e. $p \cdot n \sim \mathcal{O}(p^0 n^0)$. The collinear limit is therefore parametrized by $k_\perp \rightarrow 0$. Then the leading power behavior of the one-loop averaged squared matrix element is given by

$$\begin{aligned} & \overline{2\text{Re}\langle \mathcal{M}_{a_1 a_2, \dots}^{(0)}(p_1, p_2, \dots) | \mathcal{M}_{a_1 a_2, \dots}^{(1)}(p_1, p_2, \dots) \rangle} \simeq \\ & 4\pi\alpha_s \frac{1}{p_1 \cdot p_2} \left[\langle P_{a_1 a_2}^{(0)}(z_1) \rangle \times \overline{2\text{Re}\langle \mathcal{M}_{a, \dots}^{(0)}(p, \dots) | \mathcal{M}_{a, \dots}^{(1)}(p, \dots) \rangle} \right. \\ & \quad \left. + \frac{\alpha_s}{4\pi} \langle P_{a_1 a_2}^{(1)}(z_1) \rangle \overline{\langle \mathcal{M}_{a, \dots}^{(0)}(p, \dots) | \mathcal{M}_{a, \dots}^{(0)}(p, \dots) \rangle} \right]. \end{aligned} \quad (5.45)$$

Here a_1 and a_2 denote the flavor of the respective parton, while the flavor a is set by flavor conservation. $\langle P_{a_1 a_2}^{(0,1)}(z_1) \rangle$ are the tree-level and one-loop averaged splitting functions. For reasons that will be explained below, the exact structure of the one-loop splitting functions is of no concern to us. The tree-level averaged splitting functions in four dimensions read

$$\begin{aligned} \langle P_{gg}^{(0)}(z_1) \rangle &= 2C_A \left(\frac{z_1}{1-z_1} + \frac{1-z_1}{z_1} + z_1(1-z_1) \right), \\ \langle P_{q\bar{q}}^{(0)}(z_1) \rangle &= \langle P_{\bar{q}q}^{(0)}(z_1) \rangle = T_F (1 - 2z_1(1-z_1)), \\ \langle P_{qg}^{(0)}(z_1) \rangle &= \langle P_{\bar{q}g}^{(0)}(z_1) \rangle = C_F \frac{1+z_1^2}{1-z_1} \\ \langle P_{gq}^{(0)}(z_1) \rangle &= \langle P_{g\bar{q}}^{(0)}(z) \rangle = \langle P_{qg}^{(0)}(1-z) \rangle. \end{aligned} \quad (5.46)$$

Initial state collinear divergences can be recovered by replacing $p_2 \rightarrow -p_2$ as well as $P_{a_1 a_2} \rightarrow (-1)^{2s_a + 2s_{a_1}} P_{a_1 a_2}$, where s_a and s_{a_1} are the spins of the respective partons.

Likewise, in the limit where one of the external gluons becomes soft, $q \rightarrow 0$, the factorization of the one-loop squared amplitude with external partons reads

$$\begin{aligned} & 2\text{Re}\langle \mathcal{M}_{g, a_1, \dots}^{(0)}(q, p_1, \dots) | \mathcal{M}_{g, a_1, \dots}^{(1)}(q, p_1, \dots) \rangle \simeq \\ & -4\pi\alpha_s \left\{ \sum_{(i,j)} (\mathcal{S}_{ij}(q) - \mathcal{S}_{ii}(q)) 2\text{Re}\langle \mathcal{M}_{a_1, \dots}^{(0)}(p_1, \dots) | \mathbf{T}_i \cdot \mathbf{T}_j | \mathcal{M}_{a_1, \dots}^{(1)}(p_1, \dots) \rangle \right. \\ & \quad + \frac{\alpha_s}{4\pi} \left[\sum_{(i,j)} (\mathcal{S}_{ij}(q) - \mathcal{S}_{ii}(q)) R_{ij} \langle \mathcal{M}_{a_1, \dots}^{(0)}(p_1, \dots) | \mathbf{T}_i \cdot \mathbf{T}_j | \mathcal{M}_{a_1, \dots}^{(0)}(p_1, \dots) \rangle \right. \\ & \quad \left. \left. - 4\pi \sum_{(i,j,k)} \mathcal{S}_{ik}(q) I_{ij} \langle \mathcal{M}_{a_1, \dots}^{(0)}(p_1, \dots) | f^{abc} \mathbf{T}_i^a \mathbf{T}_j^b \mathbf{T}_k^c | \mathcal{M}_{a_1, \dots}^{(1)}(p_1, \dots) \rangle \right] \right\} \end{aligned} \quad (5.47)$$

The sums run over distinct parton indices. \mathbf{T}_i denotes the color operator of the i -th particle, i.e. it is the generator of the SU(3) group in the representation of that particle: fundamental for quarks, complex-conjugated for anti-quarks, adjoint for gluons and trivial for colorless particles. Once again, the exact structure of the one-loop coefficients I_{ij} , R_{ij} is irrelevant to us (see Ref. [164] for a definition). The eikonal factor is given by

$$\mathcal{S}_{ij}(q) = \frac{p_i \cdot p_j}{(p_i \cdot q)(p_j \cdot q)}. \quad (5.48)$$

We claim that the regulated averaged squared amplitudes⁵

$$\begin{aligned}
\overline{\langle \mathcal{M}_{gg \rightarrow gH}^{(0)} | \mathcal{M}_{gg \rightarrow gH}^{(1)} \rangle}_{\text{regulated}} &\equiv \overline{\langle \mathcal{M}_{gg \rightarrow gH}^{(0)} | \mathcal{M}_{gg \rightarrow gH}^{(1)} \rangle} - \overline{\langle \mathcal{M}_{gg \rightarrow gH}^{(0),\text{rHTL}} | \mathcal{M}_{gg \rightarrow gH}^{(1),\text{rHTL}} \rangle} \\
&- \overline{\langle \mathcal{M}_{gg \rightarrow H}^{(0)} | \mathcal{M}_{gg \rightarrow H}^{(1)} - \mathcal{M}_{gg \rightarrow H}^{(1),\text{rHTL}} \rangle} \times \begin{cases} \frac{8\pi\alpha_s}{t} \langle P_{gg}^{(0)} \left(\frac{s}{s+u} \right) \rangle & \text{if } |t| < |u| \\ \frac{8\pi\alpha_s}{u} \langle P_{gg}^{(0)} \left(\frac{s}{s+t} \right) \rangle & \text{if } |u| < |t| \end{cases}, \\
\overline{\langle \mathcal{M}_{qg \rightarrow qH}^{(0)} | \mathcal{M}_{qg \rightarrow qH}^{(1)} \rangle}_{\text{regulated}} &\equiv \overline{\langle \mathcal{M}_{qg \rightarrow qH}^{(0)} | \mathcal{M}_{qg \rightarrow qH}^{(1)} \rangle} - \overline{\langle \mathcal{M}_{qg \rightarrow qH}^{(0),\text{rHTL}} | \mathcal{M}_{qg \rightarrow qH}^{(1),\text{rHTL}} \rangle} \\
&+ \overline{\langle \mathcal{M}_{gg \rightarrow H}^{(0)} | \mathcal{M}_{gg \rightarrow H}^{(1)} - \mathcal{M}_{gg \rightarrow H}^{(1),\text{rHTL}} \rangle} \times \frac{8\pi\alpha_s}{t} \langle P_{q\bar{q}}^{(0)} \left(\frac{s}{s+u} \right) \rangle, \\
\overline{\langle \mathcal{M}_{q\bar{q} \rightarrow gH}^{(0)} | \mathcal{M}_{q\bar{q} \rightarrow gH}^{(1)} \rangle}_{\text{regulated}} &\equiv \overline{\langle \mathcal{M}_{q\bar{q} \rightarrow gH}^{(0)} | \mathcal{M}_{q\bar{q} \rightarrow gH}^{(1)} \rangle} - \overline{\langle \mathcal{M}_{q\bar{q} \rightarrow gH}^{(0),\text{rHTL}} | \mathcal{M}_{q\bar{q} \rightarrow gH}^{(1),\text{rHTL}} \rangle},
\end{aligned} \tag{5.49}$$

are free of IR divergences. The averaged splitting functions are

$$\langle P_{gg}^{(0)}(z) \rangle = 2C_A \left(\frac{z}{1-z} + \frac{1-z}{z} + z(1-z) \right) \quad \text{and} \quad \langle P_{q\bar{q}}^{(0)}(z) \rangle = T_F (1 - 2z(1-z)). \tag{5.50}$$

By subtracting the amplitude in the rHTL we are eliminating all infrared divergences coming from one-loop splitting functions or soft functions in Eqs. (5.45) and (5.47). These functions only act upon the difference of the LO Higgs-gluon form factor in QCD and in the rHTL. But this difference is zero by definition of the rHTL. Notice that the factor used for rescaling the cross section in the HTL for the interference contributions is now defined in terms of

$$r_{t \times b}^{\text{LO}} = \frac{\hat{\sigma}_{t \times b}^{\text{LO}}}{\hat{\sigma}_{t \times b}^{\text{LO,rHTL}}}, \tag{5.51}$$

which for on-shell masses yields approximately -0.129 . In contrast to the rescaling factor for the pure top-quark contribution, this rescaling factor has no direct phenomenological relevance, in the sense that it can incorporate finite quark mass effects, and is used only as a computational trick.

After subtraction of the rHTL squared amplitudes, the difference still exhibits divergences from tree-level splitting and soft functions. For the $gg \rightarrow gH$ amplitude the divergence can be handled by subtracting

$$\overline{\langle \mathcal{M}_{gg \rightarrow H}^{(0)} | \mathcal{M}_{gg \rightarrow H}^{(1)} - \mathcal{M}_{gg \rightarrow H}^{(1),\text{rHTL}} \rangle} \times \begin{cases} \frac{8\pi\alpha_s}{t} \langle P_{gg}^{(0)} \left(\frac{s}{s+u} \right) \rangle & \text{if } |t| < |u| \\ \frac{8\pi\alpha_s}{u} \langle P_{gg}^{(0)} \left(\frac{s}{s+t} \right) \rangle & \text{if } |u| < |t| \end{cases} \tag{5.52}$$

from the difference. To see this, let us first consider the t -collinear limit, i.e. $p_1 \cdot p_3 \rightarrow 0$. We can choose the anti-collinear direction to be along p_2 and then determine⁶

$$z_1 = \frac{p_1 \cdot p_2}{p_1 \cdot p_2 - p_3 \cdot p_2} = \frac{s}{s-u}. \tag{5.53}$$

Hence, Eq. (5.52) has exactly the structure required from a collinear limit (5.45). The u -collinear limit works analogously. The soft limit, where t and u tend to zero, we can expand the splitting functions and get

$$(5.52) \rightarrow \overline{\langle \mathcal{M}_{gg \rightarrow H}^{(0)} | \mathcal{M}_{gg \rightarrow H}^{(1)} - \mathcal{M}_{gg \rightarrow H}^{(1),\text{rHTL}} \rangle} \times \frac{8\pi\alpha_s}{t} 2C_A \frac{s}{u}. \tag{5.54}$$

⁵ **TODO:** Notice the different signs in front of the splitting functions compared to Ref. [4].

⁶ Note that z is only unique up to power corrections.

Remembering that the Higgs-gluon form factor was diagonal in color-space, i.e. proportional to $\delta^{c_1 c_2}$, we see that this is exactly the soft divergence predicted by Eq. (5.47).

Lacking a final state gluon, the qg -channel can not develop a soft divergence. The initial state collinear divergence is subtracted with the corresponding splitting functions analogous to the gg channel. The different sign comes from the splitting function, which generates a minus sign if a fermion is crossed to the initial state.

Lastly, after subtraction of the squared amplitude of the rHTL the $q\bar{q}$ -channel does not exhibit any IR singularity, due to the lack of available Born processes.

In Fig. 5.10 we present the results for the top-bottom interference contribution to the amplitudes, while Fig. 5.11 shows the results for the pure-top-quark contribution. Despite having subtracted

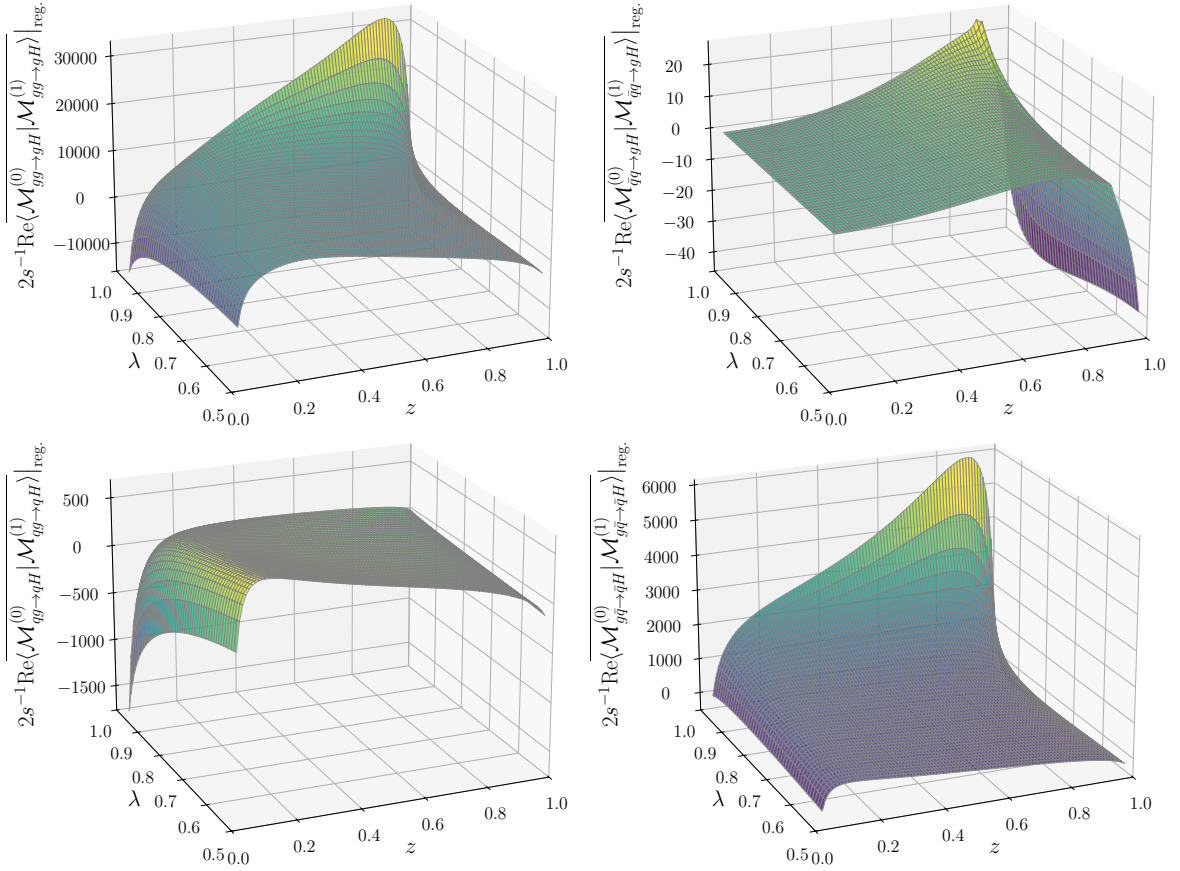


Figure 5.10: Top-bottom interference contribution to the amplitudes $gg \rightarrow gH$ (top left), $\bar{q}q \rightarrow gH$ (top right), $qg \rightarrow qH$ (bottom left) and $g\bar{q} \rightarrow \bar{q}H$ (bottom right) normalized by the partonic center of mass energy s . Displayed is only half of the parameter space $\lambda \in [0.5, 1]$; the other half can be obtained by means of the symmetry relations in Eqs. (5.41), (5.42) and (5.43). For better visibility we only show grid points in the range of $\lambda \in [0.5, 0.98]$ and $z \in [0.02, 0.98]$. The amplitude is computed with on-shell renormalized quark-masses. The computational setup is described in the conventions.

the IR-divergences, the amplitudes still have some residual divergences in the IR-sensitive regions close to $z \rightarrow 0$ and $\lambda \rightarrow 1$. These divergences are however much better behaved, only showing logarithmic growth at the edges of the phase-space, and consequently can be integrated over. As expected, $\bar{q}q$ -channel does not show logarithmic divergences in the soft limit

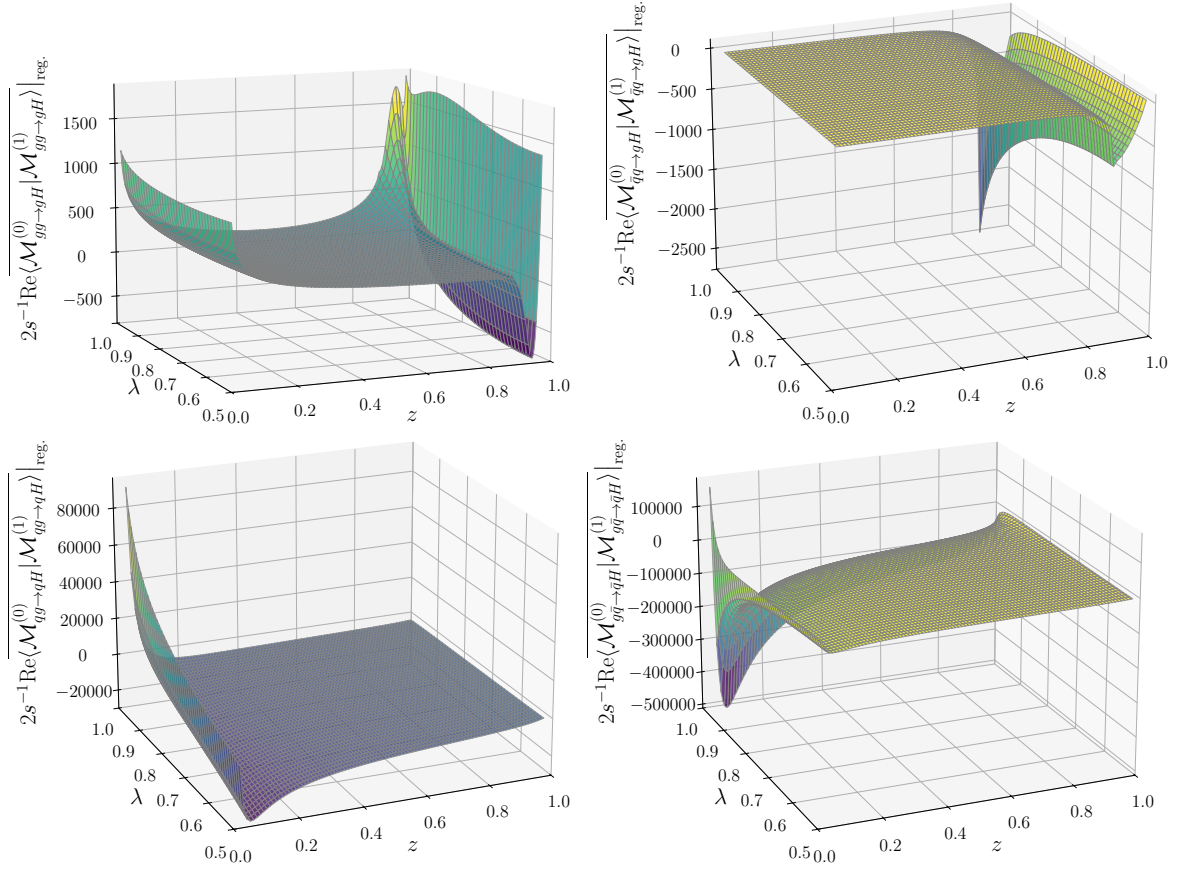


Figure 5.11: Same as in Fig. 5.10 but for the pure-top-quark contribution to the amplitudes. Plot range for the $gg \rightarrow gH$ has been changed to $z \in [0.002, 0.965]$ and $\lambda \in [0.5, 0.98]$, for better visibility.

$z \rightarrow 0$, since the $\bar{q}q \rightarrow H$ process was forbidden by the conservation of angular momentum (see discussion around Eq. (4.69)).

In the pure-top-quark contribution, the $gg \rightarrow gH$ and $\bar{q}q \rightarrow gH$ amplitudes display their most prominent features around the $t\bar{t}$ -production threshold at $z_{\text{threshold}} = 1 - \frac{m_H^2}{4m_t^2} \approx 0.87$. This aligns with our expectations, as Landau's equations predict the amplitudes to have a branch cut starting from the production threshold. The amplitudes for the $q\bar{q} \rightarrow qH$ and $g\bar{q} \rightarrow \bar{q}H$ processes do not exhibit this branch cut, since here the discontinuity lies outside the physical parameter space. For the top-bottom interference contributions, the threshold region is not as feature rich, since the amplitudes with top-quark induced Higgs production are no longer squared, but instead multiplied by the bottom-quark induced Higgs production, which do not have branch cuts at the $t\bar{t}$ -thresholds.

Interpolation

During the phase-space integration, we require the amplitude at any value of the parameter space not just at the grid points we computed. We can get a very accurate approximation of the amplitudes by interpolating between the grid point. To do this, we first identify a 4×4 sub-grid, such that the target point lies inside the center square. We then construct cubic splines in one-dimension, say in the λ -direction using the respective grid points for fixed values of z . We can then use these spline fits to obtain approximations of the amplitude at the target- λ value and the four fixed z -values. Afterwards, we simply use these four values

to construct another cubic spline fit in the z -direction, which can then be used to get an approximation of the amplitude at the target phase-space point. The method is illustrated in Fig. 5.12 and can be straightforwardly generalized to any dimension. It should also be noted

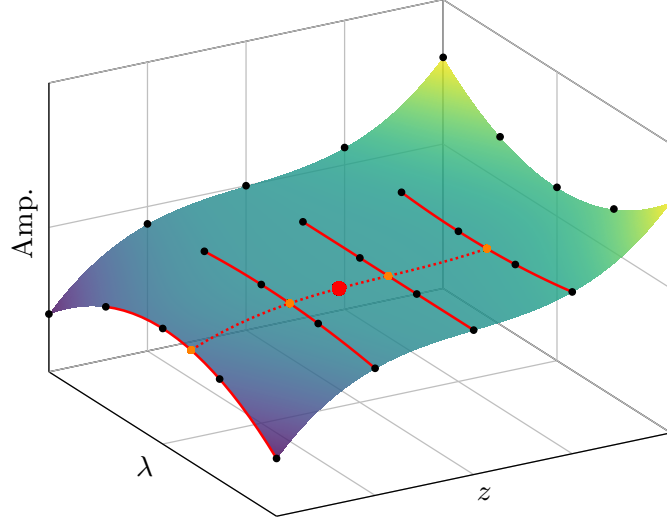


Figure 5.12: Graphical illustration of the method to perform multidimensional interpolations using cubic splines. The surface represents the actual amplitude; the black dots mark the computed grid points; the large red dot is the target phase-space point; the solid red line indicates the spline fit in the λ -direction; the orange dots mark the value of the λ -fits at the target- λ ; the dashed red line marks the spline fit in the z -direction.

that the method does not rely on a rectangularly distributed grid samples, but just requires them to be distributed in a straight line along one direction. This is important, as our grid samples were distributed logarithmically. Furthermore, grid points which are located very close to poles of the differential equation are not being evaluated due to the contour deformation. Since the interpolation method does not require equidistant grid points we can simply ignore these points and interpolate these regions of the phase-space.

During the phase-space integration we will also encounter phase-space regions which lie outside our computed grid, making it necessary for us to extrapolate. In the infrared sensitive regions the amplitude must grow double-logarithmically, whereas in the high-energy limit $z \rightarrow 1$ it can be shown [167, 120] that the amplitude grows as $\log^3(1 - z)$. One can therefore use a power-logarithmic *Ansatz* for the extrapolation of the amplitude. We found however, that extrapolations using the cubic splines yielded results compatible within the MC uncertainties, which is why we went with this simpler approach for our final result. The alternative extrapolation method serves as additional cross-check of the accuracy of our amplitudes in these regions of phase space.

After the interpolation, we add back the subtraction terms of Eq. (5.49), which we know fully analytically for the entire phase-space, to obtain the full amplitudes.

5.1.3 The Virtual-Virtual Corrections

Lastly, we consider virtual-virtual corrections to the $gg \rightarrow H$ amplitudes, that is the three-loop Higgs-gluon form factor. We can decompose the NNLO contribution to the form factor according to the quark loops of the respective Feynman diagrams as follows:

$$\begin{aligned} \mathcal{C}^{(2)} = & n_t \mathcal{C}_t^{(2)} + n_t^2 \mathcal{C}_{tt}^{(2)} + n_t n_l \mathcal{C}_{tl}^{(l)} \\ & + n_b \mathcal{C}_b^{(2)} + n_b^2 \mathcal{C}_{bb}^{(2)} + n_b n_l \mathcal{C}_{bl}^{(2)} \\ & + n_t n_b \left(\mathcal{C}_{tb}^{(2)} + \mathcal{C}_{bt}^{(2)} \right). \end{aligned} \quad (5.55)$$

The first index indicates which quark flavor couples to the Higgs, and the second index—if present—marks the flavor of the other quark loop. That means contributions inside $\mathcal{C}_t^{(2)}$ are computed from Feynman diagrams containing only a single quark-loop with a top-quark running inside. Example Feynman diagrams for this contribution are shown in Fig. 5.13. $\mathcal{C}_b^{(2)}$ is computed by the same means only with the top-quark replaced by the bottom quark. Similarly,

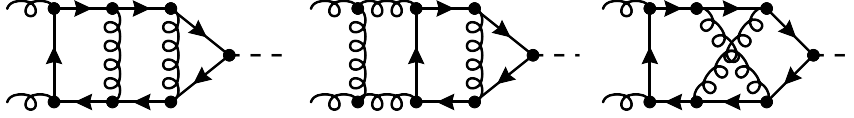


Figure 5.13: Example Feynman diagrams for contributions containing only a single heavy quark-loop.

$\mathcal{C}_{tt}^{(2)}$ then contains two closed top-quark loops, $\mathcal{C}_{tl}^{(2)}$ one top-quark and one light-quark loop, and so on. All Feynman diagrams containing two closed quark-loops are depicted in Fig. 5.14. The $\mathcal{C}_t^{(2)}$, $\mathcal{C}_{tt}^{(2)}$, $\mathcal{C}_{tl}^{(2)}$, $\mathcal{C}_b^{(2)}$, $\mathcal{C}_{bb}^{(2)}$ and $\mathcal{C}_{bl}^{(2)}$ contributions are computed with only a single heavy quark mass, making these contributions functions of only one dimensionless variable

$$z_q = \frac{m_H^2}{4m_q^2}. \quad (5.56)$$

The $\mathcal{C}_{tb}^{(2)}$ and $\mathcal{C}_{bt}^{(2)}$ parts of the form factor on the other hand are now functions of both z_b and z_t . They are the only instance, where we encounter non-factorizable Feynman-integrals with two-different masses in the whole cross section calculation. Note that when working in the 5FS, the $\mathcal{C}_{tb}^{(2)}$ contribution is set to zero, because the bottom quark loop is not coupling to the Higgs.

Both, the one and two quark mass contribution have been computed recently [43, 166]. They apply a method similar to what we have described in the previous chapter. They derive a set of differential equations, this time in terms z_q or z_b and z_t and subsequently solve the differential equation numerically. The heavy-top- and the high-energy limit are used as boundary conditions of the differential equation. The numerical samples are computed with very high precision and are then used by the authors to determine a deep asymptotic expansion in the large-mass, and the high-energy limit. For phenomenological application, both the bottom- and the top-quark mass are sufficiently far away from the threshold, that the asymptotic expansions approximate the amplitude without a relevant loss of precision. We therefore use the provided series expansions for our computations.

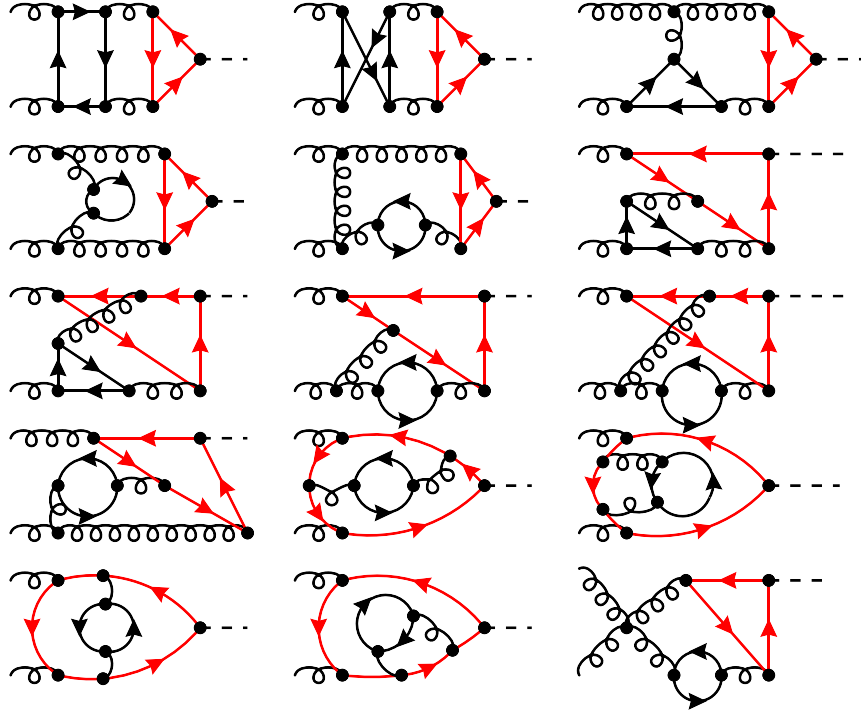


Figure 5.14: All Feynman diagrams with two closed quark loops. The quark loop coupling to Higgs, marked in red, must be a heavy quark line, i.e. either a top- or bottom- quark. The black quark loop can be either a top-, bottom- or light-quark. Reversed fermion flows are not explicitly drawn.

5.2 THE 4-FLAVOUR SCHEME

Up to this point, our discussion was mainly focused on the 5FS, where the bottom quark is considered to be a constituent of the proton. Consequently, to avoid the appearance of large logarithms, we have set the mass of the bottom-quark to zero, except in closed bottom-quark loops that couple to the Higgs. To assess the validity of this prescription, we want to investigate the alternative 4FS. Here the bottom-quark is consistently treated as a massive particle, and by excluding the quark from the initial state, the large IR-logarithms will cancel in sufficiently inclusive observables. In this section, we want to summarize the necessary adaptations of our calculation for the 4FS.

The Real-Real Corrections

In addition to the amplitudes already computed in the 5FS, the real-real corrections now include an additional channel, in which the Higgs is produced in association with a massive $b\bar{b}$ pair. Ergo, we need amplitudes for the processes $gg \rightarrow Hb\bar{b}$, and $q\bar{q} \rightarrow Hb\bar{b}$. The second and third diagram in Fig. 5.2 are examples of contributing Feynman diagrams. Note however, that we still require the Higgs to couple to a closed quark loop. Hence, a contribution like the one displayed in Fig. 5.15 are **not** considered in the present calculation. Instead, they are considered in the interference of the bottom-bottom fusion- and gluon-gluon fusion-channel and were evaluated in the 4FS a long time ago [168].

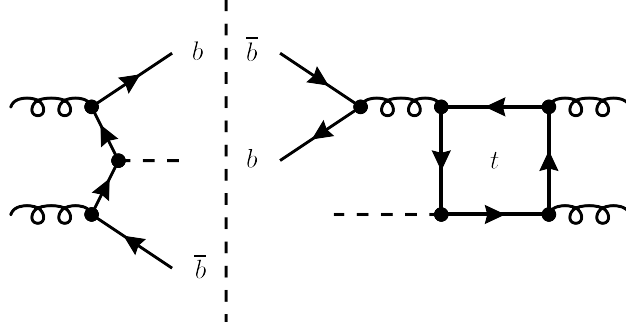


Figure 5.15: Example interference diagram for a contribution to the bottom-bottom fusion channel at NLO in the 4FS. Because the Higgs does not couple to a closed quark loop, it is not considered a contribution to gluon-gluon fusion, but to the gluon-gluon-fusion–bottom-bottom-fusion interference.

The additional amplitudes are evaluated using the public amplitude library **RECOLA** [147]. However, the exclusion of the bottom-bottom fusion channel is not supported by **RECOLA**, and requires some out-of-the-box thinking. Our approach works by computing the amplitudes in the two-Higgs-doublet model instead of the SM. The details of the model are irrelevant for our purposes, the only important aspect is that the model now contains a second Higgs boson H_2 . We switch off any coupling to lighter quarks, including the bottom quark. Hence, we can compute the top-quark induced Higgs production in association of a massive $\bar{b}b$ pair. But how can we now obtain the bottom-quark induced Higgs production? The solution is to couple the second Higgs boson and rescale the momenta and masses to match the SM, i.e. we choose the mass of the second Higgs boson as

$$m_{H_2} = \frac{m_t}{m_b} m_H, \quad (5.57)$$

and rescale all external momenta by

$$p_i^\mu \rightarrow \frac{m_t}{m_b} p_i^\mu. \quad (5.58)$$

This way the mass ratio of the Higgs boson, and the internal and external quark matches the SM ratio of m_H to m_b . Since the mass dimension of the amplitude (without the inclusion of the VEV) is vanishing, the global rescaling has no effect on the numerical result of the amplitude.

The Real-Virtual Corrections

Let us follow the notation from section 5.1.3 and introduce the bookkeeping parameters n_l , n_b and n_t to label light-, bottom-, and top-quark loops. The two-loop real-virtual amplitudes for the gluon-gluon fusion amplitudes then allow for the decomposition

$$\begin{aligned} \mathcal{M}_{ij \rightarrow kH}^{(1)} &= n_t \mathcal{M}_{ij \rightarrow kH}^{(1),t} + n_t^2 \mathcal{M}_{ij \rightarrow kH}^{(1),tt} + n_t n_l \mathcal{M}_{ij \rightarrow kH}^{(1),tl} \\ &\quad + n_b \mathcal{M}_{ij \rightarrow kH}^{(1),b} + n_b^2 \mathcal{M}_{ij \rightarrow kH}^{(1),bb} + n_b n_l \mathcal{M}_{ij \rightarrow kH}^{(1),bl} \\ &\quad + n_t n_b \left(\mathcal{M}_{ij \rightarrow kH}^{(1),tb} + \mathcal{M}_{ij \rightarrow kH}^{(1),bt} \right), \end{aligned} \quad (5.59)$$

where once again the first superscript indicates which quark flavor is coupling to the Higgs. In the 5FS both $\mathcal{M}_{ij \rightarrow kH}^{(1),tb}$ and $\mathcal{M}_{ij \rightarrow kH}^{(1),bt}$ were vanishing, the $\mathcal{M}_{ij \rightarrow kH}^{(1),bt}$ was computed analytically

while the rest was computed numerical. For the 4FS we can get the $\mathcal{M}_{ij \rightarrow kH}^{(1),tb}$ contribution from the $\mathcal{M}_{ij \rightarrow kH}^{(1),bt}$ upon exchanging the top and the bottom quark, i.e. by changing

$$m_t \longleftrightarrow m_b \quad (5.60)$$

in Eqs. (5.26), (5.27), and (5.31). For the remaining parts of the $2 \rightarrow 2$ amplitudes we compute the general amplitude in Eq. (5.59) while keeping track of the bookkeeping parameters, preserving maximal flexibility and allowing us to seamlessly change between FSs.

The Virtual-Virtual Corrections

Similarly, the 3-loop Higgs-gluon form factor is known as a deep asymptotic series with full parametric dependence on n_l , n_b and n_t . The only necessary changes to adapt the amplitude to the 4FS is to include the $\mathcal{C}_{bb}^{(2)}$ and $\mathcal{C}_{tb}^{(2)}$ terms previously omitted.

5.3 $\overline{\text{MS}}$ -SCHEME

So far, our discussion on amplitudes was limited to the on-shell renormalized quark masses. As explained in section 4.3.5, the top-bottom interference contribution is highly sensitive to the renormalization scheme, especially of the bottom quark. One of our central aims, was therefore to investigate the impact of the choice of the mass-renormalization scheme at NNLO. In this section, we want to discuss the relevant adjustments necessary for the computation of the $\overline{\text{MS}}$ -renormalized amplitudes.

Strictly speaking, $\overline{\text{MS}}$ -scheme is actually a collection of renormalization schemes, as every scale μ forms a new scheme. Since μ can be varied continuously, the RG-invariance can be leveraged in the form of the RGE

$$0 = \frac{d \ln m_q^B}{d \ln \mu} \Rightarrow \frac{d \ln m_q}{d \ln \mu} = -\frac{d \ln Z_m}{d \alpha_s} \pi \bar{\beta} = 2\alpha_s \frac{d Z_m^{(1)}}{d \alpha_s} \equiv -\gamma_m, \quad (5.61)$$

where $\bar{\beta}$ is again the d -dimensional β function of Eq. (4.44), $Z_m^{(1)}$ is the residue in the ϵ -expansion of the mass-renormalization constant, and γ_m is the *mass anomalous dimension*. The solution of the RGE is given by

$$m_q(\mu) = m_q(\mu_0) \exp \left[- \int_{\mu_0}^{\mu} \frac{d\mu'}{\mu'} \gamma_m(\mu') \right], \quad (5.62)$$

which truncated at one-loop yields

$$m_q(\mu) = m_q(\mu_0) \left(\frac{\alpha_s(\mu)}{\alpha_s(\mu_0)} \right)^{-\gamma_0/\beta_0}, \quad \text{where } \gamma_0 = 6C_F, \quad (5.63)$$

and β_0 as in Eq. (4.51). Beyond one-loop the differential equation becomes very challenging to solve analytically. We instead fall back to solving the differential equation numerically using the publically available software tool **CRunDec** [169], at the highest available 4-loop accuracy. Around the top-quark $\overline{\text{MS}}$ -mass, we observed that **CRunDec** encounters numerical instabilities, which we do not observe when using its **Mathematica** sister tool **RunDec** [170]. The Higgs production cross section is quite insensitive to the top-quark mass, hence we do not expect this to be of much importance. Especially considering, that in the total cross section the standard scale choice $\mu_R = m_H/2$ is below this instability region even for the

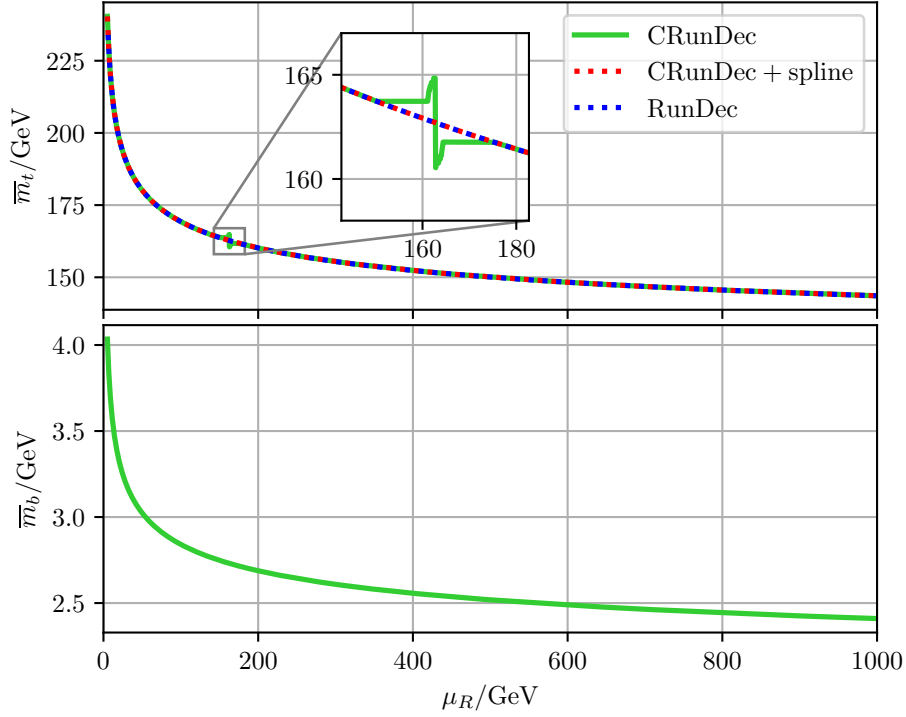


Figure 5.16: Running of the top- (top panel) and bottom-quark (bottom panel) mass. The solid green curve is the result computed with CRunDec at 4-loop accuracy. The dashed blue curve is the same but computed with RunDec [170]. The dashed red curve uses CRunDec except for the region $\mu_R \in [\bar{m}_t(\bar{m}_t) - 15 \text{ GeV}, \bar{m}_t(\bar{m}_t) + 15 \text{ GeV}]$, where we use a cubic spline instead. The computational setup is described in the conventions.

scale variation. Nevertheless, we will later also introduce dynamical scales which can exceed $\bar{m}_t(\bar{m}_t)$ for a large Higgs transverse momentum. For this reason, we bridge the problematic region around $\mu_R \in [\bar{m}_t(\bar{m}_t) - 15 \text{ GeV}, \bar{m}_t(\bar{m}_t) + 15 \text{ GeV}]$ using a cubic spline fit which we construct from the top-quark mass at $\bar{m}_t(\bar{m}_t) - 15 \text{ GeV}$, $\bar{m}_t(\bar{m}_t) - 14 \text{ GeV}$, $\bar{m}_t(\bar{m}_t) + 14 \text{ GeV}$, and $\bar{m}_t(\bar{m}_t) + 15 \text{ GeV}$. In Fig. 5.16, we can see that the spline fit correctly reproduces the results of RunDec in the unstable parameter window. The evolved quark masses then enter the computed amplitudes.

Since the real-virtual amplitudes containing only a single heavy quark flavor were computed using a fixed mass ratio m_q^2/m_H^2 (see section 5.1.2), we recompute the amplitude using a variety of different quark masses. In total, we computed the amplitude for nine different quark masses listed in Tab. 5.2. Using the interpolation method discussed in section 5.1.2, we are now able to very quickly compute all amplitudes with high precision in a large region of the parameter space. Note that the chosen grid masses have been selected explicitly to eliminate any interpolation error for the standard fixed scale choices, i.e. we only rely on the interpolation when using a dynamic scale. To assess the accuracy of our interpolation method, we individually removed all grid points corresponding to the masses $\bar{m}_b(m_H)$, $\bar{m}_b(m_H/2)$, $\bar{m}_b(m_H/4)$, m_t and reran the MC simulation. The results differed by less than the MC uncertainty, proofing the robustness of our interpolation method.

Grid mass	Value [GeV]	Approximate ratio $m_{b,t}^2/m_H^2$	Relative error [%]
m_b	4.78	$\frac{1}{684}$	0.2
$\overline{m}_b(m_H)$	2.789	$\frac{1}{2011}$	0.9
$\overline{m}_b(m_H/2)$	2.961	$\frac{1}{1782}$	0.2
$\overline{m}_b(m_H/4)$	3.170	$\frac{1}{1557}$	1.0
\overline{m}_b^{\min}	1.67	$\frac{1}{5602}$	0.1
m_t	172.4	$\frac{23}{12}$	4
$\overline{m}_t(m_H)$	166.1	$\frac{136}{77}$	0.0
$\overline{m}_t(m_H/2)$	176.2	$\frac{149}{75}$	0.0
$\overline{m}_t(m_H/4)$	188.2	$\frac{213}{94}$	0.0

Table 5.2: Mass ratios squared, m_b^2/m_H^2 and m_t^2/m_H^2 , used for the generation of numerical values of the two-loop four-point amplitudes. We chose values corresponding to the OS masses, according to PDG recommendations [171], and $\overline{\text{MS}}$ -masses at scales relevant for 7-point variation w.r.t. to a central scale of $m_H/2$. For the latter, we used $\overline{m}_b(\overline{m}_b) = 4.18$ GeV, as recommended by the PDG and $\overline{m}_t(\overline{m}_t) = 162.7$ GeV. The dynamic scale **TODO: Add reference of dynamic scale** used for our differential cross-section predictions can exceed m_H , and reaches values of up to 1 TeV. At this high scale, the bottom-quark mass is $\overline{m}_b(1 \text{ TeV}) = 2.41$ GeV. To avoid extrapolations outside our numerical grids for the amplitudes, we therefore included another mass value, \overline{m}_b^{\min} , below this minimum.

Evaluating on-shell renormalized amplitudes at the $\overline{\text{MS}}$ -mass does not make them $\overline{\text{MS}}$ -renormalized. We can however extract the $\overline{\text{MS}}$ -renormalized amplitudes by rewriting the OS-mass in terms of the $\overline{\text{MS}}$ -mass

$$m^{\text{OS}} = \overline{m}^{(n_m)}(\mu) \left(1 + c_1^{(n_m, n_l)}(\mu) \frac{\alpha_s^{(n_l)}(\mu)}{\pi} + c_2^{(n_m, n_l)}(\mu) \left(\frac{\alpha_s^{(n_l)}(\mu)}{\pi} \right)^2 + \mathcal{O}(\alpha^3) \right), \quad (5.64)$$

and then expand all amplitudes in α_s up to the required fix order. The superscripts n_m and n_l define which quark flavors have been decoupled from the mass and α_s . The relation between the quark masses in the different renormalization schemes can be extracted using the renormalization scheme invariance of the bare quark mass, which yields the relation

$$Z_m^{\overline{\text{MS}}}(\mu) \overline{m}(\mu) = Z_m^{\text{OS}} m^{\text{OS}}. \quad (5.65)$$

I.e. the coefficients c_1 and c_2 can simply be extracted after expanding the ratio $Z_m^{\overline{\text{MS}}}(\mu)/Z_m^{\text{OS}}$ in α_s . The renormalization constants themselves have logarithmic dependencies on the $\overline{\text{MS}}$ - and OS-masses. We eliminate any residual logarithmic dependence on the OS-mass by recursively inserting the relation (5.64). Note that if the quark with the mass m is not being decoupled from the running of α_s , then its mass is set to zero in all contributions to the renormalization constants which feature a closed quark loop of that flavor. This is to ensure consistency with our previous prescription of quark masses.

With the renormalization constants computed in Refs. [172, 173] we find

$$\begin{aligned}
c_1^{(n_f, n_l)}(\mu) &= C_F \left(1 - \frac{3}{4} \ln \left(\frac{\overline{m}^{(n_f)}(\mu)^2}{\mu^2} \right) \right), \\
c_2^{(n_f, n_l)}(\mu) &= -\frac{1}{384} C_F \left\{ C_A \left(-132 \ln^2 \left(\frac{\overline{m}^{(n_f)}(\mu)^2}{\mu^2} \right) + 740 \ln \left(\frac{\overline{m}^{(n_f)}(\mu)^2}{\mu^2} \right) + 144\zeta(3) - 1111 + \pi^2(32 - 96 \ln(2)) \right) \right. \\
&\quad + 3C_F \left(-36 \ln^2 \left(\frac{\overline{m}^{(n_f)}(\mu)^2}{\mu^2} \right) - 36 \ln \left(\frac{\overline{m}^{(n_f)}(\mu)^2}{\mu^2} \right) - 96\zeta(3) + 71 + 8\pi^2(8 \ln(2) - 5) \right) \\
&\quad + 4n_l T_F \left(12 \ln^2 \left(\frac{\overline{m}^{(n_f)}(\mu)^2}{\mu^2} \right) - 52 \ln \left(\frac{\overline{m}^{(n_f)}(\mu)^2}{\mu^2} \right) + 8\pi^2 + 71 \right) \Big\} \\
&\quad - \sum_{i=n_l+1}^{n_f} \frac{1}{96} C_F T_F \left(12 \ln^2 \left(\frac{\overline{m}^{(n_f)}(\mu)^2}{\mu^2} \right) - 24 \ln \left(\frac{\overline{m}^{(n_f)}(\mu)^2}{\mu^2} \right) \ln \left(\frac{\overline{m}_i^{(n_f)}(\mu)^2}{\mu^2} \right) - 52 \ln \left(\frac{\overline{m}^{(n_f)}(\mu)^2}{\mu^2} \right) \right. \\
&\quad + 32 \ln \left(\frac{\overline{m}_i^{(n_f)}(\mu)^2}{\mu^2} \right) + 48(x_i - 1)^2 (x_i^2 + x_i + 1) \text{Li}_2(1 - x_i) + 48x_i^4 \ln^2(x_i) + 48x_i^2 \ln(x_i) \\
&\quad \left. - 48(x_i^4 + x_i^3 + x_i + 1) (\text{Li}_2(-x_i) + \ln(x_i) \ln(x_i + 1)) - 16\pi^2(x_i^3 + x_i) + 72x_i^2 + 71 \right), \tag{5.67}
\end{aligned}$$

where we defined $x_i = \frac{\overline{m}_i^{(n_f)}(\mu)}{\overline{m}^{(n_f)}(\mu)}$, n_f is the total number of quarks, i.e. $n_f = 6$ in the SM and n_l is the number of light quarks, i.e. the number of quarks which have not been decoupled in the running of α_s . The sum therefore runs over all quark flavors which are decoupled from the running of α_s ; this includes the quark with mass $\overline{m}^{(n_f)}$ in case it is decoupled. This implies that the OS- $\overline{\text{MS}}$ -mass relation of the bottom-quark somehow depends on the mass of the top-quark. Since the top-quark mass is orders of magnitudes larger than the bottom-quark mass, this seems quite unphysical. The problem is that we relate the OS-mass with the bottom-quark mass within the full $n_f = 6$ theory. Instead, we would like to relate the OS-mass to the decoupled masses defined by

$$\begin{aligned}
\overline{m}^{(n_m)} &= \zeta_m \left(\alpha_s^{(n_m+1)}(\mu), \ln \frac{m^2}{\mu^2} \right) \alpha_s^{(n_m+1)}(\mu), \\
\text{with } \zeta_m(\alpha_s, L) &= 1 + \left(\frac{\alpha_s}{\pi} \right)^2 T_F \left[\frac{89}{288} C_F + \frac{5}{24} C_F L + \frac{C_F}{8} L^2 \right]. \tag{5.68}
\end{aligned}$$

Ones we expand our relation in $x_i \ll 1$, which we can do anyway, as all decoupling relations only hold up to power corrections, we find that all non-decoupling effects cancel as expected. The coefficients for general $n_m \leq n_f$ are therefore given by Eq. (5.67) upon replacing $n_f \rightarrow n_m$ on the left and right-hand side.

In case we have a hierarchy among the mass scales for which $x_i \gg 1$, for example when considering the top-quark OS- $\overline{\text{MS}}$ -mass relation in the 4FS, we can expand the expression yielding

$$\begin{aligned}
c_1^{(n_m, n_l)}(\mu) &= C_F \left(1 - \frac{3}{4} \ln \left(\frac{\overline{m}^{(n_m)}(\mu)^2}{\mu^2} \right) \right), \\
c_2^{(n_m, n_l)}(\mu) &= -\frac{1}{384} C_F \left\{ C_A \left(-132 \ln^2 \left(\frac{\overline{m}^{(n_m)}(\mu)^2}{\mu^2} \right) + 740 \ln \left(\frac{\overline{m}^{(n_m)}(\mu)^2}{\mu^2} \right) + 144\zeta(3) - 1111 + \pi^2 (32 - 96 \ln(2)) \right) \right. \\
&\quad + 3C_F \left(-36 \ln^2 \left(\frac{\overline{m}^{(n_m)}(\mu)^2}{\mu^2} \right) - 36 \ln \left(\frac{\overline{m}^{(n_m)}(\mu)^2}{\mu^2} \right) - 96\zeta(3) + 71 + 8\pi^2 (8 \ln(2) - 5) \right) \\
&\quad \left. + 4n_l T_F \left(12 \ln^2 \left(\frac{\overline{m}^{(n_m)}(\mu)^2}{\mu^2} \right) - 52 \ln \left(\frac{\overline{m}^{(n_m)}(\mu)^2}{\mu^2} \right) + 8\pi^2 + 71 \right) \right\} \\
&\quad - \frac{1}{96} C_F T_F \left\{ 72 \right. \\
&\quad \left. + \sum_{i=n_l+1}^{n_m} \left[71 - 20 \ln \left(\frac{\overline{m}^{(n_m)}(\mu)^2}{\mu^2} \right) - 12 \ln^2 \left(\frac{\overline{m}^{(n_m)}(\mu)^2}{\mu^2} \right) + 8\pi^2 (1 - 3x_i) + 16 \ln(x_i) \left(4 - 3 \ln \left(\frac{\overline{m}^{(n_m)}(\mu)^2}{\mu^2} \right) \right) \right] \right\}.
\end{aligned} \tag{5.70}$$

The sum once again runs over all quark flavors decoupled from the running of α_s , with masses less or equal than m . We once again underscore that these are not the standard relations between the pole and the $\overline{\text{MS}}$ -masses, thanks to our prescription of the bottom quark mass in loops that do not couple to the Higgs. However, the standard relations follow upon replacing

$$n_l \longrightarrow n_l - 1 \tag{5.71}$$

in Eqs. (5.67) and (5.70).

For convenience of the reader we also provide the numerical values for the top- and bottom-quark mass scheme relations in the 4 and 5FSs

$$\begin{aligned}
5\text{FS} : m_t &= \overline{m}_t^{(6)}(\overline{m}_t^{(6)}) \left(1 + 1.333 \times \frac{\alpha_s^{(5)}}{\pi} + 8.237 \times \left(\frac{\alpha_s^{(5)}}{\pi} \right)^2 + \mathcal{O}(\alpha_s^3) \right) \\
&= (162.7 + 7.493 + 1.608) \text{ GeV},
\end{aligned} \tag{5.72}$$

$$\begin{aligned}
4\text{FS} : m_t &= \overline{m}_t^{(6)}(\overline{m}_t^{(6)}) \left(1 + 1.333 \times \frac{\alpha_s^{(4)}}{\pi} + 8.864 \times \left(\frac{\alpha_s^{(4)}}{\pi} \right)^2 + \mathcal{O}(\alpha_s^3) \right) \\
&= (162.7 + 7.434 + 1.694) \text{ GeV},
\end{aligned} \tag{5.73}$$

$$\begin{aligned}
5\text{FS} : m_b &= \overline{m}_b^{(5)}(\overline{m}_b^{(5)}) \left(1 + 1.333 \times \frac{\alpha_s^{(5)}}{\pi} + 8.132 \times \left(\frac{\alpha_s^{(5)}}{\pi} \right)^2 + \mathcal{O}(\alpha_s^3) \right) \\
&= (4.18 + 0.398 + 0.174) \text{ GeV},
\end{aligned} \tag{5.74}$$

$$\begin{aligned}
4\text{FS} : m_b &= \overline{m}_b^{(5)}(\overline{m}_b^{(5)}) \left(1 + 1.333 \times \frac{\alpha_s^{(4)}}{\pi} + 9.278 \times \left(\frac{\alpha_s^{(4)}}{\pi} \right)^2 + \mathcal{O}(\alpha_s^3) \right) \\
&= (4.18 + 0.443 + 0.245) \text{ GeV}.
\end{aligned} \tag{5.75}$$

We stress that the top-quark masses on the right-hand side of Eqs. (5.72) and (5.73) are not decoupled, and for the bottom-quark masses in Eqs. (5.74) and (5.75), only the top-quark is decoupled. The first two expansion parameters already indicate a relatively good perturbative convergence for the top-quark, whereas the bottom quark receives quite large correction, a phenomenon which actually worsens with higher orders of perturbation theory [123, 124]. The top quark mass is not relevantly effected by the choice of the FS, whereas we see a slight shift of the bottom-quark mass of around 2%.

We can now insert the OS- $\overline{\text{MS}}$ -mass relation into the OS-renormalized amplitudes and subsequently expand in α_s , yielding the relation between the amplitudes in the two schemes

$$\begin{aligned}\mathcal{M}^{\overline{\text{MS}}}(\overline{m}(\mu)) &= \mathcal{M}^{\text{OS}}(\overline{m}(\mu)) + \delta\mathcal{M}(\overline{m}(\mu)), \\ \delta\mathcal{M}^{(1)}(\overline{m}(\mu)) &= \overline{m}(\mu)c_1(\mu)\frac{\alpha_s(\mu)}{\pi}\frac{d\mathcal{M}^{\text{OS},(0)}}{dm}\bigg|_{m=\overline{m}(\mu)}, \\ \delta\mathcal{M}^{(2)}(\overline{m}(\mu)) &= \overline{m}(\mu)\left[c_1(\mu)\frac{\alpha_s(\mu)}{\pi}\frac{d\mathcal{M}^{\text{OS},(1)}}{dm}\bigg|_{m=\overline{m}(\mu)} + c_2(\mu)\left(\frac{\alpha_s(\mu)}{\pi}\right)^2\frac{d\mathcal{M}^{\text{OS},(0)}}{dm}\bigg|_{m=\overline{m}(\mu)}\right] \\ &\quad + \frac{1}{2}\left(\overline{m}(\mu)c_1(\mu)\frac{\alpha_s(\mu)}{\pi}\right)^2\frac{d^2\mathcal{M}^{\text{OS},(0)}}{dm^2}\bigg|_{m=\overline{m}(\mu)}.\end{aligned}\tag{5.76}$$

The relevant LO and NLO amplitudes are known fully analytically, and we perform the necessary mass derivatives fully automatized using **Mathematica**.

5.4 PERFORMING THE PHASE-SPACE INTEGRATION

Once, we collected all the relevant amplitudes, we perform the phase-space integration to obtain cross sections. We perform the phase-space integration numerically using MC methods. The IR-singularities arising during the integration are handled using the *sector-improved residue subtraction scheme*⁷ [27], implemented in the private software package **Stripper**.

Typically, **Stripper** runs the MC simulation at a fixed renormalization scale, and then evolves the final result to other desired scales automatically based on the provided lower order amplitudes. This procedure is however only implemented if the involved masses are renormalization scale independent, hence it is not fully automatized in the $\overline{\text{MS}}$ -scheme. Each individual renormalization scale is therefore run individually.

For the top-quark induced Higgs-production cross section we subtract the rHTL limit already on the integrand level. Since the rHTL already captures the bulk of the cross section, this massively improves the MC uncertainties. To get the total cross section we can then add back the rHTL cross section after performing the phase-space integration. The rHTL cross sections on the other hand can be evaluated extremely efficiently by public software tools like **SusHi** or **iHixs**.

⁷ See section 2.2.3 for a brief review on subtraction schemes.

6 | RESULTS AND DISCUSSION

In this chapter we will present the main results of this PhD thesis. We will show the total and differential top-bottom interference contribution to the cross section. We present results in the 4 and 5FS. Further we compare results in the OS- and the $\overline{\text{MS}}$ -renormalization scheme for the top- and bottom-quark mass. The pure top-quark mass effects are also provided. Lastly we compare our findings with other works.

We use two scale choices for fully-inclusive cross section we use the central scale of $\mu = m_H/2$, as it shows very good perturbative convergence as explained in section 4.3.1. In differential cross section we use the dynamic scale

$$\mu = \frac{H_T}{2} \equiv \frac{1}{2} \left(\sqrt{m_H^2 + p_T^2} + \sum_i p_{i,T} \right), \quad (6.1)$$

where p_T is the transverse momentum of the Higgs, and $p_{i,T}$ is the transverse momentum of the i -th final state parton. The scale was chosen on the one hand to match previous studies [135, 137, 131], but also to improve perturbative convergence at large p_T , where the Higgs mass alone is no longer the natural scale. This can for example be seen nicely in the phase-space measure in Eq. (4.76), which shows that at large transverse momentum we encounter logarithms of the form $\log(\mu^2/s)$.

Unless specified otherwise, we follow the computational setup described in the conventions.

6.1 TOTAL CROSS SECTION

6.1.1 Effects of Finite Top-Quark Masses

As mentioned before, the effect of finite top quark mass effects on the Higgs production cross section in the OS-scheme have already been studied in Ref. [122]. Here we reproduce theses result and complement them with scale uncertainties. We further provide results for additional center of mass energies. The results are displayed in Tab. 6.1. Additionally, we show a comparison of the HTL and the full cross section in the various partonic channels in Fig. 4.9 and Tab. 4.3. As we discussed before, the rHTL approximates the cross section extremely well. By looking at Fig. 4.9, we see that this is especially true for the gluon-gluon channel, whereas the other channels show discrepancies of $\mathcal{O}(10)\%$. The dominance of the gluon-gluon channel then results in the astonishing accuracy of the rHTL when combining all partonic channels, yielding approximations with sub-percent precision. We observe that the NNLO correction of $\sigma_t - \sigma_{\text{rHTL}}$ has the opposite sign and roughly half the magnitude of the NLO correction. The lower scale uncertainties are reduced drastically by a factor of 4–6 going from NLO to NNLO, whilst the upper uncertainties increase slightly.

In Tab. 6.2 we show the difference between top-quark induced gluon-gluon fusion cross section computed with a top-quark mass defined in the $\overline{\text{MS}}$ - and the OS-scheme. Based on the

previously known LO and NLO order results, it was conjectured that the renormalization scheme of the top-quark mass has little effect on the cross section. We find this trend continued at NNLO, where the difference amounts to just -0.01 pb or 0.2% at 13 TeV. Based on our findings, we conclude that the scale uncertainties severely overestimate the uncertainty of the difference, which decrease slightly going from NLO to NNLO.

Lastly, we compare the pure top-quark effects between the 4 and 5FS. Here the Higgs boson is always produced through a coupling to the top-quark, but the two schemes differ in the treatment of the bottom-quark mass. The results are displayed in Tab. 6.3. The differences between the two schemes are insignificant, reaching 0.03 pb at NLO and 0.01 pb at NNLO at a center of mass energy of 13 TeV. At NLO the only difference between the computations is the used PDF set and the additional $qg \rightarrow Hq$ channel in the 5FS. Only at NNLO, we have explicit dependence on the bottom-quark mass in the 4FS, which does however not give rise to significant deviations. On the contrary, the NNLO results are already shifted even closer together. We stress however, that the cross sections of the rHTL are shifted by a significant -1.16 pb from the 5 to the 4FS (see Tab. 6.5).

6.1.2 Effects of Finite Bottom-Quark Masses

Tab. 6.4 shows one of the major findings of this work, the top-bottom interference contribution to the gluon-gluon fusion cross section at NNLO. Herein, we compare various computational setups, including results computed with $\overline{\text{MS}}$ - and On-shell renormalization (OS)-renormalized bottom- and top-quark masses, as well different results in the 5 and 4FS.

Order	σ_{rHTL} [pb]	$(\sigma_t - \sigma_{\text{rHTL}})$ [pb]	$(\sigma_t - \sigma_{\text{rHTL}})/\sigma_{\text{rHTL}}$ [%]
$\sqrt{s} = 7 \text{ TeV}$			
$\mathcal{O}(\alpha_s^2)$	+5.85	–	
LO	$5.85^{+1.56}_{-1.11}$	–	–
$\mathcal{O}(\alpha_s^3)$	+7.14	–0.0604	
NLO	$12.99^{+2.89}_{-2.14}$	$-0.0604^{+0.021}_{-0.037}$	–0.5
$\mathcal{O}(\alpha_s^4)$	+3.28	+0.0386(2)	
NNLO	$16.27^{+1.45}_{-1.61}$	$-0.0218(2)^{+0.035}_{-0.009}$	–0.1
$\sqrt{s} = 8 \text{ TeV}$			
$\mathcal{O}(\alpha_s^2)$	+7.39	–	
LO	$7.39^{+1.98}_{-1.40}$	–	–
$\mathcal{O}(\alpha_s^3)$	+9.14	–0.0873	
NLO	$16.53^{+3.63}_{-2.73}$	$-0.0873^{+0.030}_{-0.052}$	–0.5
$\mathcal{O}(\alpha_s^4)$	+4.19	+0.0523(2)	
NNLO	$20.72^{+1.84}_{-2.06}$	$-0.0350(2)^{+0.048}_{-0.013}$	–0.2
$\sqrt{s} = 13 \text{ TeV}$			
$\mathcal{O}(\alpha_s^2)$	+16.30	–	
LO	$16.30^{+4.36}_{-3.10}$	–	–
$\mathcal{O}(\alpha_s^3)$	+21.14	–0.303	
NLO	$37.44^{+8.42}_{-6.29}$	$-0.303^{+0.10}_{-0.17}$	–0.8
$\mathcal{O}(\alpha_s^4)$	+9.72	+0.147(1)	
NNLO	$47.16^{+4.21}_{-4.77}$	$-0.156(1)^{+0.13}_{-0.03}$	–0.3
$\sqrt{s} = 13.6 \text{ TeV}$			
$\mathcal{O}(\alpha_s^2)$	+17.47	–	
LO	$17.47^{+4.67}_{-3.32}$	–	–
$\mathcal{O}(\alpha_s^3)$	+22.76	–0.338	
NLO	$40.23^{+9.07}_{-6.77}$	$-0.338^{+0.11}_{-0.18}$	–0.8
$\mathcal{O}(\alpha_s^4)$	+10.47	+0.162(1)	
NNLO	$50.70^{+4.53}_{-5.14}$	$-0.176(1)^{+0.14}_{-0.03}$	–0.3
$\sqrt{s} = 14 \text{ TeV}$			
$\mathcal{O}(\alpha_s^2)$	+18.26	–	
LO	$18.26^{+4.88}_{-3.47}$	–	–
$\mathcal{O}(\alpha_s^3)$	+23.86	–0.362	
NLO	$42.12^{+9.51}_{-7.10}$	$-0.362^{+0.12}_{-0.20}$	–0.9
$\mathcal{O}(\alpha_s^4)$	+10.98	+0.171(1)	
NNLO	$53.10^{+4.75}_{-5.39}$	$-0.191(1)^{+0.15}_{-0.04}$	–0.4

Table 6.1: Total gluon-gluon fusion cross section in the rHTL and the pure top-quark mass effects for a selection of hadronic center of mass energies relevant for LHC phenomenology. The top-quark mass is renormalized in the OS-scheme. The computational setup is described in the conventions. The scale uncertainties are determined with seven-point variation.

Order	$(\sigma_t^{\overline{\text{MS}}} - \sigma_t^{\text{OS}})$ [pb]
$\sqrt{s} = 13$ TeV	
$\mathcal{O}(\alpha_s^2)$	-0.04
LO	$-0.04^{+0.12}_{-0.17}$
$\mathcal{O}(\alpha_s^3)$	+0.02
NLO	$-0.02^{+0.14}_{-0.30}$
$\mathcal{O}(\alpha_s^4)$	+0.01
NNLO	$-0.01^{+0.12}_{-0.24}$

Table 6.2: Difference of cross sections for Higgs production through a closed top-quark loop with the top-quark mass defined either in the $\overline{\text{MS}}$ or the OS scheme. The results are computed for LHC @ 13 TeV using the computational setup is described in the conventions. The scale uncertainties are determined with seven-point variation.

Order	$(\sigma_t - \sigma_{\text{rHTL}})$ [pb]	
$\sqrt{s} = 13$ TeV		
	5FS	4FS
	$m_t = 173.06$ GeV	$m_t = 173.06$ GeV
		$\overline{m}_b(\overline{m}_b) = 4.18$ GeV
LO	-	-
$\mathcal{O}(\alpha_s^3)$	-0.30	-0.27
NLO	$-0.30^{+0.10}_{-0.17}$	$-0.27^{+0.09}_{-0.16}$
$\mathcal{O}(\alpha_s^4)$	+0.14	+0.12
NNLO	$-0.16^{+0.13}_{-0.03}$	$-0.15^{+0.10}_{-0.02}$

Table 6.3: Effect of the finite top-quark mass on the gluon-gluon fusion cross section in the 4 and 5FS. The top-quark mass is defined in the OS-scheme, while the bottom-quark mass is defined in the $\overline{\text{MS}}$ -scheme. The results are computed for LHC @ 13 TeV using the computational setup is described in the conventions. The scale uncertainties are determined with seven-point variation.

Order	$\sigma_{t \times b}$ [pb]				
$\sqrt{s} = 13$ TeV					
	5FS	5FS	5FS	4FS	5FS
	$m_t = 173.06$ GeV	$m_t = 173.06$ GeV	$\overline{m}_t(\overline{m}_t) = 162.7$ GeV	$m_t = 173.06$ GeV	$m_t = 173.06$ GeV
	$\overline{m}_b(\overline{m}_b) = 4.18$ GeV	$m_b = 4.78$ GeV	$\overline{m}_b(\overline{m}_b) = 4.18$ GeV	$\overline{m}_b(\overline{m}_b) = 4.18$ GeV	$m_b = 4.78$ GeV
					$Y_b = \overline{m}_b/v$
$\mathcal{O}(\alpha_s^2)$	-1.11	-1.98	-1.12	-1.15	-1.223
LO	$-1.11^{+0.28}_{-0.43}$	$-1.98^{+0.38}_{-0.53}$	$-1.12^{+0.28}_{-0.42}$	$-1.15^{+0.29}_{-0.45}$	$-1.223^{+0.29}_{-0.44}$
$\mathcal{O}(\alpha_s^3)$	-0.65	-0.44	-0.64	-0.66	-0.623(1)
NLO	$-1.76^{+0.27}_{-0.28}$	$-2.42^{+0.19}_{-0.12}$	$-1.76^{+0.27}_{-0.28}$	$-1.81^{+0.28}_{-0.30}$	$-1.85^{+0.26}_{-0.26}$
$\mathcal{O}(\alpha_s^4)$	+0.02	+0.43	-0.02	-0.02	+0.019(5)
NNLO	$-1.74(2)^{+0.13}_{-0.03}$	$-1.99(2)^{+0.29}_{-0.15}$	$-1.78(1)^{+0.15}_{-0.03}$	$-1.83(2)^{+0.14}_{-0.03}$	$-1.83(1)^{+0.08}_{-0.03}$

Table 6.4: Top-bottom interference contribution to the gluon-gluon fusion cross section for various computational setups. The results are computed for LHC @ 13 TeV using the computational setup is described in the conventions. The scale uncertainties are determined with seven-point variation. Numbers in parentheses indicate the MC uncertainties on the last provided digit.

Using an $\overline{\text{MS}}$ -bar renormalized bottom-quark mass, an OS renormalized top-quark mass, and the 5FS, we find that the central value is not shifted significantly going from NLO to NNLO. The result is therefore consistent within the previously estimated scale uncertainty bands. The latter are reduced significantly in this setup. The upwards scale variation is halved, reaching a precision of 7% whereas the lower uncertainty is reduced even further to about 2%. Overall we observe a good perturbative convergence using this setup.

When the top-quark mass is renormalized in the $\overline{\text{MS}}$ -scheme instead (3rd column of Tab. 6.4), we find very mild changes in the results. This is true both for the central value and the associated scale uncertainties. This aligns with our expectations, as we already observed, little to no dependence on the top-quark mass renormalization-scheme, in the pure top-quark mass effects.

The situation is very different for the renormalization scheme of the bottom-quark, however. At LO, the cross sections in two renormalization schemes differ by almost 80%. At this order, the only difference during the computation is the numerical value of the bottom-quark mass. The OS-mass of the bottom quark is $m_b = 4.78$ GeV, while the $\overline{\text{MS}}$ -mass at the central scale can be read off Fig. 5.16 and reads about $\overline{m}_b(m_H/2) = 3.0$ GeV. The large difference at LO is therefore explained by the large discrepancy of the two mass values and the fact that the Higgs-gluon form factor show a strong quadratic dependence on the quark mass in the HEL (see Eq. (4.12)). In principle, the difference should be mitigated when including higher orders in perturbation theory. The bad perturbative convergence of the $\overline{\text{MS}}$ -OS-mass relation in Eq. (5.74) however, often averts this in practice. Indeed, although we observe that the gap between the $\overline{\text{MS}}$ - and OS-results is reduced significantly, the results in the OS-scheme are unreliable, as the NNLO correction has nearly the same magnitude as the NLO correction but comes with the opposite sign. Alternating corrections of similar magnitude are a typical indicator of bad perturbative convergence. The NNLO corrections also lie outside the previously estimated uncertainty band. Additionally, we find that the scale uncertainties actually increase going from NLO to NNLO giving us further evidence, that the cross section does not stabilize in the OS-scheme. The main conclusion here is that the cross section results with an OS-renormalized bottom-quark mass are not trustworthy. The NNLO predictions therefore allowed us to eliminate the scheme-uncertainty previously associated with the gluon-gluon fusion cross section, by conclusively demonstrating that the $\overline{\text{MS}}$ -scheme performs better in this instance.

To further investigate the origin of the improvements of the perturbative convergence in the $\overline{\text{MS}}$ -scheme, we also computed results in a mixed renormalization scheme, where the bottom-quark mass is renormalized in the OS-scheme, but the Yukawa coupling of the Higgs and the bottom-quark is renormalized in the $\overline{\text{MS}}$ -scheme. We stress that this scheme is inconsistent, since in the SM, the Yukawa couplings are set by the mass via

$$Y = \frac{m}{v}, \quad (6.2)$$

hence the renormalization constant of the Yukawa coupling is fixed by the respective constants of the mass and the VEV. With the inclusion of electroweak corrections, this can result in serious problems, but since our considerations are limited to QCD corrections, we can ignore these for our purposes. The results are much easier to calculate from the OS-results than when using the $\overline{\text{MS}}$ -scheme consistently, because the Yukawa coupling only enters our cross

section linearly, which means that the derivatives in Eq. (5.76) are trivial, and the perturbative corrections can be obtained via

$$\begin{aligned}
\sigma_{t \times b, \text{Mixed}}^{(0)} &= \frac{\overline{m}_b}{m_b} \sigma_{t \times b, \text{OS}}^{(0)} \\
\sigma_{t \times b, \text{Mixed}}^{(1)} &= \frac{\overline{m}_b}{m_b} \left[\sigma_{t \times b, \text{OS}}^{(1)} + c_1^{(5,5)} \frac{\alpha_s}{\pi} \sigma_{t \times b, \text{OS}}^{(0)} \right] \\
\sigma_{t \times b, \text{Mixed}}^{(2)} &= \frac{\overline{m}_b}{m_b} \left[\sigma_{t \times b, \text{OS}}^{(2)} + c_1^{(5,5)} \frac{\alpha_s}{\pi} \sigma_{t \times b, \text{OS}}^{(1)} + c_2^{(5,5)} \left(\frac{\alpha_s}{\pi} \right)^2 \sigma_{t \times b, \text{OS}}^{(0)} \right], \\
\text{with } \sigma_{t \times b}^{\text{NNLO}} &= \sigma_{t \times b}^{(0)} + \sigma_{t \times b}^{(1)} + \sigma_{t \times b}^{(2)}.
\end{aligned} \tag{6.3}$$

The results for the mixed renormalization scheme are displayed in the last column of Tab. 6.4. We can see that the main improvements on the perturbative convergence are already captured by the mixed scheme, as we no longer encounter alternating corrections of similar magnitude. The central values are compatible across all orders with the results computed using a consistent $\overline{\text{MS}}$ -renormalized bottom quark within the provided scale uncertainties. The scale uncertainties themselves are generally also very similar, and even slightly reduced.

It is clear from the bad perturbative convergence of the OS- $\overline{\text{MS}}$ -mass relation of the bottom-quark and the strong dependence mass-dependence of the cross section below the threshold, that the OS- and the $\overline{\text{MS}}$ -mass renormlized cross section can not both have good convergence, i.e. if one converges nicely the other must consequently converge poorly¹. As to why it is the $\overline{\text{MS}}$ -scheme which performs better: the standard argument is that logarithms of the form $\log(m_b^2/\mu^2)$ are automatically resummed in the $\overline{\text{MS}}$ -scheme to all orders by means of the RGE running of the bottom-quark mass. In the top-bottom interference contribution however, we also encounter Sudakov-type logarithms of the form $\log^2(m_b^2/m_H^2)$ (see for example Eq. (4.12)). These logarithms should in principle dominate over the UV-logarithms, making the standard reasoning not directly applicable. Without further insight about the underlying structure of these double logarithms², it is hard to give a conclusive reason, and we leave this question for future research.

Lastly, we compare the results of the different FSs. Similarly to the pure top-quark mass effects, we find that the differences are mild. Once again, at LO the only difference in the computation is the used PDF set and at NLO the computations additionally differ by the inclusion of the $bg \rightarrow Hb$ channel in the 5FS, which due to the small PDF of the bottom-quark does not impact the result significantly. Only at NNLO, do we encounter differences in the calculation of amplitudes, due to closed bottom-quark masses which are not coupled to the Higgs. We observe, that the 4 and 5FS are compatible within the provided uncertainties across all orders. The treatment of bottom-quark mass in the 5FS therefore seems to capture the effects from finite bottom-quark masses well. Intuitively, this seems reasonable, because the massless limit $m_b \rightarrow 0$, works extremely well in QCD at LHC energies. We would hence expect the same for loops that do not couple to Higgs. It is nevertheless important to verify this intuition, and validate that electroweak effects which are causing the strong mass dependence are not creeping into the parts of the amplitude which should be dominated by QCD.

¹ Of course, it is also possible that both of them converge poorly.

² There has been attempts to understand the origin of the logarithms in the abelian part of the amplitudes [174].

6.2 DIFFERENTIAL CROSS SECTION

Besides the total cross section we also computed results for differential cross section distributions, specifically for the Higgs- p_T and the Higgs-rapidity distribution.

In Fig. 6.1, we show the top-bottom interference contribution to the two differential cross sections at NNLO³. Herein we compare results for an OS and an $\overline{\text{MS}}$ renormalized bottom-quark mass. Fig. 6.2 then shows the complete differential cross section, i.e. including the pure-top-quark and top-bottom interference contribution, and compares them to the respective results in the rHTL⁴. The Higgs- p_T distribution is particularly interesting, as the various

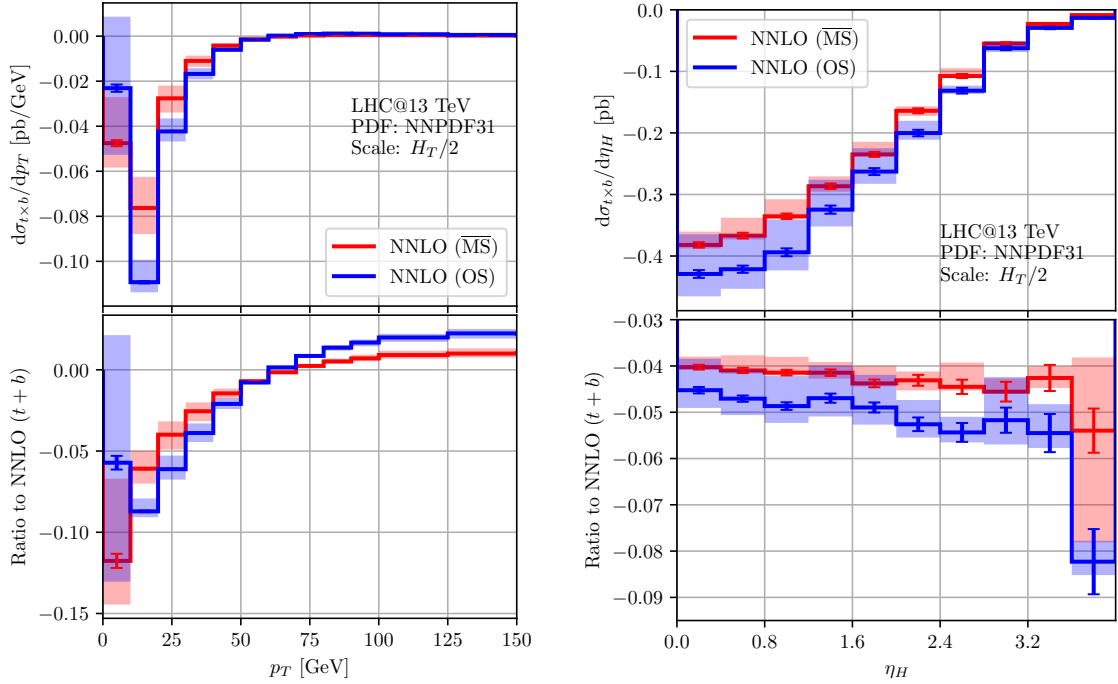


Figure 6.1: Higgs- p_T (left) and Higgs-rapidity (right) distribution for the gluon-gluon fusion channel. Compared are the 5FS results obtained in the rHTL with those including finite-quark-mass effects (pure top-quark mass effects + top-bottom interference contribution). The bottom-quark mass is renormalized in the $\overline{\text{MS}}$ scheme, while the top-quark mass is renormalized in the OS scheme. The results are computed for LHC @ 13 TeV using the computational setup is described in the conventions. The transparent bands indicate the scale uncertainties, whereas the error bars show the MC uncertainty.

regions of p_T are sensitive to very different physics. At large $p_T \gg m_t$, we see that the rHTL completely breaks down and we are increasingly sensitive to finite top-quark mass effects. In section 4.3.6, we explained that this is due to the non-vanishing mass dimension of coupling in of the HTL, resulting in a less suppressed high p_T -tail. Our analysis concluded, that the ratio of the rHTL and SM differential cross section must grow quadratically in p_T (see Eq. (4.111)). We find this rough estimate confirmed⁵ in the ratio plot of the p_T distribution in Fig. 6.2. For $p_T > 50$ GeV the NNLO correction shifts the distribution upwards by around a factor

³ In Fig. 6.3 we also show OS-scheme results for a slightly altered computational setup, with a finer binning.

⁴ In Fig. D.1 we present the analogous results for an OS renormalized bottom quark mass.

⁵ A linear fit of the differential cross section with double logarithmic axes resulted in a slope of 1.95 with a p_T range of [500 GeV, 1000 GeV]. Tighter bounds yielded results even closer to 2.

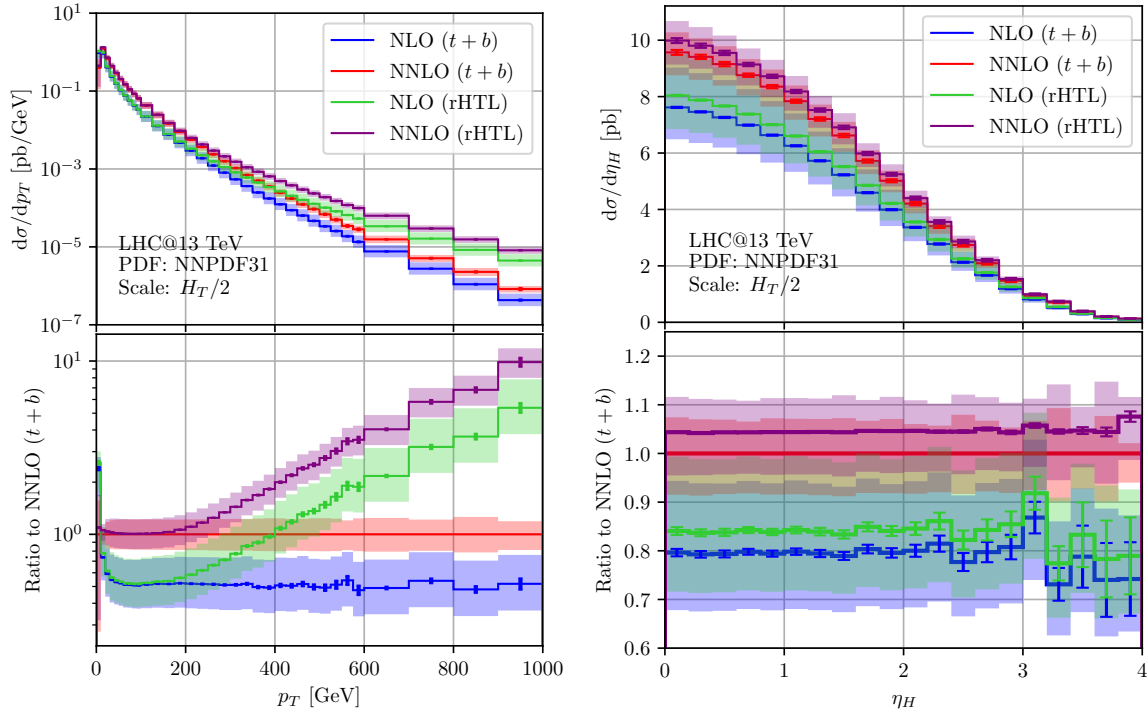


Figure 6.2: Higgs- p_T (left) and Higgs-rapidity (right) distribution for the gluon-gluon fusion channel. Compared are the 5FS results obtained in the rHTL with those including finite-quark-mass effects (pure top-quark mass effects + top-bottom interference contribution). The bottom-quark mass is renormalized in the $\overline{\text{MS}}$ scheme, while the top-quark mass is renormalized in the OS scheme. The results are computed for LHC @ 13 TeV using the computational setup is described in the conventions. The transparent bands indicate the scale uncertainties, whereas the error bars show the MC uncertainty.

of two, both for the rHTL and the SM results. At lower transverse momentum $p_T < m_t$, the cross section is well approximated by the rHTL apart from the missing light-quark mass effects which are only relevant for $p_T < 50$ GeV. At small transverse momenta, the fixed order cross sections are logarithmically enhanced by $\log(p_T^2/m_H^2)$, which spoil the perturbative convergence. These kinds of logarithms can be resummed to all orders of perturbation theory. For the pure-top-quark effects, the fixed order results can be compared to parton shower matched results [144], and one observes that resummation only becomes relevant below transverse momenta of 20 GeV. In the very low p_T region where $p_T \ll m_b$, the bottom quark is not resolved and the appearing logarithms can be resummed once again. However, this region is also sensitive to non-perturbative effects. For intermediate transverse momenta $m_b < p_T < m_H$, the top-bottom interference contribution also receives additional logarithms of the form $\log p_T/m_b$ and $\log m_H/m_b$, which could further worsen the perturbative convergence. The origin and resummation of these are not well understood, however the resummation effects have been estimated in Ref. [136]. In that reference, the authors show, that the effects are only relevant for transverse momenta below 20 GeV. Our fixed order results are hence reliable above this threshold.

The comparison of the p_T -distributions computed with OS and $\overline{\text{MS}}$ renormalized bottom-quark mass shows that the two schemes are compatible for transverse momenta above 30 GeV. Below this, we see significant deviations and a more sharp spike at around 15 GeV in the OS scheme. In the $\overline{\text{MS}}$ scheme the spike is also visible but less pronounced and overall there is a smoother

low- p_T behavior, indicating that the main improvements on the perturbative convergence over the OS scheme come from this region of the phase-space.

The rapidity distribution is not subject to logarithmic enhancements and is reliable across the entire range. The distribution overall is less feature rich. With a $\overline{\text{MS}}$ renormalized bottom-quark mass, the top-bottom interference contribution approximately results in a shift of -4% across the entire rapidity spectrum. In the OS scheme the shift is slightly larger—around -4.5% with a slight negative tilt towards larger rapidities. Relative scale uncertainties remain roughly constant and are significantly larger in the OS-scheme, as expected from our findings on the total cross section (see Tab. 6.4). In the right panel of Fig. 6.2, we can see that the NNLO corrections on the total cross section result in a shift of $+20\%$ across the entire rapidity spectrum, both for the rHTL and the SM cross section. This once again perfectly aligns with the observed corrections in the total cross section in Tab. 6.1. Likewise the rHTL differential cross section overestimates the cross section by around $4 - 5\%$ across the entire spectrum, aligning perfectly with the observed shift of the top-bottom interference contribution in the right panel Fig. 6.1.

6.3 VALIDATION & COMPARISON WITH OTHER WORKS

In the 4FS, the bottom-quark mass acts as an IR-regulator, resulting in huge logarithmic enhancements of the individual amplitudes. To check that these enhancements cancel in inclusive observables, we performed the calculation of the rHTL cross section for a number of small bottom-quark masses. That means that the cross section contains only contributions arising from the effective coupling of the Higgs to gluons, and the bottom-quark mass is only relevant in bottom-quark loops which are not coupling to the Higgs. These are however the relevant loops, which give rise to the logarithmic enhancements. The results are displayed in Tab. 6.5. The results clearly show that there are no logarithmic enhancements on the cross

Order	σ_{rHTL} [pb]				
$\sqrt{s} = 13 \text{ TeV}$					
	5FS	4FS	4FS	4FS	4FS
		$m_b = 0.01 \text{ GeV}$	$m_b = 0.1 \text{ GeV}$	$m_b = 4.78 \text{ GeV}$	$\overline{m}_b(\overline{m}_b) = 4.18 \text{ GeV}$
$\mathcal{O}(\alpha_s^2)$	+16.30	+16.27	+16.27	+16.27	16.27
LO	$16.30^{+4.36}_{-3.10}$	$16.27^{+4.63}_{-3.22}$	$16.27^{+4.63}_{-3.22}$	$16.27^{+4.63}_{-3.22}$	$16.27^{+4.63}_{-3.22}$
$\mathcal{O}(\alpha_s^3)$	+21.14	+20.08(3)	+20.08(3)	+20.08(3)	+20.08(3)
NLO	$37.44^{+8.42}_{-6.29}$	$36.35(3)^{+8.57}_{-6.32}$	$36.35(3)^{+8.57}_{-6.32}$	$36.35(3)^{+8.57}_{-6.32}$	$36.35(3)^{+8.57}_{-6.32}$
$\mathcal{O}(\alpha_s^4)$	+9.72	+10.8(4)	+11.1(4)	+9.5(2)	+9.6(2)
NNLO	$47.16^{+4.21}_{-4.77}$	$47.2(4)^{+5.4}_{-5.4}$	$47.5(4)^{+5.4}_{-5.5}$	$45.9(2)^{+4.3}_{-4.9}$	$46.0(2)^{+4.4}_{-5.0}$

Table 6.5: rHTL cross section in the 5-flavour scheme and for different bottom-quark masses in the 4-flavour scheme. In the last column the cross section and the scale variation are computed with the $\overline{\text{MS}}$ -mass. The results are computed for LHC @ 13 TeV using the computational setup is described in the conventions. The scale uncertainties are determined with seven-point variation. Numbers in parentheses indicate the MC uncertainties on the last provided digit. Results computed in the 5FS were computed using **SusHi**.

section level, as there is no strong rise of the cross section for decreasing bottom-quark masses.

We further observe, that the 4FS approach the 5FS results in the limit $m_b \rightarrow 0$. For realistic values of the bottom-quark mass (last two columns in Tab. 6.5), we see a significant change from the 5 to the 4FS of around -2% which is however still well within the associated scale uncertainties. Results for OS and $\overline{\text{MS}}$ renormalized bottom-quark masses show no significant deviations.

To further validate our findings, we compared our p_T -spectra against existing Higgs+jet analysis. The top-bottom interference contribution with OS-renormalized top- and bottom-quark masses was compared to the results presented in Ref. [136]. In that reference, the authors approximate the real-virtual corrections using the HTL for the top-quark, and they work under the assumption of a nearly massless bottom-quark. Fig. 6.3, shows the comparison of the two results. We see that the approximations perform well for a transverse momentum below 40 GeV, but result in an error of about 20% above this threshold. Since the approximation of a nearly massless bottom quark is expected to perform well in the limit $m_b \ll m_H, p_T$, the discrepancy is likely due to the HTL approximation. Since the p_T range $[0, 40 \text{ GeV}]$ is responsible for the majority of the top-bottom interference contribution—about 99%—, the approximation is still highly accurate for the total cross section. Additionally, we observe that the scale uncertainties of the first two-bins are significantly larger in Ref. [136]. We were able to identify that this difference arises only from a single scale variation ($\mu_R/\mu = 1, \mu_F/\mu = 2$), but we have not found any error on our end that would account for this difference.

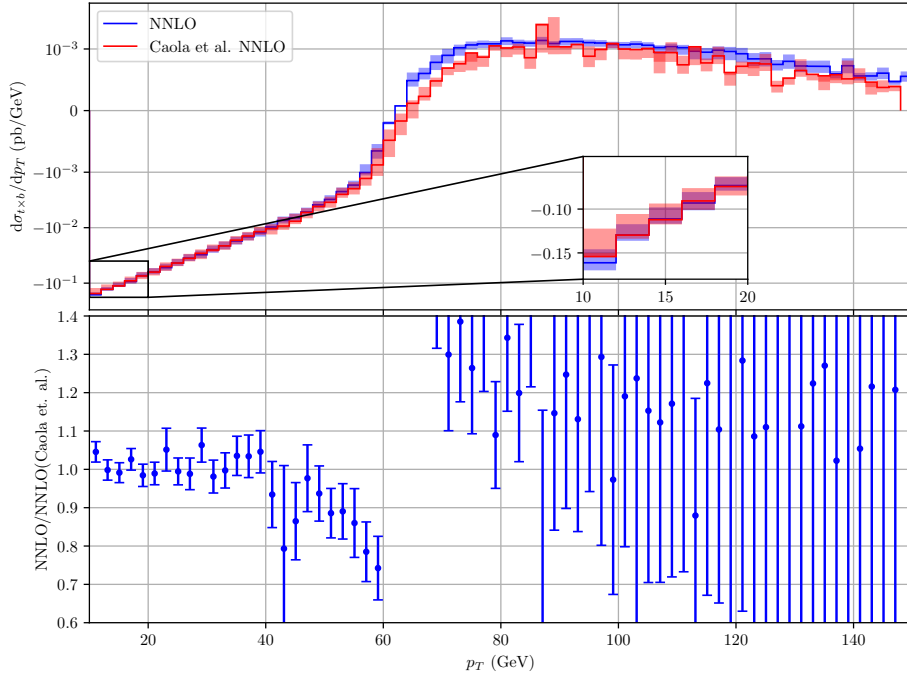


Figure 6.3: Top-bottom interference contribution to the Higgs production cross section. Displayed are our results and the results presented in Ref. [136], with data provided by the authors. The authors of that reference used an OS top- and bottom-quark mass of $m_t = 173.2 \text{ GeV}$, and $m_b = 4.75 \text{ GeV}$, whereas we used $m_t = 173.05 \text{ GeV}$ and $m_b = 4.78 \text{ GeV}$ and the same Higgs mass of $m_H = 125 \text{ GeV}$. For the sake of this comparison we used the same PDF4LHC15_nlo_30 PDF set and a central scale of $\mu = \frac{1}{2}\sqrt{m_H^2 + p_T^2}$. The transparent bands indicate scale uncertainties, whereas the error bars in the lower panel indicate the MC uncertainties dominated by the uncertainties of Ref. [136].

Furthermore, we compared our findings of the pure-top and the top-bottom-interference contribution with both quark-masses defined in the $\overline{\text{MS}}$ scheme with the results presented in Ref. [137]. The results show excellent agreement for transverse momenta $p_T \leq 400$ GeV.

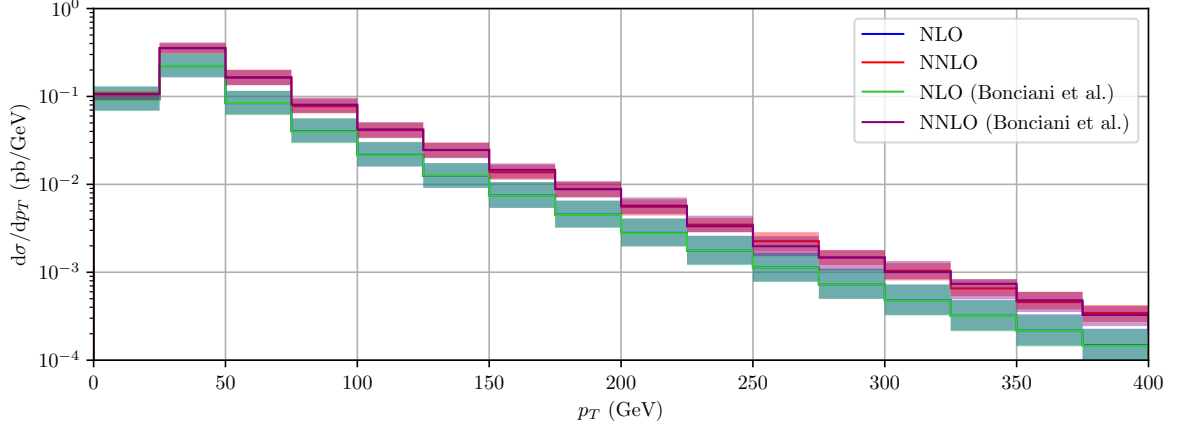


Figure 6.4: Comparison of the differential cross section of the gluon-gluon fusion channel between our findings and the results presented in Ref. [137]. The cross section constitutes the pure-top-quark, the top-bottom interference, and the pure-bottom-quark contribution, we however neglect the pure-bottom-quark contribution for all NNLO corrections. For the sake of this comparison we use the same computational setup as the authors of Ref. [137], namely top- and bottom-quark masses defined in the $\overline{\text{MS}}$ scheme with the masses $\overline{m}_t(\overline{m}_t) = 163.4$ GeV and $\overline{m}_b(\overline{m}_b) = 4.18$ GeV. The running of the quark-masses is computed at two-loop accuracy. The Higgs mass is set to $m_H = 125.25$ GeV. We apply the anti- k_T algorithm with a jet radius of $R = 0.4$ and use the central scale $\mu = \frac{1}{2} \left(\sqrt{m_H^2 + p_T^2} + \sum_i p_{i,T} \right)$, where the sum runs over all jet momenta. We use a p_T -cut on the jets, requiring that at least one of the jets satisfies $p_{i,T} > 20$ GeV. We use the NNPDF40_nlo_as_01180 PDF set.

Above this scale we find significant deviations. We were able to identify, that the problem arises from the real-virtual amplitudes. Indeed, our numerical grids were only computed for top-quark masses up to a scale of $\mu_R = 125$ GeV. If the scale supersedes this value, we are extrapolating from our grid. This then results in large errors for $p_T > 400$ GeV. We stress that all our previous findings did not rely on this extrapolation, since we used fixed scales whenever we renormalized the top-quark mass in the $\overline{\text{MS}}$ scheme.

6.4 RECOMMENDATIONS FOR PHENOMENOLOGICAL APPLICATIONS

We want to conclude this chapter by giving our recommendations for the total gluon-gluon fusion Higgs-production cross section for future phenomenological applications. We combine our findings with the full N³LO rHTL results, the partial N⁴LO results in the soft-virtual approximation, the available electroweak corrections, and the finite top-quark mass effects. The associated uncertainties of each contribution are carefully examined.

Following our discussion of section 4.3.1, we suggest using $\mu = m_H/2$ as the central scale. Further we recommend using the MSHT20xNNPDF40_aN3LO PDF set until full N³LO sets become available.

The top-bottom interference contribution proved to be quite independent of the used FS. We therefore suggest using the 5FS going forward, because large logarithms are automatically resummed in this FS by the running of the PDFs. The renormalization scheme of the top-quark mass also did not affect the cross section significantly. Both the $\overline{\text{MS}}$ and the OS scheme are therefore valid choices. In the following we provide results for the latter. The bottom-quark mass on the other hand, was very sensitive to the renormalization scheme, and the $\overline{\text{MS}}$ scheme showed significantly better perturbative convergence, which is why we strongly recommend using this scheme going forward.

Our best prediction for the gluon-gluon fusion cross section is

$$\begin{aligned}
 \sigma_{pp \rightarrow HX}(13 \text{ TeV}) = & + 15.33 \text{ pb} \quad (+33.17\%) \quad (\text{LO rHTL}) \\
 & + 19.99 \text{ pb} \quad (+43.26\%) \quad (\text{NLO rHTL}) \\
 & + 9.20 \text{ pb} \quad (+19.91\%) \quad (\text{NNLO rHTL}) \\
 & + 1.56 \text{ pb} \quad (+3.38\%) \quad (\text{N}^3\text{LO rHTL}) \\
 & + 0.14 \text{ pb} \quad (+0.30\%) \quad (\text{N}^4\text{LO rHTL in s.v. approx.}) \\
 & + 2.02 \text{ pb} \quad (+4.37\%) \quad (\text{NLO EW-QCD}) \\
 & - 0.16 \text{ pb} \quad (-0.35\%) \quad (\text{NNLO finite top-quark mass}) \\
 & - 0.23 \text{ pb} \quad (-0.50\%) \quad (\text{NLO top-charm interference}) \\
 & + 0.10 \text{ pb} \quad (+0.22\%) \quad (\text{NLO pure bottom-quark effects}) \\
 & - 1.74 \text{ pb} \quad (-3.77\%) \quad (\text{NNLO top-bottom interference}) \\
 \hline
 & 46.21 \text{ pb} \quad (100\%).
 \end{aligned} \tag{6.4}$$

The rHTL results were computed using `iHixs 2`. The N^4LO results were extracted from the K -factor with respect to N^3LO at 13 TeV, provided in Ref. [72]. In that reference they use a slightly altered computational setup, including a different PDF (`MMHT2014`). Since the N^4LO corrections is tiny, the final result should not be affected by this. Similarly, the electroweak corrections were extracted from Ref. [116], where the authors used the `PDF4LHC15_nlo_30` PDF set and slightly different masses for the Higgs, and the top- and bottom-quark⁶. Once again, the electroweak corrections themselves are small, making the impact of a slightly altered computational setup non-essential. Finally, the effects from finite top- and bottom-quark masses were computed using the `NNPDF31_nnlo_as_0118` PDF set.

We estimate the missing higher order uncertainties, based on the μ_R variation⁷ of the N^4LO cross section in the soft-virtual approximation in the range $[m_H/4, m_H]$ presented in Ref. [72]. The factorization scale dependence was shown to be very small (see Fig. 4.11), making this an accurate estimate on missing higher order uncertainties. We do not include uncertainties on the soft-virtual approximation itself, as it is believed to be small compared to the other sources. Uncertainties on the electroweak corrections are also dominated by missing higher order uncertainties, and we adopt the uncertainties assigned in Ref. [116]. Errors associated to missing higher orders in the PDF fits, including the missing ingredients for the DGLAP evolution equation, are estimated by comparing cross section results computed using the `NNPDF40_an3lo_as_01180_mhou` and the `NNPDF40_an3lo_as_01180` PDF set, i.e. the uncertainty is calculated via

$$\delta(\text{PDF MHO}) = \sqrt{\left(\sigma_{gg \rightarrow HX}^{\text{NNPDF40_an3lo_as_01180_mhou}}\right)^2 - \left(\sigma_{gg \rightarrow HX}^{\text{NNPDF40_an3lo_as_01180}}\right)^2}. \tag{6.5}$$

⁶ The authors also used a bottom-quark mass defined in the OS scheme.

⁷ Recently, the missing higher order uncertainties were also estimated using theory nuisance parameters [175] at NNLO. The authors found the uncertainties to be compatible.

This assumes that the PDF-theory and the PDF uncertainties are uncorrelated. Uncertainties for finite quark-mass effects are determined through seven-point scale variation. The full theory uncertainty can be broken down as follows:

$$\begin{aligned}
\delta(\text{theory}) = & \begin{array}{l} +0.10 \\ -1.73 \end{array} \text{ pb } \begin{array}{l} (+0.2\% \\ -3.7\% \end{array} \text{ (scale)} \\
& \pm 0.14 \text{ pb } (\pm 0.3\%) \text{ (electroweak)} \\
& \pm 0.16 \text{ pb } (\pm 0.3\%) \text{ (PDF MHOU)} \\
& \begin{array}{l} +0.13 \\ -0.03 \end{array} \text{ pb } \begin{array}{l} (+0.3\% \\ -0.1\% \end{array} \text{ (finite top-quark mass)} \\
& \begin{array}{l} +0.13 \\ -0.03 \end{array} \text{ pb } \begin{array}{l} (+0.3\% \\ -0.1\% \end{array} \text{ (top-bottom interference)} \\
\hline
& \begin{array}{l} +0.25 \\ -1.73 \end{array} \text{ pb } \begin{array}{l} (+0.5\% \\ -3.8\% \end{array}.
\end{aligned} \tag{6.6}$$

For the final theory uncertainty, we added all individual errors in quadrature. In section 4.3.5 we observed, that the top-bottom interference contribution is actually anti-correlated with the pure-top quark contribution. We do not take this anti-correlation into account here, because the correlations among the other sources of uncertainty are currently unavailable. The uncertainty estimates are slightly different from the upcoming Higgs Working Group recommendation [176], mainly due to the fact that electroweak corrections are not incorporated with full NLO precision. Furthermore, the Higgs Working Group assumes maximal correlation between the various uncertainties. The uncertainty estimates presented here are therefore smaller by approximately 1% of the total cross section.

Finally, the uncertainties on the PDF sets are combined with the α_s uncertainties, assuming that the errors are uncorrelated. This not entirely realistic assumption, is adopted out of necessity, since the **MSHT20xNNPDF40_aN3LO** PDF set does not support correlations yet. The α_s -uncertainty is estimated by reevaluation of the N³LO rHTL cross section at $\alpha_s(m_Z) = 0.117$ and $\alpha_s(m_Z) = 0.119$, corresponding to the standard deviation of α_s [177], the resulting range is taken as the standard deviation. The combined uncertainty reads

$$\begin{aligned}
\delta(\text{PDF} + \alpha_s) &= \sqrt{[\delta(\text{PDF})]^2 + [\delta(\alpha_s)]^2} = \sqrt{[0.88 \text{ pb } (1.9\%)]^2 + \left[\begin{array}{l} +1.23 \\ -1.21 \end{array} \text{ pb } \begin{array}{l} (+2.6\% \\ -2.6\% \end{array} \right]^2} \\
&= \begin{array}{l} +1.52 \\ -1.50 \end{array} \text{ pb } \begin{array}{l} (+3.3\% \\ -3.2\% \end{array}.
\end{aligned} \tag{6.7}$$

Our final best prediction for the gluon-gluon fusion cross at 13 TeV is

$$\boxed{\sigma_{pp \rightarrow HX}(13 \text{ TeV}) = 46.21_{-1.73}^{+0.25} \text{ (theory)} \begin{array}{l} +1.52 \\ -1.50 \end{array} \text{ (PDF} + \alpha_s \text{) pb.}} \tag{6.8}$$

7 | CONCLUSIONS

Here are my conclusions.

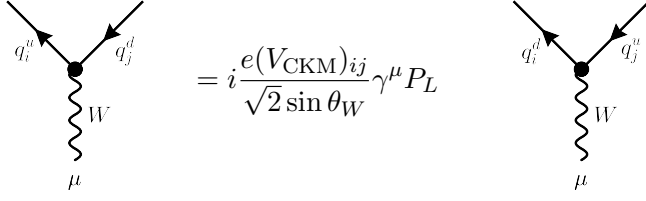
In this chapter we list all Feynman rules of the SM. We choose to work in a unitary gauge, meaning that the all Goldstone-bosons decouple and there are no unphysical particles in the electroweak sector. In the QCD sector, we work in the R_ξ gauge, i.e. we have unphysical particles in the form of *Faddeev-Popov ghosts*. If not otherwise specified, the momenta on every line are defined as incoming.

Propagators:

$$\begin{aligned}
 a, \mu \quad \text{---} \overline{\text{---}} \overline{\text{---}} \overline{\text{---}} \overline{\text{---}} \overline{\text{---}} \overline{\text{---}} \overline{\text{---}} \overline{\text{---}} \text{---} \quad b, \nu &= i \frac{\delta^{ab}}{k^2 + i0^+} \left[-g_{\mu\nu} + (1 - \xi) \frac{k_\mu k_\nu}{k^2 + i0^+} \right] \\
 i \quad \text{---} \overline{\text{---}} \overline{\text{---}} \overline{\text{---}} \overline{\text{---}} \overline{\text{---}} \overline{\text{---}} \overline{\text{---}} \text{---} \quad j &= i \delta_{ij} \frac{\not{k} + m}{k^2 - m^2 + i0^+} \\
 \text{---} \overline{\text{---}} \overline{\text{---}} \overline{\text{---}} \overline{\text{---}} \overline{\text{---}} \overline{\text{---}} \overline{\text{---}} \text{---} &= i \frac{1}{k^2 - m_H^2 + i0^+} \\
 \mu \quad \text{---} \overline{\text{---}} \overline{\text{---}} \overline{\text{---}} \overline{\text{---}} \overline{\text{---}} \overline{\text{---}} \overline{\text{---}} \text{---} \quad \nu &= i \frac{-g_{\mu\nu}}{k^2 + i0^+} \\
 \mu \quad \text{---} \overline{\text{---}} \overline{\text{---}} \overline{\text{---}} \overline{\text{---}} \overline{\text{---}} \overline{\text{---}} \overline{\text{---}} \text{---} \quad \nu &= i \frac{1}{k^2 - m_W^2 + i0^+} \left(-g_{\mu\nu} + \frac{k_\mu k_\nu}{m_W^2 + i0^+} \right) \\
 \mu \quad \text{---} \overline{\text{---}} \overline{\text{---}} \overline{\text{---}} \overline{\text{---}} \overline{\text{---}} \overline{\text{---}} \overline{\text{---}} \text{---} \quad \nu &= i \frac{1}{k^2 - m_Z^2 + i0^+} \left(-g_{\mu\nu} + \frac{k_\mu k_\nu}{m_Z^2 + i0^+} \right) \\
 a \quad \text{---} \overline{\text{---}} \overline{\text{---}} \overline{\text{---}} \overline{\text{---}} \overline{\text{---}} \overline{\text{---}} \overline{\text{---}} \text{---} \quad b &= i \frac{\delta^{ab}}{k^2 + i0^+}
 \end{aligned}$$

Fermion–Gauge-Boson Vertices:

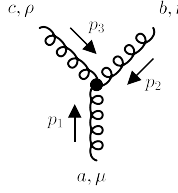
$$\begin{aligned}
 \begin{array}{c} i \\ \swarrow \\ \bullet \\ \searrow \\ j \\ \downarrow \\ a, \mu \end{array} &= ig \gamma^\mu T_{ij}^a \\
 \begin{array}{c} \swarrow \\ \bullet \\ \searrow \\ \downarrow \\ \mu \end{array} &= -ie \gamma^\mu Q \\
 \begin{array}{c} a \\ \swarrow \\ \bullet \\ \searrow \\ b \\ \downarrow \\ c, \mu \end{array} &= g f^{abc} p^\mu \\
 \begin{array}{c} \swarrow \\ \bullet \\ \searrow \\ \downarrow \\ \mu \end{array} &= i \frac{e}{\sin \theta_W \cos \theta_W} \gamma^\mu \times (I^3 P_L - Q \sin^2 \theta_W)
 \end{aligned}$$



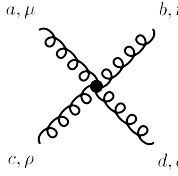
$$= i \frac{e(V_{\text{CKM}})_{ij}}{\sqrt{2} \sin \theta_W} \gamma^\mu P_L$$

$$= i \frac{e(V_{\text{CKM}})^*_{ji}}{\sqrt{2} \sin \theta_W} \gamma^\mu P_L$$

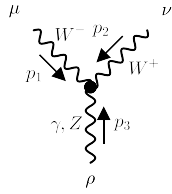
Gauge-Boson Self Interactions:



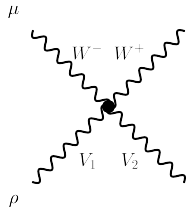
$$= g f^{abc} ((p_1^\rho - p_2^\rho) g^{\mu\nu} + (p_2^\mu - p_3^\mu) g^{\nu\rho} + (p_3^\nu - p_1^\nu) g^{\rho\mu})$$



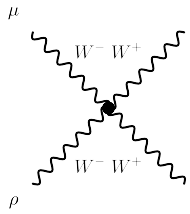
$$= -ig^2 (f^{abe} f^{cde} (g^{\mu\rho} g^{\nu\sigma} - g^{\mu\sigma} g^{\nu\rho}) + f^{ace} f^{bde} (g^{\mu\nu} g^{\rho\sigma} - g^{\mu\sigma} g^{\nu\rho}) + f^{ade} f^{bce} (g^{\mu\nu} g^{\rho\sigma} - g^{\mu\rho} g^{\nu\sigma}))$$



$$= i \frac{e}{\sin \theta_W} ((p_1^\rho - p_2^\rho) g^{\mu\nu} + (p_2^\mu - p_3^\mu) g^{\nu\rho} + (p_3^\nu - p_1^\nu) g^{\rho\mu}) \times \begin{cases} -\sin \theta_W & \text{for } \gamma \\ \cos \theta_W & \text{for } Z \end{cases}$$



$$= i \frac{e^2}{\sin^2 \theta_W} (g^{\mu\sigma} g^{\nu\rho} + g^{\mu\rho} g^{\nu\sigma} - 2g^{\mu\nu} g^{\rho\sigma}) \times \prod_{i=1}^2 \begin{cases} -\sin \theta_W & \text{if } V_i = \gamma \\ \cos \theta_W & \text{if } V_i = Z \end{cases}$$



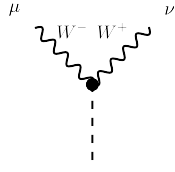
$$= i \frac{e^2}{\sin^2 \theta_W} (2g^{\mu\rho} g^{\nu\sigma} - g^{\mu\nu} g^{\rho\sigma} - g^{\mu\sigma} g^{\nu\rho})$$

Higgs Interactions:

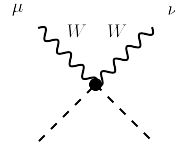


$$= -i \frac{m_q}{v} \delta_{ij}$$

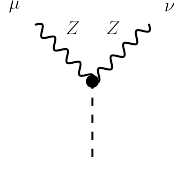

$$= -i \frac{3m_H^2}{v}$$



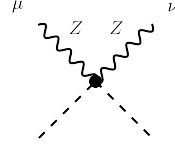
$$= i \frac{e}{\sin \theta_W} m_W g^{\mu\nu}$$



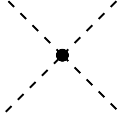
$$= i \frac{e^2}{2 \sin^2 \theta_W} g^{\mu\nu}$$



$$= i \frac{e}{\sin \theta_W \cos \theta_W} m_Z g^{\mu\nu}$$



$$= i \frac{e^2}{2 \sin^2 \theta_W \cos^2 \theta_W} g^{\mu\nu}$$



$$= -i \frac{3m_H^2}{v^2}$$

B | FEYNMAN INTEGRALS

In this appendix we collect some common one-loop Feynman integrals which appear frequently throughout this PhD thesis.

Bubble

We define the function $B(p^2)$ as the finite part of the bubble integral

$$B(p^2) = 2 - \log\left(\frac{m^2}{\mu^2}\right) + \beta(p^2, m^2) \log\left(-\frac{1 - \beta(p^2, m^2)}{1 + \beta(p^2, m^2)} + i0^+\right). \quad (\text{B.1})$$

The function $\beta(s, m^2)$ is defined in Eq. (5.28). We further define

$$B_1(p^2) \equiv B(p^2) - B(m_H^2). \quad (\text{B.2})$$

Triangle

The one-loop on-shell triangle integral is

$$C(s) = C(p_1, p_2) = \frac{1}{2s} \log^2\left(-\frac{1 - \beta(p^2, m^2)}{1 + \beta(p^2, m^2)} + i0^+\right). \quad (\text{B.3})$$

The triangle integral with one off-shell leg is related via

$$s_1 C_1(s) \equiv sC(s) - m_H^2 C(m_H^2). \quad (\text{B.4})$$

Box

The one-loop box integral reads

$$\begin{aligned} D(s, t) &= D(p_1, p_2, p_3) \\ &= \int \frac{d^4 l}{i\pi^2} \frac{1}{[l^2 - m^2][(l + p_1)^2 - m^2][(l + p_1 + p_2)^2 - m^2][(l + p_1 + p_2 + p_3)^2 - m^2]} \\ &= -\frac{2}{st\beta(st/u, m^2)} \left\{ \text{Li}_2\left(\frac{1 - \beta(st/u, m^2)}{-\beta(st/u, m^2) - \beta(m_H^2, m^2 - i0^+)}\right) \right. \\ &\quad - \text{Li}_2\left(\frac{1 + \beta(st/u, m^2)}{\beta(st/u, m^2) - \beta(m_H^2, m^2 - i0^+)}\right) + \text{Li}_2\left(\frac{1 - \beta(st/u, m^2)}{\beta(m_H^2, m^2 - i0^+) - \beta(st/u, m^2)}\right) \\ &\quad - \text{Li}_2\left(\frac{1 + \beta(st/u, m^2)}{\beta(m_H^2, m^2 - i0^+) + \beta(st/u, m^2)}\right) \\ &\quad + \log\left(-\frac{1 - \beta(st/u, m^2)}{\beta(st/u, m^2) + 1}\right) \log\left(1 - \frac{m_H^2}{4m^2}(1 - \beta^2(st/u, m^2) - i0^+)\right) \\ &\quad \left. - (m_H^2 \rightarrow s) - (m_H^2 \rightarrow t) \right\} \end{aligned} \quad (\text{B.5})$$

where $p_1^2 = p_2^2 = p_3^2 = 0$. We further define the auxiliary function

$$E(u, t) = uC(u) + tC(t) + u_1 C_1(u) + t_1 C(t) - utD(u, t). \quad (\text{B.6})$$

C

ENERGY SCAN OF THE TOP-BOTTOM
INTERFERENCE CONTRIBUTION

In this appendix we provide additional results on the top-bottom interference contribution to the gluon-gluon fusion cross section. Specifically we provide the results for collider energies of 7, 8, 13, 13.6, and 14 TeV. In Tab. C.1 we present the results computed with a setup according to Higgs-Working-Group recommendations. Tab. ?? show the results for an OS renormalized bottom-quark mass, as well as the results for a mixed renormalization scheme, where the bottom-quark Yukawa coupling has been renormalized in the $\overline{\text{MS}}$ -scheme.

	7 TeV	8 TeV	13 TeV	13.6 TeV	14 TeV
LO	$-0.39^{+0.10}_{-0.15}$ pb	$-0.50^{+0.12}_{-0.19}$ pb	$-1.09^{+0.27}_{-0.42}$ pb	$-1.17^{+0.29}_{-0.45}$ pb	$-1.22^{+0.31}_{-0.47}$ pb
NLO	$-0.66^{+0.11}_{-0.12}$ pb	$-0.82^{+0.13}_{-0.14}$ pb	$-1.72^{+0.26}_{-0.27}$ pb	$-1.84^{+0.28}_{-0.29}$ pb	$-1.91^{+0.29}_{-0.30}$ pb
NNLO	$-0.68^{+0.06}_{-0.02}$ pb	$-0.84^{+0.07}_{-0.01}$ pb	$-1.70^{+0.13}_{-0.01}$ pb	$-1.80^{+0.13}_{-0.01}$ pb	$-1.88^{+0.13}_{-0.01}$ pb

Table C.1: Top-Bottom interference contribution to the fully-inclusive Higgs-production cross section for different collider energies and perturbative orders. Top-quark mass is renormalized in the OS-scheme with a pole mass of $m_t = 172.5$ GeV, except in the real-virtual corrections where we use a mass of $m_t = 173.18$ GeV. We reevaluated this contribution with a value of $m_t = 171.1$ GeV and found that the difference is below our MC uncertainties. The bottom-quark mass is renormalized in the $\overline{\text{MS}}$ -scheme with a mass of $\overline{m}_b(\overline{m}_b) = 4.18$ GeV. The Higgs mass was chosen as $m_H = 125.09$ GeV. The results were computed using the PDF4LHC21_40 PDF set. The scale uncertainties are determined with seven-point variation.

Order	$\sigma_{t \times b}$ [pb]	$\sigma_{t \times b}(Y_{b, \overline{\text{MS}}})$ [pb]	$\sigma_{t \times b}/\sigma_{\text{HEFT}}$ [%]
$\sqrt{s} = 7 \text{ TeV}$			
$\mathcal{O}(\alpha_s^2)$	-0.708	-0.439	
LO	$-0.708^{+0.13}_{-0.19}$	$-0.439^{+0.10}_{-0.16}$	-12
$\mathcal{O}(\alpha_s^3)$	-0.226	-0.264	
NLO	$-0.934^{+0.09}_{-0.07}$	$-0.703^{+0.11}_{-0.12}$	$-7.2^{+1.0}_{-0.8}$
$\mathcal{O}(\alpha_s^4)$	+0.121(3)	-0.026(2)	
NNLO	$-0.813(3)^{+0.10}_{-0.04}$	$-0.729(2)^{+0.04}_{-0.01}$	$-5.0^{+1.0}_{-0.8}$
$\sqrt{s} = 8 \text{ TeV}$			
$\mathcal{O}(\alpha_s^2)$	-0.895	-0.554	
LO	$-0.895^{+0.17}_{-0.24}$	$-0.554^{+0.13}_{-0.20}$	-12
$\mathcal{O}(\alpha_s^3)$	-0.268	-0.323	
NLO	$-1.163^{+0.10}_{-0.08}$	$-0.877^{+0.13}_{-0.14}$	$-7.0^{+1.0}_{-0.8}$
$\mathcal{O}(\alpha_s^4)$	+0.167(3)	-0.022(2)	
NNLO	$-0.996(3)^{+0.12}_{-0.05}$	$-0.899(2)^{+0.04}_{-0.02}$	$-4.8^{+0.9}_{-0.8}$
$\sqrt{s} = 13 \text{ TeV}$			
$\mathcal{O}(\alpha_s^2)$	-1.975	-1.223	
LO	$-1.98^{+0.38}_{-0.53}$	$-1.22^{+0.29}_{-0.44}$	-12
$\mathcal{O}(\alpha_s^3)$	-0.446(1)	-0.623(1)	
NLO	$-2.42^{+0.19}_{-0.12}$	$-1.85^{+0.26}_{-0.26}$	$-6.5^{+0.9}_{-0.8}$
$\mathcal{O}(\alpha_s^4)$	+0.434(8)	+0.019(5)	
NNLO	$-1.99(1)^{+0.30}_{-0.15}$	$-1.83(1)^{+0.08}_{-0.03}$	$-4.2^{+0.9}_{-0.8}$
$\sqrt{s} = 13.6 \text{ TeV}$			
$\mathcal{O}(\alpha_s^2)$	-2.117	-1.311	
LO	$-2.12^{+0.40}_{-0.57}$	$-1.31^{+0.31}_{-0.47}$	-12
$\mathcal{O}(\alpha_s^3)$	-0.464(1)	-0.659(1)	
NLO	$-2.58^{+0.20}_{-0.12}$	$-1.97^{+0.28}_{-0.28}$	$-6.4^{+0.9}_{-0.8}$
$\mathcal{O}(\alpha_s^4)$	+0.464(9)	+0.022(6)	
NNLO	$-2.12(1)^{+0.33}_{-0.16}$	$-1.95(1)^{+0.09}_{-0.03}$	$-4.2^{+0.9}_{-0.8}$
$\sqrt{s} = 14 \text{ TeV}$			
$\mathcal{O}(\alpha_s^2)$	-2.213	-1.370	
LO	$-2.21^{+0.42}_{-0.59}$	$-1.37^{+0.32}_{-0.49}$	-12
$\mathcal{O}(\alpha_s^3)$	-0.475(1)	-0.682(1)	
NLO	$-2.69^{+0.21}_{-0.13}$	$-2.05^{+0.29}_{-0.29}$	$-6.4^{+0.9}_{-0.8}$
$\mathcal{O}(\alpha_s^4)$	+0.488(9)	+0.027(6)	
NNLO	$-2.20(1)^{+0.34}_{-0.17}$	$-2.03(1)^{+0.09}_{-0.03}$	$-4.1^{+0.9}_{-0.8}$

Table C.2: Top-bottom interference contribution to the gluon-gluon fusion cross section for top- and bottom-quark masses defined in the OS-scheme, and in a mixed scheme, where the bottom-quark Yukawa coupling is renormalized in the $\overline{\text{MS}}$ -scheme. The results are computed for LHC @ 7,8,13,13.6 and 14 TeV using the computational setup is described in the conventions. The scale uncertainties are determined with seven-point variation. Numbers in parentheses indicate the MC uncertainties on the last provided digit.

D

ON-SHELL RESULTS FOR THE DIFFERENTIAL CROSS SECTION

Here we present the results for the Higgs-transverse momentum and -rapidity spectra with the bottom-quark mass defined in the OS scheme. Since the relevant discrepancies between the

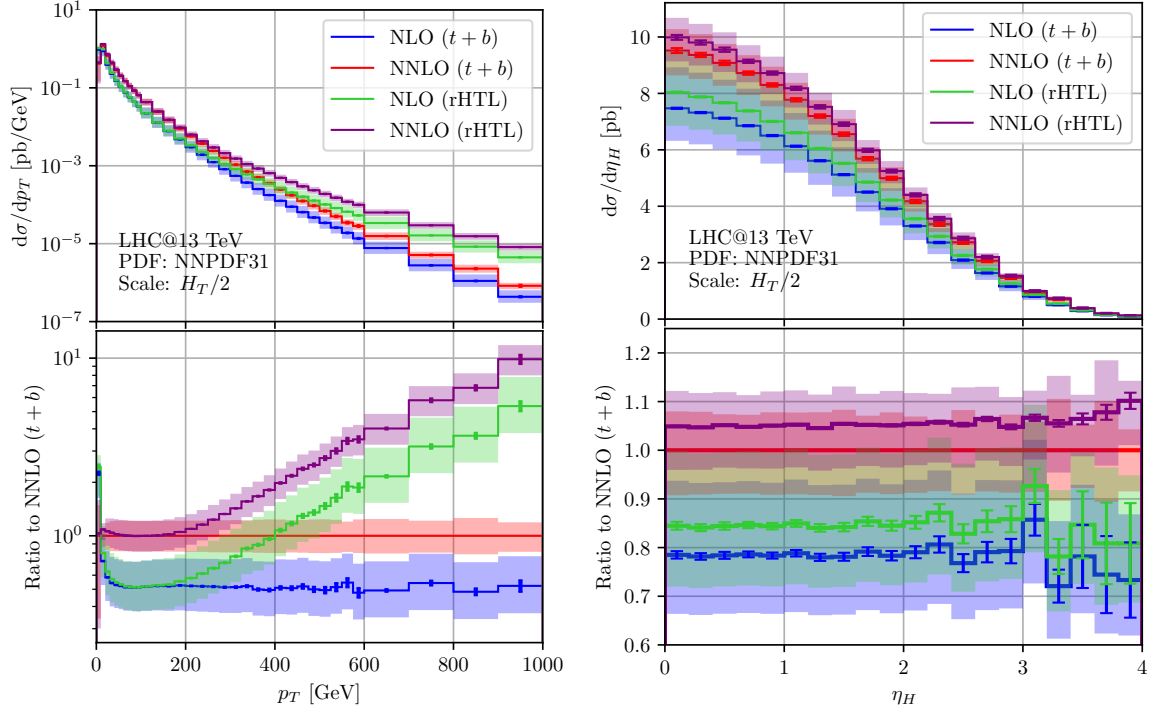


Figure D.1: Same as in Fig. 6.2 but for an OS renormalized bottom-quark mass.

OS and the $\overline{\text{MS}}$ scheme were limited to $p_T < 40$ GeV, and even here the differences were mild, the spectra are effectively identical to the ones presented in Fig. 6.2.

BIBLIOGRAPHY

- [1] Michał Czakon, Felix Schment, and Tom Schellenberger. “Revisiting the double-soft asymptotics of one-loop amplitudes in massless QCD.” In: *JHEP* 04 (2023), p. 065. DOI: [10.1007/JHEP04\(2023\)065](#). arXiv: [2211.06465 \[hep-ph\]](#).
- [2] Michał Czakon, Felix Schment, and Tom Schellenberger. “Subleading effects in soft-gluon emission at one-loop in massless QCD.” In: *JHEP* 12 (2023), p. 126. DOI: [10.1007/JHEP12\(2023\)126](#). arXiv: [2307.02286 \[hep-ph\]](#).
- [3] Michał Czakon et al. “Top-Bottom Interference Contribution to Fully Inclusive Higgs Production.” In: *Phys. Rev. Lett.* 132.21 (2024), p. 211902. DOI: [10.1103/PhysRevLett.132.211902](#). arXiv: [2312.09896 \[hep-ph\]](#).
- [4] Michał Czakon et al. “Quark mass effects in Higgs production.” In: *JHEP* 10 (2024), p. 210. DOI: [10.1007/JHEP10\(2024\)210](#). arXiv: [2407.12413 \[hep-ph\]](#).
- [5] Izaak Neutelings. *Izaak neutelings*. Mar. 2024. URL: https://tikz.net/sm_particles/.
- [6] Stefan Weinzierl. *Feynman Integrals. A Comprehensive Treatment for Students and Researchers*. UNITEXT for Physics. Springer, 2022. ISBN: 978-3-030-99557-7, 978-3-030-99560-7, 978-3-030-99558-4. DOI: [10.1007/978-3-030-99558-4](#). arXiv: [2201.03593 \[hep-th\]](#).
- [7] Gerard 't Hooft. “Renormalizable Lagrangians for Massive Yang-Mills Fields.” In: *Nucl. Phys. B* 35 (1971). Ed. by J. C. Taylor, pp. 167–188. DOI: [10.1016/0550-3213\(71\)90139-8](#).
- [8] Gerard 't Hooft and M. J. G. Veltman. “Regularization and Renormalization of Gauge Fields.” In: *Nucl. Phys. B* 44 (1972), pp. 189–213. DOI: [10.1016/0550-3213\(72\)90279-9](#).
- [9] Andy Buckley et al. “LHAPDF6: parton density access in the LHC precision era.” In: *Eur. Phys. J. C* 75 (2015), p. 132. DOI: [10.1140/epjc/s10052-015-3318-8](#). arXiv: [1412.7420 \[hep-ph\]](#).
- [10] Richard D. Ball et al. “Parton distributions from high-precision collider data.” In: *Eur. Phys. J. C* 77.10 (2017), p. 663. DOI: [10.1140/epjc/s10052-017-5199-5](#). arXiv: [1706.00428 \[hep-ph\]](#).
- [11] John C. Collins, Davison E. Soper, and George F. Sterman. “Factorization of Hard Processes in QCD.” In: *Adv. Ser. Direct. High Energy Phys.* 5 (1989), pp. 1–91. DOI: [10.1142/9789814503266_0001](#). arXiv: [hep-ph/0409313](#).
- [12] Yuri L. Dokshitzer. “Calculation of the Structure Functions for Deep Inelastic Scattering and e^+e^- Annihilation by Perturbation Theory in Quantum Chromodynamics.” In: *Sov. Phys. JETP* 46 (1977), pp. 641–653.
- [13] V. N. Gribov and L. N. Lipatov. “Deep inelastic $e p$ scattering in perturbation theory.” In: *Sov. J. Nucl. Phys.* 15 (1972), pp. 438–450.
- [14] Guido Altarelli and G. Parisi. “Asymptotic Freedom in Parton Language.” In: *Nucl. Phys. B* 126 (1977), pp. 298–318. DOI: [10.1016/0550-3213\(77\)90384-4](#).

- [15] T. Kinoshita and A. Ukawa. “Mass Singularities of Feynman Amplitudes.” In: *Lect. Notes Phys.* 39 (1975). Ed. by Huzihiro Araki, pp. 55–58. DOI: [10.1007/BFb0013300](#).
- [16] T. D. Lee and M. Nauenberg. “Degenerate Systems and Mass Singularities.” In: *Phys. Rev.* 133 (1964). Ed. by G. Feinberg, B1549–B1562. DOI: [10.1103/PhysRev.133.B1549](#).
- [17] Charalampos Anastasiou and Kirill Melnikov. “Higgs boson production at hadron colliders in NNLO QCD.” In: *Nucl. Phys. B* 646 (2002), pp. 220–256. DOI: [10.1016/S0550-3213\(02\)00837-4](#). arXiv: [hep-ph/0207004](#).
- [18] Falko Dulat et al. “Higgs-differential cross section at NNLO in dimensional regularisation.” In: *JHEP* 07 (2017), p. 017. DOI: [10.1007/JHEP07\(2017\)017](#). arXiv: [1704.08220 \[hep-ph\]](#).
- [19] Markus A. Ebert, Bernhard Mistlberger, and Gherardo Vita. “ N -jettiness beam functions at N³LO.” In: *JHEP* 09 (2020), p. 143. DOI: [10.1007/JHEP09\(2020\)143](#). arXiv: [2006.03056 \[hep-ph\]](#).
- [20] Daniel Baranowski et al. “Zero-jettiness soft function to third order in perturbative QCD.” In: (Sept. 2024). arXiv: [2409.11042 \[hep-ph\]](#).
- [21] Daniel Baranowski et al. “Triple real-emission contribution to the zero-jettiness soft function at N³LO in QCD.” In: (Dec. 2024). arXiv: [2412.14001 \[hep-ph\]](#).
- [22] John M. Campbell et al. “The NNLO QCD soft function for 1-jettiness.” In: *Eur. Phys. J. C* 78.3 (2018), p. 234. DOI: [10.1140/epjc/s10052-018-5732-1](#). arXiv: [1711.09984 \[hep-ph\]](#).
- [23] Thomas Becher and Guido Bell. “The gluon jet function at two-loop order.” In: *Phys. Lett. B* 695 (2011), pp. 252–258. DOI: [10.1016/j.physletb.2010.11.036](#). arXiv: [1008.1936 \[hep-ph\]](#).
- [24] Thomas Becher and Matthias Neubert. “Toward a NNLO calculation of the anti- $B \rightarrow X(s)$ gamma decay rate with a cut on photon energy. II. Two-loop result for the jet function.” In: *Phys. Lett. B* 637 (2006), pp. 251–259. DOI: [10.1016/j.physletb.2006.04.046](#). arXiv: [hep-ph/0603140](#).
- [25] Radja Boughezal, Xiaohui Liu, and Frank Petriello. “ N -jettiness soft function at next-to-next-to-leading order.” In: *Phys. Rev. D* 91.9 (2015), p. 094035. DOI: [10.1103/PhysRevD.91.094035](#). arXiv: [1504.02540 \[hep-ph\]](#).
- [26] Michał Czakon et al. “Single-jet inclusive rates with exact color at $\mathcal{O}(\alpha_s^4)$.” In: *JHEP* 10 (2019), p. 262. DOI: [10.1007/JHEP10\(2019\)262](#). arXiv: [1907.12911 \[hep-ph\]](#).
- [27] M. Czakon. “A novel subtraction scheme for double-real radiation at NNLO.” In: *Phys. Lett. B* 693 (2010), pp. 259–268. DOI: [10.1016/j.physletb.2010.08.036](#). arXiv: [1005.0274 \[hep-ph\]](#).
- [28] Marco Cirelli, Alessandro Strumia, and Jure Zupan. “Dark Matter.” In: (June 2024). arXiv: [2406.01705 \[hep-ph\]](#).
- [29] Giorgio Arcadi, Abdelhak Djouadi, and Martti Raidal. “Dark Matter through the Higgs portal.” In: *Phys. Rept.* 842 (2020), pp. 1–180. DOI: [10.1016/j.physrep.2019.11.003](#). arXiv: [1903.03616 \[hep-ph\]](#).
- [30] Abdelhak Djouadi et al. “Implications of LHC searches for Higgs–portal dark matter.” In: *Phys. Lett. B* 709 (2012), pp. 65–69. DOI: [10.1016/j.physletb.2012.01.062](#). arXiv: [1112.3299 \[hep-ph\]](#).

- [31] M. Aaboud et al. “Search for an invisibly decaying Higgs boson or dark matter candidates produced in association with a Z boson in pp collisions at $\sqrt{s} = 13$ TeV with the ATLAS detector.” In: *Phys. Lett. B* 776 (2018), pp. 318–337. DOI: [10.1016/j.physletb.2017.11.049](#). arXiv: [1708.09624 \[hep-ex\]](#).
- [32] Vardan Khachatryan et al. “Searches for invisible decays of the Higgs boson in pp collisions at $\sqrt{s} = 7, 8$, and 13 TeV.” In: *JHEP* 02 (2017), p. 135. DOI: [10.1007/JHEP02\(2017\)135](#). arXiv: [1610.09218 \[hep-ex\]](#).
- [33] Georges Aad et al. “Measurements of the Higgs boson production and decay rates and constraints on its couplings from a combined ATLAS and CMS analysis of the LHC pp collision data at $\sqrt{s} = 7$ and 8 TeV.” In: *JHEP* 08 (2016), p. 045. DOI: [10.1007/JHEP08\(2016\)045](#). arXiv: [1606.02266 \[hep-ex\]](#).
- [34] Georges Aad et al. “Search for Invisible Decays of a Higgs Boson Produced in Association with a Z Boson in ATLAS.” In: *Phys. Rev. Lett.* 112 (2014), p. 201802. DOI: [10.1103/PhysRevLett.112.201802](#). arXiv: [1402.3244 \[hep-ex\]](#).
- [35] A. Liss and J. Nielsen. “Physics at a High-Luminosity LHC with ATLAS.” In: (July 2013). Ed. by Norman A. Graf, Michael E. Peskin, and Jonathan L. Rosner. arXiv: [1307.7292 \[hep-ex\]](#).
- [36] “Projected Performance of an Upgraded CMS Detector at the LHC and HL-LHC: Contribution to the Snowmass Process.” In: *Snowmass 2013: Snowmass on the Mississippi*. July 2013. arXiv: [1307.7135 \[hep-ex\]](#).
- [37] M. Cepeda et al. “Report from Working Group 2: Higgs Physics at the HL-LHC and HE-LHC.” In: *CERN Yellow Rep. Monogr.* 7 (2019). Ed. by Andrea Dainese et al., pp. 221–584. DOI: [10.23731/CYRM-2019-007.221](#). arXiv: [1902.00134 \[hep-ph\]](#).
- [38] Armen Tumasyan et al. “A portrait of the Higgs boson by the CMS experiment ten years after the discovery.” In: *Nature* 607.7917 (2022). [Erratum: *Nature* 623, (2023)], pp. 60–68. DOI: [10.1038/s41586-022-04892-x](#). arXiv: [2207.00043 \[hep-ex\]](#).
- [39] Georges Aad et al. “Observation of a new particle in the search for the Standard Model Higgs boson with the ATLAS detector at the LHC.” In: *Phys. Lett. B* 716 (2012), pp. 1–29. DOI: [10.1016/j.physletb.2012.08.020](#). arXiv: [1207.7214 \[hep-ex\]](#).
- [40] Serguei Chatrchyan et al. “Observation of a New Boson at a Mass of 125 GeV with the CMS Experiment at the LHC.” In: *Phys. Lett. B* 716 (2012), pp. 30–61. DOI: [10.1016/j.physletb.2012.08.021](#). arXiv: [1207.7235 \[hep-ex\]](#).
- [41] H. M. Georgi et al. “Higgs Bosons from Two Gluon Annihilation in Proton Proton Collisions.” In: *Phys. Rev. Lett.* 40 (1978), p. 692. DOI: [10.1103/PhysRevLett.40.692](#).
- [42] M. Czakon and D. Heymes. “Four-dimensional formulation of the sector-improved residue subtraction scheme.” In: *Nucl. Phys. B* 890 (2014), pp. 152–227. DOI: [10.1016/j.nuclphysb.2014.11.006](#). arXiv: [1408.2500 \[hep-ph\]](#).
- [43] Michał Czakon and Marco Niggetiedt. “Exact quark-mass dependence of the Higgs-gluon form factor at three loops in QCD.” In: *JHEP* 05 (2020), p. 149. DOI: [10.1007/JHEP05\(2020\)149](#). arXiv: [2001.03008 \[hep-ph\]](#).
- [44] S. Dawson. “Radiative corrections to Higgs boson production.” In: *Nucl. Phys. B* 359 (1991), pp. 283–300. DOI: [10.1016/0550-3213\(91\)90061-2](#).
- [45] H. Kluberg-Stern and J. B. Zuber. “Ward Identities and Some Clues to the Renormalization of Gauge Invariant Operators.” In: *Phys. Rev. D* 12 (1975), pp. 467–481. DOI: [10.1103/PhysRevD.12.467](#).

- [46] Satish D. Joglekar and Benjamin W. Lee. “General Theory of Renormalization of Gauge Invariant Operators.” In: *Annals Phys.* 97 (1976), p. 160. DOI: [10.1016/0003-4916\(76\)90225-6](#).
- [47] Marc Henneaux, Axel Kleinschmidt, and Gustavo Lucena Gómez. “Remarks on Gauge Invariance and First-class Constraints.” In: *Ann. U. Craiova Phys.* 21 (2011), S1–S10.
- [48] David J. Gross and Frank Wilczek. “Ultraviolet Behavior of Nonabelian Gauge Theories.” In: *Phys. Rev. Lett.* 30 (1973). Ed. by J. C. Taylor, pp. 1343–1346. DOI: [10.1103/PhysRevLett.30.1343](#).
- [49] H. David Politzer. “Reliable Perturbative Results for Strong Interactions?” In: *Phys. Rev. Lett.* 30 (1973). Ed. by J. C. Taylor, pp. 1346–1349. DOI: [10.1103/PhysRevLett.30.1346](#).
- [50] *Proceedings, Colloquium on Renormalization of Yang-Mills Fields, Marseille, June 19-23, 1972*. 1972.
- [51] William E. Caswell. “Asymptotic Behavior of Nonabelian Gauge Theories to Two Loop Order.” In: *Phys. Rev. Lett.* 33 (1974), p. 244. DOI: [10.1103/PhysRevLett.33.244](#).
- [52] D. R. T. Jones. “Two Loop Diagrams in Yang-Mills Theory.” In: *Nucl. Phys. B* 75 (1974), p. 531. DOI: [10.1016/0550-3213\(74\)90093-5](#).
- [53] E. Egorian and O. V. Tarasov. “Two Loop Renormalization of the QCD in an Arbitrary Gauge.” In: *Teor. Mat. Fiz.* 41 (1979), pp. 26–32.
- [54] Bernd A. Kniehl and Michael Spira. “Two loop $O(\alpha_s G(F) m(t)^2)$ correction to the $H \rightarrow b\bar{b}$ decay rate.” In: *Nucl. Phys. B* 432 (1994), pp. 39–48. DOI: [10.1016/0550-3213\(94\)90592-4](#). arXiv: [hep-ph/9410319](#).
- [55] Bernd A. Kniehl and Michael Spira. “Low-energy theorems in Higgs physics.” In: *Z. Phys. C* 69 (1995), pp. 77–88. DOI: [10.1007/s002880050007](#). arXiv: [hep-ph/9505225](#).
- [56] K. G. Chetyrkin, Bernd A. Kniehl, and M. Steinhauser. “Decoupling relations to $O(\alpha_s^{**3})$ and their connection to low-energy theorems.” In: *Nucl. Phys. B* 510 (1998), pp. 61–87. DOI: [10.1016/S0550-3213\(97\)00649-4](#). arXiv: [hep-ph/9708255](#).
- [57] Thomas Appelquist and J. Carazzone. “Infrared Singularities and Massive Fields.” In: *Phys. Rev. D* 11 (1975), p. 2856. DOI: [10.1103/PhysRevD.11.2856](#).
- [58] K. G. Chetyrkin, Bernd A. Kniehl, and M. Steinhauser. “Strong coupling constant with flavor thresholds at four loops in the \overline{MS} scheme.” In: *Phys. Rev. Lett.* 79 (1997), pp. 2184–2187. DOI: [10.1103/PhysRevLett.79.2184](#). arXiv: [hep-ph/9706430](#).
- [59] Y. Schroder and M. Steinhauser. “Four-loop decoupling relations for the strong coupling.” In: *JHEP* 01 (2006), p. 051. DOI: [10.1088/1126-6708/2006/01/051](#). arXiv: [hep-ph/0512058](#).
- [60] K. G. Chetyrkin, Johann H. Kuhn, and Christian Sturm. “QCD decoupling at four loops.” In: *Nucl. Phys. B* 744 (2006), pp. 121–135. DOI: [10.1016/j.nuclphysb.2006.03.020](#). arXiv: [hep-ph/0512060](#).
- [61] Robert V. Harlander and William B. Kilgore. “Next-to-next-to-leading order Higgs production at hadron colliders.” In: *Phys. Rev. Lett.* 88 (2002), p. 201801. DOI: [10.1103/PhysRevLett.88.201801](#). arXiv: [hep-ph/0201206](#).
- [62] Charalampos Anastasiou et al. “High precision determination of the gluon fusion Higgs boson cross-section at the LHC.” In: *JHEP* 05 (2016), p. 058. DOI: [10.1007/JHEP05\(2016\)058](#). arXiv: [1602.00695 \[hep-ph\]](#).

- [63] S. Catani and M. H. Seymour. “A General algorithm for calculating jet cross-sections in NLO QCD.” In: *Nucl. Phys. B* 485 (1997). [Erratum: *Nucl.Phys.B* 510, 503–504 (1998)], pp. 291–419. DOI: [10.1016/S0550-3213\(96\)00589-5](#). arXiv: [hep-ph/9605323](#).
- [64] Valentin Ahrens et al. “Origin of the Large Perturbative Corrections to Higgs Production at Hadron Colliders.” In: *Phys. Rev. D* 79 (2009), p. 033013. DOI: [10.1103/PhysRevD.79.033013](#). arXiv: [0808.3008 \[hep-ph\]](#).
- [65] Charalampos Anastasiou et al. “Higgs Boson GluonFusion Production Beyond Threshold in N^3LO QCD.” In: *JHEP* 03 (2015), p. 091. DOI: [10.1007/JHEP03\(2015\)091](#). arXiv: [1411.3584 \[hep-ph\]](#).
- [66] Charalampos Anastasiou et al. “Higgs Boson Gluon-Fusion Production in QCD at Three Loops.” In: *Phys. Rev. Lett.* 114 (2015), p. 212001. DOI: [10.1103/PhysRevLett.114.212001](#). arXiv: [1503.06056 \[hep-ph\]](#).
- [67] Charalampos Anastasiou et al. “Higgs boson gluon–fusion production at threshold in N^3LO QCD.” In: *Phys. Lett. B* 737 (2014), pp. 325–328. DOI: [10.1016/j.physletb.2014.08.067](#). arXiv: [1403.4616 \[hep-ph\]](#).
- [68] Bernhard Mistlberger. “Higgs boson production at hadron colliders at N^3LO in QCD.” In: *JHEP* 05 (2018), p. 028. DOI: [10.1007/JHEP05\(2018\)028](#). arXiv: [1802.00833 \[hep-ph\]](#).
- [69] Robert V. Harlander, Stefan Liebler, and Hendrik Mantler. “SusHi: A program for the calculation of Higgs production in gluon fusion and bottom-quark annihilation in the Standard Model and the MSSM.” In: *Comput. Phys. Commun.* 184 (2013), pp. 1605–1617. DOI: [10.1016/j.cpc.2013.02.006](#). arXiv: [1212.3249 \[hep-ph\]](#).
- [70] Robert V. Harlander, Stefan Liebler, and Hendrik Mantler. “SusHi Bento: Beyond NNLO and the heavy-top limit.” In: *Comput. Phys. Commun.* 212 (2017), pp. 239–257. DOI: [10.1016/j.cpc.2016.10.015](#). arXiv: [1605.03190 \[hep-ph\]](#).
- [71] D. de Florian et al. “Handbook of LHC Higgs Cross Sections: 4. Deciphering the Nature of the Higgs Sector.” In: 2/2017 (Oct. 2016). DOI: [10.23731/CYRM-2017-002](#). arXiv: [1610.07922 \[hep-ph\]](#).
- [72] G. Das, S. Moch, and A. Vogt. “Approximate four-loop QCD corrections to the Higgs-boson production cross section.” In: *Phys. Lett. B* 807 (2020), p. 135546. DOI: [10.1016/j.physletb.2020.135546](#). arXiv: [2004.00563 \[hep-ph\]](#).
- [73] Stefano Catani et al. “Soft gluon resummation for Higgs boson production at hadron colliders.” In: *JHEP* 07 (2003), p. 028. DOI: [10.1088/1126-6708/2003/07/028](#). arXiv: [hep-ph/0306211](#).
- [74] George F. Sterman. “Summation of Large Corrections to Short Distance Hadronic Cross-Sections.” In: *Nucl. Phys. B* 281 (1987), pp. 310–364. DOI: [10.1016/0550-3213\(87\)90258-6](#).
- [75] S. Catani and L. Trentadue. “Resummation of the QCD Perturbative Series for Hard Processes.” In: *Nucl. Phys. B* 327 (1989), pp. 323–352. DOI: [10.1016/0550-3213\(89\)90273-3](#).
- [76] S. Catani and L. Trentadue. “Comment on QCD exponentiation at large x.” In: *Nucl. Phys. B* 353 (1991), pp. 183–186. DOI: [10.1016/0550-3213\(91\)90506-S](#).
- [77] Andreas von Manteuffel, Erik Panzer, and Robert M. Schabinger. “Cusp and collinear anomalous dimensions in four-loop QCD from form factors.” In: *Phys. Rev. Lett.* 124.16 (2020), p. 162001. DOI: [10.1103/PhysRevLett.124.162001](#). arXiv: [2002.04617 \[hep-ph\]](#).

- [78] Christian W. Bauer, Dan Pirjol, and Iain W. Stewart. “Soft collinear factorization in effective field theory.” In: *Phys. Rev. D* 65 (2002), p. 054022. DOI: [10.1103/PhysRevD.65.054022](#). arXiv: [hep-ph/0109045](#).
- [79] Christian W. Bauer et al. “Hard scattering factorization from effective field theory.” In: *Phys. Rev. D* 66 (2002), p. 014017. DOI: [10.1103/PhysRevD.66.014017](#). arXiv: [hep-ph/0202088](#).
- [80] J. A. M. Vermaseren, A. Vogt, and S. Moch. “The Third-order QCD corrections to deep-inelastic scattering by photon exchange.” In: *Nucl. Phys. B* 724 (2005), pp. 3–182. DOI: [10.1016/j.nuclphysb.2005.06.020](#). arXiv: [hep-ph/0504242](#).
- [81] S. Moch, J. A. M. Vermaseren, and A. Vogt. “The Longitudinal structure function at the third order.” In: *Phys. Lett. B* 606 (2005), pp. 123–129. DOI: [10.1016/j.physletb.2004.11.063](#). arXiv: [hep-ph/0411112](#).
- [82] S. Moch, M. Rogal, and A. Vogt. “Differences between charged-current coefficient functions.” In: *Nucl. Phys. B* 790 (2008), pp. 317–335. DOI: [10.1016/j.nuclphysb.2007.09.022](#). arXiv: [0708.3731 \[hep-ph\]](#).
- [83] S. Moch, J. A. M. Vermaseren, and A. Vogt. “Third-order QCD corrections to the charged-current structure function $F(3)$.” In: *Nucl. Phys. B* 813 (2009), pp. 220–258. DOI: [10.1016/j.nuclphysb.2009.01.001](#). arXiv: [0812.4168 \[hep-ph\]](#).
- [84] J. Davies et al. “Non-singlet coefficient functions for charged-current deep-inelastic scattering to the third order in QCD.” In: *PoS DIS2016* (2016), p. 059. DOI: [10.22323/1.265.0059](#). arXiv: [1606.08907 \[hep-ph\]](#).
- [85] J. Blümlein et al. “The massless three-loop Wilson coefficients for the deep-inelastic structure functions F_2 , F_L , xF_3 and g_1 .” In: *JHEP* 11 (2022), p. 156. DOI: [10.1007/JHEP11\(2022\)156](#). arXiv: [2208.14325 \[hep-ph\]](#).
- [86] H. Kawamura et al. “On the next-to-next-to-leading order QCD corrections to heavy-quark production in deep-inelastic scattering.” In: *Nucl. Phys. B* 864 (2012), pp. 399–468. DOI: [10.1016/j.nuclphysb.2012.07.001](#). arXiv: [1205.5727 \[hep-ph\]](#).
- [87] Niccolò Laurenti. “Construction of a next-to-next-to-next-to-leading order approximation for heavy flavour production in deep inelastic scattering with quark masses.” In: (Jan. 2024). arXiv: [2401.12139 \[hep-ph\]](#).
- [88] Julien Baglio et al. “Inclusive production cross sections at $N^3\text{LO}$.” In: *JHEP* 12 (2022), p. 066. DOI: [10.1007/JHEP12\(2022\)066](#). arXiv: [2209.06138 \[hep-ph\]](#).
- [89] Claude Duhr, Falko Dulat, and Bernhard Mistlberger. “Charged current Drell-Yan production at $N^3\text{LO}$.” In: *JHEP* 11 (2020), p. 143. DOI: [10.1007/JHEP11\(2020\)143](#). arXiv: [2007.13313 \[hep-ph\]](#).
- [90] Claude Duhr and Bernhard Mistlberger. “Lepton-pair production at hadron colliders at $N^3\text{LO}$ in QCD.” In: *JHEP* 03 (2022), p. 116. DOI: [10.1007/JHEP03\(2022\)116](#). arXiv: [2111.10379 \[hep-ph\]](#).
- [91] Xuan Chen et al. “Dilepton Rapidity Distribution in Drell-Yan Production to Third Order in QCD.” In: *Phys. Rev. Lett.* 128.5 (2022), p. 052001. DOI: [10.1103/PhysRevLett.128.052001](#). arXiv: [2107.09085 \[hep-ph\]](#).
- [92] Xuan Chen et al. “Transverse mass distribution and charge asymmetry in W boson production to third order in QCD.” In: *Phys. Lett. B* 840 (2023), p. 137876. DOI: [10.1016/j.physletb.2023.137876](#). arXiv: [2205.11426 \[hep-ph\]](#).

- [93] S. Moch et al. “Four-Loop Non-Singlet Splitting Functions in the Planar Limit and Beyond.” In: *JHEP* 10 (2017), p. 041. DOI: [10.1007/JHEP10\(2017\)041](#). arXiv: [1707.08315 \[hep-ph\]](#).
- [94] S. Moch et al. “Low moments of the four-loop splitting functions in QCD.” In: *Phys. Lett. B* 825 (2022), p. 136853. DOI: [10.1016/j.physletb.2021.136853](#). arXiv: [2111.15561 \[hep-ph\]](#).
- [95] J. Davies et al. “Large- n_f contributions to the four-loop splitting functions in QCD.” In: *Nucl. Phys. B* 915 (2017), pp. 335–362. DOI: [10.1016/j.nuclphysb.2016.12.012](#). arXiv: [1610.07477 \[hep-ph\]](#).
- [96] G. Falcioni et al. “The double fermionic contribution to the four-loop quark-to-gluon splitting function.” In: *Phys. Lett. B* 848 (2024), p. 138351. DOI: [10.1016/j.physletb.2023.138351](#). arXiv: [2310.01245 \[hep-ph\]](#).
- [97] Thomas Gehrmann et al. “Complete N_f^2 contributions to four-loop pure-singlet splitting functions.” In: *JHEP* 01 (2024), p. 029. DOI: [10.1007/JHEP01\(2024\)029](#). arXiv: [2308.07958 \[hep-ph\]](#).
- [98] G. Falcioni et al. “Four-loop splitting functions in QCD – The quark-quark case.” In: *Phys. Lett. B* 842 (2023), p. 137944. DOI: [10.1016/j.physletb.2023.137944](#). arXiv: [2302.07593 \[hep-ph\]](#).
- [99] Thomas Gehrmann et al. “The $N_f C_F^3$ contribution to the non-singlet splitting function at four-loop order.” In: *Phys. Lett. B* 849 (2024), p. 138427. DOI: [10.1016/j.physletb.2023.138427](#). arXiv: [2310.12240 \[hep-ph\]](#).
- [100] T. Jaroszewicz. “Gluonic Regge Singularities and Anomalous Dimensions in QCD.” In: *Phys. Lett. B* 116 (1982), pp. 291–294. DOI: [10.1016/0370-2693\(82\)90345-8](#).
- [101] Richard D. Ball and Stefano Forte. “Summation of leading logarithms at small x .” In: *Phys. Lett. B* 351 (1995), pp. 313–324. DOI: [10.1016/0370-2693\(95\)00395-2](#). arXiv: [hep-ph/9501231](#).
- [102] Richard D. Ball and Stefano Forte. “The Small x behavior of Altarelli-Parisi splitting functions.” In: *Phys. Lett. B* 465 (1999), pp. 271–281. DOI: [10.1016/S0370-2693\(99\)01013-8](#). arXiv: [hep-ph/9906222](#).
- [103] Marco Bonvini and Simone Marzani. “Four-loop splitting functions at small x .” In: *JHEP* 06 (2018), p. 145. DOI: [10.1007/JHEP06\(2018\)145](#). arXiv: [1805.06460 \[hep-ph\]](#).
- [104] Xin Guan et al. “Splitting amplitudes at N^3 LO in QCD.” In: *JHEP* 01 (2025), p. 090. DOI: [10.1007/JHEP01\(2025\)090](#). arXiv: [2408.03019 \[hep-ph\]](#).
- [105] J. McGowan et al. “Approximate N^3 LO parton distribution functions with theoretical uncertainties: MSHT20a N^3 LO PDFs.” In: *Eur. Phys. J. C* 83.3 (2023). [Erratum: *Eur.Phys.J.C* 83, 302 (2023)], p. 185. DOI: [10.1140/epjc/s10052-023-11236-0](#). arXiv: [2207.04739 \[hep-ph\]](#).
- [106] Richard D. Ball et al. “The path to N^3 LO parton distributions.” In: *Eur. Phys. J. C* 84.7 (2024), p. 659. DOI: [10.1140/epjc/s10052-024-12891-7](#). arXiv: [2402.18635 \[hep-ph\]](#).
- [107] Thomas Cridge et al. “Combination of a N^3 LO PDFs and implications for Higgs production cross-sections at the LHC.” In: (Nov. 2024). arXiv: [2411.05373 \[hep-ph\]](#).
- [108] Falko Dulat, Achilleas Lazopoulos, and Bernhard Mistlberger. “iHixs 2 — Inclusive Higgs cross sections.” In: *Comput. Phys. Commun.* 233 (2018), pp. 243–260. DOI: [10.1016/j.cpc.2018.06.025](#). arXiv: [1802.00827 \[hep-ph\]](#).

- [109] U. Aglietti et al. “Two loop light fermion contribution to Higgs production and decays.” In: *Phys. Lett. B* 595 (2004), pp. 432–441. DOI: [10.1016/j.physletb.2004.06.063](#). arXiv: [hep-ph/0404071](#).
- [110] Giuseppe Degrandi and Fabio Maltoni. “Two-loop electroweak corrections to Higgs production at hadron colliders.” In: *Phys. Lett. B* 600 (2004), pp. 255–260. DOI: [10.1016/j.physletb.2004.09.008](#). arXiv: [hep-ph/0407249](#).
- [111] Stefano Actis et al. “NNLO Computational Techniques: The Cases $H \rightarrow \gamma\gamma$ and $H \rightarrow gg$.” In: *Nucl. Phys. B* 811 (2009), pp. 182–273. DOI: [10.1016/j.nuclphysb.2008.11.024](#). arXiv: [0809.3667 \[hep-ph\]](#).
- [112] Stefano Actis et al. “NLO Electroweak Corrections to Higgs Boson Production at Hadron Colliders.” In: *Phys. Lett. B* 670 (2008), pp. 12–17. DOI: [10.1016/j.physletb.2008.10.018](#). arXiv: [0809.1301 \[hep-ph\]](#).
- [113] Charalampos Anastasiou, Radja Boughezal, and Frank Petriello. “Mixed QCD-electroweak corrections to Higgs boson production in gluon fusion.” In: *JHEP* 04 (2009), p. 003. DOI: [10.1088/1126-6708/2009/04/003](#). arXiv: [0811.3458 \[hep-ph\]](#).
- [114] Charalampos Anastasiou et al. “Mixed QCD-electroweak corrections to Higgs production via gluon fusion in the small mass approximation.” In: *JHEP* 03 (2019), p. 162. DOI: [10.1007/JHEP03\(2019\)162](#). arXiv: [1811.11211 \[hep-ph\]](#).
- [115] Marco Bonetti, Kirill Melnikov, and Lorenzo Tancredi. “Higher order corrections to mixed QCD-EW contributions to Higgs boson production in gluon fusion.” In: *Phys. Rev. D* 97.5 (2018). [Erratum: *Phys.Rev.D* 97, 099906 (2018)], p. 056017. DOI: [10.1103/PhysRevD.97.056017](#). arXiv: [1801.10403 \[hep-ph\]](#).
- [116] Matteo Becchetti et al. “Next-to-leading order corrections to light-quark mixed QCD-EW contributions to Higgs boson production.” In: *Phys. Rev. D* 103.5 (2021), p. 054037. DOI: [10.1103/PhysRevD.103.054037](#). arXiv: [2010.09451 \[hep-ph\]](#).
- [117] A. Djouadi, M. Spira, and P. M. Zerwas. “Production of Higgs bosons in proton colliders: QCD corrections.” In: *Phys. Lett. B* 264 (1991), pp. 440–446. DOI: [10.1016/0370-2693\(91\)90375-Z](#).
- [118] D. Graudenz, M. Spira, and P. M. Zerwas. “QCD corrections to Higgs boson production at proton proton colliders.” In: *Phys. Rev. Lett.* 70 (1993), pp. 1372–1375. DOI: [10.1103/PhysRevLett.70.1372](#).
- [119] Robert V. Harlander and Kemal J. Ozeren. “Finite top mass effects for hadronic Higgs production at next-to-next-to-leading order.” In: *JHEP* 11 (2009), p. 088. DOI: [10.1088/1126-6708/2009/11/088](#). arXiv: [0909.3420 \[hep-ph\]](#).
- [120] Robert V. Harlander et al. “Higgs production in gluon fusion at next-to-next-to-leading order QCD for finite top mass.” In: *Eur. Phys. J. C* 66 (2010), pp. 359–372. DOI: [10.1140/epjc/s10052-010-1258-x](#). arXiv: [0912.2104 \[hep-ph\]](#).
- [121] Alexey Pak, Mikhail Rogal, and Matthias Steinhauser. “Finite top quark mass effects in NNLO Higgs boson production at LHC.” In: *JHEP* 02 (2010), p. 025. DOI: [10.1007/JHEP02\(2010\)025](#). arXiv: [0911.4662 \[hep-ph\]](#).
- [122] M. Czakon et al. “Exact Top-Quark Mass Dependence in Hadronic Higgs Production.” In: *Phys. Rev. Lett.* 127.16 (2021). [Erratum: *Phys.Rev.Lett.* 131, 179901 (2023)], p. 162002. DOI: [10.1103/PhysRevLett.127.162002](#). arXiv: [2105.04436 \[hep-ph\]](#).
- [123] Peter Marquard et al. “Quark Mass Relations to Four-Loop Order in Perturbative QCD.” In: *Phys. Rev. Lett.* 114.14 (2015), p. 142002. DOI: [10.1103/PhysRevLett.114.142002](#). arXiv: [1502.01030 \[hep-ph\]](#).

- [124] Peter Marquard et al. “Four-loop relation between the \overline{MS} and on-shell quark mass.” In: *PoS RADCOR2015* (2016), p. 094. DOI: [10.22323/1.235.0094](#). arXiv: [1601.03748 \[hep-ph\]](#).
- [125] X. Chen et al. “Precise QCD predictions for the production of Higgs + jet final states.” In: *Phys. Lett. B* 740 (2015), pp. 147–150. DOI: [10.1016/j.physletb.2014.11.021](#). arXiv: [1408.5325 \[hep-ph\]](#).
- [126] Kathrin Becker et al. “Precise predictions for boosted Higgs production.” In: *SciPost Phys. Core* 7 (2024), p. 001. DOI: [10.21468/SciPostPhysCore.7.1.001](#). arXiv: [2005.07762 \[hep-ph\]](#).
- [127] X. Chen et al. “Fully Differential Higgs Boson Production to Third Order in QCD.” In: *Phys. Rev. Lett.* 127.7 (2021), p. 072002. DOI: [10.1103/PhysRevLett.127.072002](#). arXiv: [2102.07607 \[hep-ph\]](#).
- [128] Xuan Chen et al. “NNLO QCD Corrections for Higgs-plus-jet Production in the Four-lepton Decay Mode.” In: *PoS RADCOR2019* (2019), p. 003. DOI: [10.22323/1.375.0003](#). arXiv: [1912.03560 \[hep-ph\]](#).
- [129] Massimiliano Grazzini and Hayk Sargsyan. “Heavy-quark mass effects in Higgs boson production at the LHC.” In: *JHEP* 09 (2013), p. 129. DOI: [10.1007/JHEP09\(2013\)129](#). arXiv: [1306.4581 \[hep-ph\]](#).
- [130] Malte Buschmann et al. “Mass Effects in the Higgs-Gluon Coupling: Boosted vs Off-Shell Production.” In: *JHEP* 02 (2015), p. 038. DOI: [10.1007/JHEP02\(2015\)038](#). arXiv: [1410.5806 \[hep-ph\]](#).
- [131] S. P. Jones, M. Kerner, and G. Luisoni. “Next-to-Leading-Order QCD Corrections to Higgs Boson Plus Jet Production with Full Top-Quark Mass Dependence.” In: *Phys. Rev. Lett.* 120.16 (2018). [Erratum: *Phys.Rev.Lett.* 128, 059901 (2022)], p. 162001. DOI: [10.1103/PhysRevLett.120.162001](#). arXiv: [1802.00349 \[hep-ph\]](#).
- [132] Fady Bishara et al. “Constraining Light-Quark Yukawa Couplings from Higgs Distributions.” In: *Phys. Rev. Lett.* 118.12 (2017), p. 121801. DOI: [10.1103/PhysRevLett.118.121801](#). arXiv: [1606.09253 \[hep-ph\]](#).
- [133] Gage Bonner and Heather E. Logan. “Constraining the Higgs couplings to up and down quarks using production kinematics at the CERN Large Hadron Collider.” In: (Aug. 2016). arXiv: [1608.04376 \[hep-ph\]](#).
- [134] Albert M Sirunyan et al. “Measurement and interpretation of differential cross sections for Higgs boson production at $\sqrt{s} = 13$ TeV.” In: *Phys. Lett. B* 792 (2019), pp. 369–396. DOI: [10.1016/j.physletb.2019.03.059](#). arXiv: [1812.06504 \[hep-ex\]](#).
- [135] Jonas M. Lindert et al. “Top-bottom interference effects in Higgs plus jet production at the LHC.” In: *Phys. Rev. Lett.* 118.25 (2017), p. 252002. DOI: [10.1103/PhysRevLett.118.252002](#). arXiv: [1703.03886 \[hep-ph\]](#).
- [136] Fabrizio Caola et al. “Bottom-quark effects in Higgs production at intermediate transverse momentum.” In: *JHEP* 09 (2018), p. 035. DOI: [10.1007/JHEP09\(2018\)035](#). arXiv: [1804.07632 \[hep-ph\]](#).
- [137] Roberto Bonciani et al. “Next-to-leading-order QCD corrections to Higgs production in association with a jet.” In: *Phys. Lett. B* 843 (2023), p. 137995. DOI: [10.1016/j.physletb.2023.137995](#). arXiv: [2206.10490 \[hep-ph\]](#).

- [138] Hendrik Mantler and Marius Wieseemann. “Top- and bottom-mass effects in hadronic Higgs production at small transverse momenta through LO+NLL.” In: *Eur. Phys. J. C* 73.6 (2013), p. 2467. DOI: [10.1140/epjc/s10052-013-2467-x](https://doi.org/10.1140/epjc/s10052-013-2467-x). arXiv: [1210.8263](https://arxiv.org/abs/1210.8263) [hep-ph].
- [139] Keith Hamilton, Paolo Nason, and Giulia Zanderighi. “Finite quark-mass effects in the NNLOPS POWHEG+MiNLO Higgs generator.” In: *JHEP* 05 (2015), p. 140. DOI: [10.1007/JHEP05\(2015\)140](https://doi.org/10.1007/JHEP05(2015)140). arXiv: [1501.04637](https://arxiv.org/abs/1501.04637) [hep-ph].
- [140] Emanuele Bagnaschi and Alessandro Vicini. “The Higgs transverse momentum distribution in gluon fusion as a multiscale problem.” In: *JHEP* 01 (2016), p. 056. DOI: [10.1007/JHEP01\(2016\)056](https://doi.org/10.1007/JHEP01(2016)056). arXiv: [1505.00735](https://arxiv.org/abs/1505.00735) [hep-ph].
- [141] Emanuele Bagnaschi et al. “Resummation ambiguities in the Higgs transverse-momentum spectrum in the Standard Model and beyond.” In: *JHEP* 01 (2016), p. 090. DOI: [10.1007/JHEP01\(2016\)090](https://doi.org/10.1007/JHEP01(2016)090). arXiv: [1510.08850](https://arxiv.org/abs/1510.08850) [hep-ph].
- [142] Rikkert Frederix et al. “Heavy-quark mass effects in Higgs plus jets production.” In: *JHEP* 08 (2016), p. 006. DOI: [10.1007/JHEP08\(2016\)006](https://doi.org/10.1007/JHEP08(2016)006). arXiv: [1604.03017](https://arxiv.org/abs/1604.03017) [hep-ph].
- [143] Fabrizio Caola et al. “The Higgs transverse momentum spectrum with finite quark masses beyond leading order.” In: *JHEP* 08 (2016), p. 150. DOI: [10.1007/JHEP08\(2016\)150](https://doi.org/10.1007/JHEP08(2016)150). arXiv: [1606.04100](https://arxiv.org/abs/1606.04100) [hep-ph].
- [144] Marco Niggetiedt and Marius Wieseemann. “Higgs-boson production in the full theory at NNLO+PS.” In: *Phys. Lett. B* 858 (2024), p. 139043. DOI: [10.1016/j.physletb.2024.139043](https://doi.org/10.1016/j.physletb.2024.139043). arXiv: [2407.01354](https://arxiv.org/abs/2407.01354) [hep-ph].
- [145] Falko Dulat, Bernhard Mistlberger, and Andrea Pelloni. “Precision predictions at N³LO for the Higgs boson rapidity distribution at the LHC.” In: *Phys. Rev. D* 99.3 (2019), p. 034004. DOI: [10.1103/PhysRevD.99.034004](https://doi.org/10.1103/PhysRevD.99.034004). arXiv: [1810.09462](https://arxiv.org/abs/1810.09462) [hep-ph].
- [146] Falko Dulat, Bernhard Mistlberger, and Andrea Pelloni. “Differential Higgs production at N³LO beyond threshold.” In: *JHEP* 01 (2018), p. 145. DOI: [10.1007/JHEP01\(2018\)145](https://doi.org/10.1007/JHEP01(2018)145). arXiv: [1710.03016](https://arxiv.org/abs/1710.03016) [hep-ph].
- [147] Stefano Actis et al. “RECOLA: REcursive Computation of One-Loop Amplitudes.” In: *Comput. Phys. Commun.* 214 (2017), pp. 140–173. DOI: [10.1016/j.cpc.2017.01.004](https://doi.org/10.1016/j.cpc.2017.01.004). arXiv: [1605.01090](https://arxiv.org/abs/1605.01090) [hep-ph].
- [148] Lucy Budge et al. “The one-loop amplitudes for Higgs + 4 partons with full mass effects.” In: *JHEP* 05 (2020), p. 079. DOI: [10.1007/JHEP05\(2020\)079](https://doi.org/10.1007/JHEP05(2020)079). arXiv: [2002.04018](https://arxiv.org/abs/2002.04018) [hep-ph].
- [149] John Campbell and Tobias Neumann. “Precision Phenomenology with MCFM.” In: *JHEP* 12 (2019), p. 034. DOI: [10.1007/JHEP12\(2019\)034](https://doi.org/10.1007/JHEP12(2019)034). arXiv: [1909.09117](https://arxiv.org/abs/1909.09117) [hep-ph].
- [150] John M. Campbell and R. Keith Ellis. “An Update on vector boson pair production at hadron colliders.” In: *Phys. Rev. D* 60 (1999), p. 113006. DOI: [10.1103/PhysRevD.60.113006](https://doi.org/10.1103/PhysRevD.60.113006). arXiv: [hep-ph/9905386](https://arxiv.org/abs/hep-ph/9905386).
- [151] John M. Campbell, R. Keith Ellis, and Ciaran Williams. “Vector Boson Pair Production at the LHC.” In: *JHEP* 07 (2011), p. 018. DOI: [10.1007/JHEP07\(2011\)018](https://doi.org/10.1007/JHEP07(2011)018). arXiv: [1105.0020](https://arxiv.org/abs/1105.0020) [hep-ph].
- [152] R. Keith Ellis and Giulia Zanderighi. “Scalar one-loop integrals for QCD.” In: *JHEP* 02 (2008), p. 002. DOI: [10.1088/1126-6708/2008/02/002](https://doi.org/10.1088/1126-6708/2008/02/002). arXiv: [0712.1851](https://arxiv.org/abs/0712.1851) [hep-ph].

- [153] Stefano Carrazza, R. Keith Ellis, and Giulia Zanderighi. “QCDLoop: a comprehensive framework for one-loop scalar integrals.” In: *Comput. Phys. Commun.* 209 (2016), pp. 134–143. DOI: [10.1016/j.cpc.2016.07.033](#). arXiv: [1605.03181 \[hep-ph\]](#).
- [154] Kirill Melnikov, Lorenzo Tancredi, and Christopher Wever. “Two-loop $gg \rightarrow Hg$ amplitude mediated by a nearly massless quark.” In: *JHEP* 11 (2016), p. 104. DOI: [10.1007/JHEP11\(2016\)104](#). arXiv: [1610.03747 \[hep-ph\]](#).
- [155] Kirill Melnikov, Lorenzo Tancredi, and Christopher Wever. “Two-loop amplitudes for $qg \rightarrow Hq$ and $q\bar{q} \rightarrow Hg$ mediated by a nearly massless quark.” In: *Phys. Rev. D* 95.5 (2017), p. 054012. DOI: [10.1103/PhysRevD.95.054012](#). arXiv: [1702.00426 \[hep-ph\]](#).
- [156] Lance J. Dixon. “Calculating scattering amplitudes efficiently.” In: *Theoretical Advanced Study Institute in Elementary Particle Physics (TASI 95): QCD and Beyond*. Jan. 1996, pp. 539–584. arXiv: [hep-ph/9601359](#).
- [157] J. A. M. Vermaseren. “New features of FORM.” In: (Oct. 2000). arXiv: [math-ph/0010025](#).
- [158] Ben Ruijl, Takahiro Ueda, and Jos Vermaseren. “FORM version 4.2.” In: (July 2017). arXiv: [1707.06453 \[hep-ph\]](#).
- [159] S. Laporta. “High-precision calculation of multiloop Feynman integrals by difference equations.” In: *Int. J. Mod. Phys. A* 15 (2000), pp. 5087–5159. DOI: [10.1142/S0217751X00002159](#). arXiv: [hep-ph/0102033](#).
- [160] Philipp Maierhöfer, Johann Usovitsch, and Peter Uwer. “Kira—A Feynman integral reduction program.” In: *Comput. Phys. Commun.* 230 (2018), pp. 99–112. DOI: [10.1016/j.cpc.2018.04.012](#). arXiv: [1705.05610 \[hep-ph\]](#).
- [161] Philipp Maierhöfer and Johann Usovitsch. “Kira 1.2 Release Notes.” In: (Dec. 2018). arXiv: [1812.01491 \[hep-ph\]](#).
- [162] Jonas Klappert et al. “Integral reduction with Kira 2.0 and finite field methods.” In: *Comput. Phys. Commun.* 266 (2021), p. 108024. DOI: [10.1016/j.cpc.2021.108024](#). arXiv: [2008.06494 \[hep-ph\]](#).
- [163] U. Baur and E. W. Nigel Glover. “Higgs Boson Production at Large Transverse Momentum in Hadronic Collisions.” In: *Nucl. Phys. B* 339 (1990), pp. 38–66. DOI: [10.1016/0550-3213\(90\)90532-I](#).
- [164] Michał Czakon et al. “The $(Q_7, Q_{1,2})$ contribution to $\bar{B} \rightarrow X_s \gamma$ at $\mathcal{O}(\alpha_s^2)$.” In: *JHEP* 04 (2015), p. 168. DOI: [10.1007/JHEP04\(2015\)168](#). arXiv: [1503.01791 \[hep-ph\]](#).
- [165] Vladimir A. Smirnov. “Applied asymptotic expansions in momenta and masses.” In: *Springer Tracts Mod. Phys.* 177 (2002), pp. 1–262.
- [166] Marco Niggetiedt. “Quark mass effects in form factors and hadronic Higgs production.” PhD thesis. 2023. DOI: [10.18154/RWTH-2023-11198](#).
- [167] Simone Marzani et al. “Higgs production via gluon-gluon fusion with finite top mass beyond next-to-leading order.” In: *Nucl. Phys. B* 800 (2008), pp. 127–145. DOI: [10.1016/j.nuclphysb.2008.03.016](#). arXiv: [0801.2544 \[hep-ph\]](#).
- [168] Stefan Dittmaier, Michael Krämer, and Michael Spira. “Higgs radiation off bottom quarks at the Tevatron and the CERN LHC.” In: *Phys. Rev. D* 70 (2004), p. 074010. DOI: [10.1103/PhysRevD.70.074010](#). arXiv: [hep-ph/0309204](#).

- [169] Barbara Schmidt and Matthias Steinhauser. “CRunDec: a C++ package for running and decoupling of the strong coupling and quark masses.” In: *Comput. Phys. Commun.* 183 (2012), pp. 1845–1848. DOI: [10.1016/j.cpc.2012.03.023](https://doi.org/10.1016/j.cpc.2012.03.023). arXiv: [1201.6149 \[hep-ph\]](https://arxiv.org/abs/1201.6149).
- [170] K. G. Chetyrkin, Johann H. Kuhn, and M. Steinhauser. “RunDec: A Mathematica package for running and decoupling of the strong coupling and quark masses.” In: *Comput. Phys. Commun.* 133 (2000), pp. 43–65. DOI: [10.1016/S0010-4655\(00\)00155-7](https://doi.org/10.1016/S0010-4655(00)00155-7). arXiv: [hep-ph/0004189](https://arxiv.org/abs/hep-ph/0004189).
- [171] R. L. Workman et al. “Review of Particle Physics.” In: *PTEP* 2022 (2022), p. 083C01. DOI: [10.1093/ptep/ptac097](https://doi.org/10.1093/ptep/ptac097).
- [172] R. Tarrach. “The Pole Mass in Perturbative QCD.” In: *Nucl. Phys. B* 183 (1981), pp. 384–396. DOI: [10.1016/0550-3213\(81\)90140-1](https://doi.org/10.1016/0550-3213(81)90140-1).
- [173] N. Gray et al. “Three Loop Relation of Quark (Modified) \overline{MS} and Pole Masses.” In: *Z. Phys. C* 48 (1990), pp. 673–680. DOI: [10.1007/BF01614703](https://doi.org/10.1007/BF01614703).
- [174] Kirill Melnikov and Alexander Penin. “On the light quark mass effects in Higgs boson production in gluon fusion.” In: *JHEP* 05 (2016), p. 172. DOI: [10.1007/JHEP05\(2016\)172](https://doi.org/10.1007/JHEP05(2016)172). arXiv: [1602.09020 \[hep-ph\]](https://arxiv.org/abs/1602.09020).
- [175] Matthew A. Lim and Rene Poncelet. “Robust estimates of theoretical uncertainties at fixed-order in perturbation theory.” In: (Dec. 2024). arXiv: [2412.14910 \[hep-ph\]](https://arxiv.org/abs/2412.14910).
- [176] Cappati et al. “ggF Status Report.” In: The 21st Workshop of the LHC Higgs Working Group. URL: <https://indico.cern.ch/event/1389221/contributions/6185912/attachments/2979973/5249263/241204-ggFWG1Update-3.pdf>. 2024.
- [177] R. L. Workman et al. “Review of Particle Physics.” In: *PTEP* 2022 (2022), p. 083C01. DOI: [10.1093/ptep/ptac097](https://doi.org/10.1093/ptep/ptac097).